Modeling Bone Marrow Sub-Structures at Power-Line Frequencies

by

Roanna Sum-Wan Chiu
B.A.Sc., Simon Fraser University, 1999

A Thesis Submitted in Partial Fulfillment of the
Requirements for the Degree of

MASTER OF APPLIED SCIENCE

in the Department of Electrical and Computer Engineering

Supervisor: Dr. Maria A. Stuchly

ABSTRACT

Bone marrow resides in cancellous bone and is known to be responsible for leukemia. The irregular geometry and differences in dielectric properties of different components within the bone marrow network cause electromagnetic fields to distribute non-uniformly within bone marrow sub-structures. Applying numerical computation techniques – finite element method and scalar potential finite difference method – the field distributions were studied. CT scan data of cancellous bone, as well as a simplified bone marrow stroma cell with gap junctions were used. Electric field enhancement of up to 50% was observed in the former, while transmembrane potential change was estimated to vary from several to over 200 μV across the gap junction connecting adjoining stroma cells.

Table of Content

List of Figures

List of Tables

ACKNOWLEDGEMENTS

I would like to thank my supervisor, Dr. Maria Stuchly, for her guidance, encouragement as well as patience with me. I would also like to thank members of the Applied Electromagnetics Group for their suggestions and company. Special thanks should be given to Dr. Kris Caputa and Donna Shannon for their technical and administrative support and advices. Finally, I would like to express my gratitude to Dr. Stuchly and Hui-Siong Ng for helping with the editing of this thesis when I did not even want to read my own writing.

1. Introduction: Electromagnetic Fields & Health Effects

Electrical power has been a part of modern living for many years. Few would question the need to make it available to every household. However, whether it is truly harmless to human health is still debated within the scientific community, as well as among the general public.

1.1 Background: Epidemiology Reports

While residential power safety precautions usually refer to proper handling of high voltage current or preventing electroshocks, guidelines regarding electromagnetic fields (EMF) associated with electricity supply have also been developed and reviewed. The concern of possible harmful health effects from power-frequency EMF gained public attention in the late 70's. Wertheimer and Leeper published a report in 1979 [1] linking electric wiring configurations with childhood cancer – leukemia in specific. They suggested a positive correlation in increased childhood cancer risk to the magnetic fields induced by imbalanced current between the distribution wires and the ground line through water pipes. The original investigation was conducted in the greater Denver area, and since then, many similar studies have been performed in different regions worldwide.

The results of these studies were inconsistent, but one similarity among them was that they were mostly epidemiology analysis. These epidemiology studies focused on analyzing human health records, especially occurrences of cancers, and then attempted to identify correlation, if any, to the environmental settings. Some other studies also investigated claims of exposure-related symptoms, such as headaches, loss of sleep, increased irritability, etc. While these studies provided the most direct information about human health, they suffered from several limitations. Quantifying and isolating the various factors involved are often difficult: for example, aside from environmental factors, human health is directly related to diet and lifestyle. After all, there are only a few agents such as tobacco smoke that are clearly carcinogenic. Another difficulty is identifying a good sample population which is sufficiently random and unbiased. Conducting a study in a small rural village with two hundred residents probably cannot produce

representative data for household electrical use in the particular country. Childhood leukemia is an often deadly but rare disease, which makes it harder to gather a significant sample size.

1.2 Experimental Approaches

Aside from epidemiology, researchers attempted to address the question through biological experiments. Animal experiments have studied influences on behaviour, neurophysiology, reproduction, bone development, immunology, etc. Whole animal studies often involved exposing mammals to high levels of EMF for prolonged periods of time. Some studies have also applied carcinogenic substances to groups of animals, or employed tumor-bearing animals to determine if exposure to EMF would accelerate tumor development. While these experiments were often well-controlled, the obvious question is the reliability of these data when extrapolating to human exposure conditions. Due to different anatomy, fields in tissue are distributed differently in different species. Numerous papers have been published since the original report; neither human nor animal studies have shown any conclusive detrimental effects [2].

Cellular studies allow for investigations at microscopic level of the mechanisms involved when biological tissues are exposed to EMF, thus enabling researchers to evaluate processes involved and fundamental interactions. Some cellular studies were performed with actual cells *in vitro*, where metabolism or genetic effects were observed. Sometimes measurements were taken of enzyme or membrane activities. Other researchers have also developed cell replicas in different configurations to estimate properties such as membrane potential, inter-cellular forces, etc. [3].

1.3 Numerical Computations

An alternative approach to cellular studies is through numerical computation. Using simplified models of the organs or cells of interest, the field distributions can be obtained using known mathematical formulas. For homogeneous spherical or ellipsoidal cell models, potential distribution can be obtained by solving Laplace's equation. Electric

fields in cell components for ellipsoidal models with various axial ratios have also been calculated analytically and tabulated by Bernhardt and Pauly [4]. However, few of actual human cells are exactly uniform in shape. While a typical biological cell is usually depicted as roughly spherical with irregular boundary, exceptions are numerous including the familiar examples of muscle and neurons.

Availability of more powerful computational resources brought about higher accuracy and efficiency; even more importantly, it opened the possibility of computing more complex, and hence realistic models using numerical methods. Not only single cells, but cell assemblies of different configurations and finer features can be computed [5]. Alternatively, whole body computations of human models are also possible, where anatomically realistic data are employed [6]. Numerical computation can certainly provide new insights in resolving the mysterious link between power-frequency EMF and leukemia.

1.4 Leukemia

Leukemia, according to the definition of National Cancer Institute [7], is a "cancer that starts in blood-forming tissue such as the bone marrow, and causes large numbers of blood cells to be produced and enter the blood stream." Therefore to address the problem through computational approaches, field distributions over the whole human body were computed and the tissue dose for bone marrow analyzed.

Epidemiology reports link cancer risk to wiring configurations, which is directly related to magnetic field. Therefore, many computations were performed concerning power-frequency magnetic field and human body. In 2000, Kavet *et al.* [8] proposed contact current as the medium between residential magnetic field and induced fields in the body. Based on that assumption, Dawson *et al.* [9] employed anatomically realistic human models developed from magnetic resonance imaging data, and found that relatively strong electric fields could arise from contact currents of moderate strength.

Whereas bone marrow is not one specific type of tissue, but a network of fatty connective tissue found in large bones, a sub-cellular approach may provide a different perspective in understanding the actual mechanism that takes place. Macroscopic dosimetry studies lay the foundation for such sub-cellular modeling.

1.5 Objectives and Outline of This Thesis

In summary, with the motivation provided by the hypothesis linking childhood leukemia to strong electric fields in bone marrow, and by the currently available resources for numerical analysis, the objectives of this thesis are:

- To compute the electric fields in a model of bone marrow consisting of two domains, namely the cancellous bone and medium representing average electrical properties of bone marrow,
- To compute the electric fields in a model of the stroma cell (which is the most complex cell of the marrow), and
- To evaluate the significance of electric field enhancements due to the geometry and electrical properties of the bone marrow components.

This thesis extends the results obtained from previous computations of heterogeneous human model exposed to electric and magnetic fields. Section 2 is a brief summary of research history in the study of extremely low-frequency (ELF) EMF. In section 3, the two numerical methods employed in this research will be discussed and the selected models of bone marrow sub-structures explained in details. Results obtained are presented and discussed in section 4. The discussions section contains verifications of the results, followed by the implications of the obtained results to the hypothesis of strong local electric field in bone marrow. Section 6 concludes the thesis with a summary of the work accomplished, as well as proposal for future research directions.

2. Brief Review of Previous Research

Over the last decade, many engineering reviews have been published in response to epidemiology reports on adverse health effects possibly caused by power-frequency EMF [10]-[14]. Some argued that the assumptions or hypotheses in the epidemiology studies were flawed [12]; others suggested that the evidence in support of links between EMF and cancer was weak and inconsistent, although it could not be proven that such link did not exist [13]; yet some pointed out the economic impacts due to this fear had to be properly addressed [14]. The general conclusion has been that despite all the data reported, the issue remained a scientific uncertainty. Most authors called for more research, especially to examine the underlying biological mechanisms that are still inadequately understood.

Extensive research programs covering present knowledge in epidemiology, animal studies, cellular experiments, field computations, risk assessments, etc., have been conducted in different countries. The Electric and Magnetic Fields Research and Public Information Dissemination (EMF RAPID) Program in the United States concluded in 1999 that "the scientific evidence suggesting that ELF-EMF exposures pose any health risk is weak." [15] In Japan, researchers engaged in a similar project reported that "there is no evidence to indicate that the EMFs found in the environment in Japan are harmful to health." [16]

Epidemiology studies are usually not reproducible and are often associated with numerous uncertainties. Inconsistent results of human and animal experiments have been reported from different laboratories. Cellular studies tend to be very specific, i.e., the results are cell-specific or process-dependent. Engineering evaluation of electric fields in tissues with numerical methods is relatively inexpensive. It provides a way to quantify the interactions of EMF and biological cells with consistency and accuracy. The rest of this thesis will be focused on addressing the issue of power-frequency EMF on biological subjects through numerical approaches.

2.1 Whole Body Human Models

In the past, human models were represented as geometric combinations of spheres, cylinders and ellipsoids, where field distribution can be solved analytically (Figure 2.1a). Later, with the development of integral equation methods (e.g., Method of Moments) [17], some investigators solved the field problem using models made up of cubic cells [18] (Figure 2.1b). These models were more realistic since the gross anatomic and biometric characteristics of human bodies were accounted for.

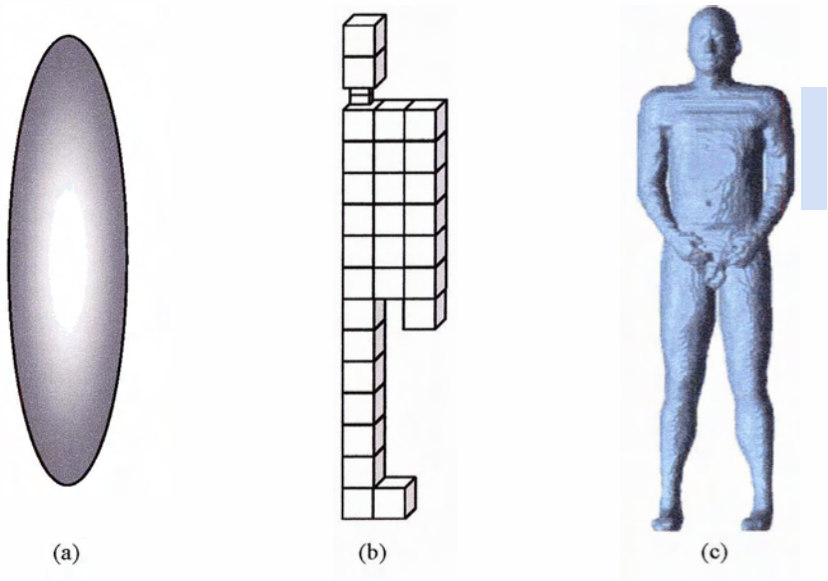

Figure 2.1: Human models (a) as ellipsoid which can be solved analytically; (b) made up of cubic cells; (c) created from MRI data thus are more realistic anatomically

Recently, with the advancements in medical imaging technologies (e.g., MRI and CT), different research groups developed anatomically realistic models of the human body as shown in Figure 2.1c [6][19][20]. Progresses in development of numerical techniques, combined with increasingly powerful computer resources, more complex problems can be computed. These heterogeneous models defined up to over 30 organs or tissues, thus enabling tissue-specific dosimetry calculations. It is known that different tissues have different dielectric properties, which can markedly influence their responses to EMF.

Even though our modern day living surrounds us with power grids, most of the time we are not exposed directly to strong fields. However, it has been recognized that induced fields inside tissues could produce effects similar to strong external fields. In fact, cells react strongly to field strengths in their immediate vicinity. Thus, it is important to be able to identify the distribution of fields in different tissues, or regions of the body.

Numerical methods commonly employed for ELF computations for whole body human models include scalar potential finite difference (SPFD) [6][19], impedance method [19][20], and variations of the finite difference time domain (FDTD) method [6][20]. As for the tissue dielectric values, a comprehensive listing by Gabriel *et al.* published in 1996 is widely used [21]. Research groups working with these anatomically accurate human models often based the dielectric values on Gabriel's paper, or on other previously published articles. Some also used a combination of both and compared the results.

Results from three independent research groups obtained using different human models and different numerical methods were compared [22]. These results were in reasonable agreement whereas differences could be explained rationally. It was highlighted that apart from numerical error, voxels sizes, and variations in anatomies of the models, the assignment of conductivity values played an important role in the accuracy of the results.

2.2 Cellular Models

Although macroscopic dosimetry data provide information about local fields within an organ or a smaller region of the body, computations of smaller sub-structures allow more in depth investigation of the biological mechanisms that take place.

One of the dominant features of a typical biological cell is its highly-resistive membrane. Figure 2.2 shows a much simplified representation of a biological cell consisting of membrane and cytoplasm. Typical dielectric values and dimensions are also listed for reference. The cell is usually assumed to be suspending in conductive medium representing typical body fluid. The membrane separates the interior of the cell (cytoplasm) from the surrounding. Consisting of lipids, proteins and some carbohydrates,

it serves its regulatory function of controlling the inflow and outflow of substance into or from the cell through active ion transport. Due to its essentially nonconductive nature at low-frequencies, the membrane itself experiences the full range of potential changes in the surrounding, while shielding the interior of the cell, which maintains a field close to zero.

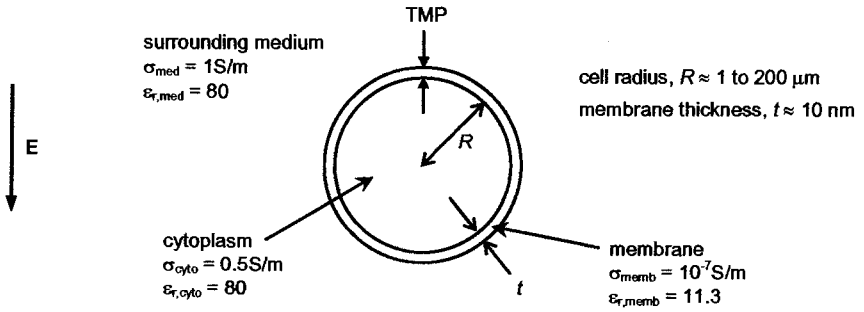

Figure 2.2: Simplified model of a biological cell with typical dielectric and dimensional values

Living organisms distort the electric fields in their vicinity in such a manner that the fields are nearly perpendicular to the boundary surfaces [23]. With its curved surface, when a biological cell is placed in a uniform field, the resultant electric field is concentrated at the two extremities of the membrane. The drop in potential across the membrane, known as transmembrane potential (TMP), has been the focus of several investigations.

Even though no two cells are exactly identical, a lot of them can roughly be represented by spherical or ellipsoidal shapes. Analytical TMP approximations were found for these primitive shapes [4][24]. Induced TMP is proportional to cell dimension; therefore, connected cells would have larger TMP. Similarly, TMP is also influenced by the presence of neighbouring cells. Fear and Stuchly [25] and Susil *et al.* [26] computed numerically the TMP obtained from different cell assemblies including chains, sheets, clusters, etc., where cell radii, density and field orientation were varied.

For better conformity to the curved surfaces of these cellular models, finite element method (FEM) is often the numerical technique of choice. Instead of regular grids as in FDTD or impedance method (IM), the FEM mesh is made up of arbitrarily shaped elements, typically tetrahedrons of different sizes for 3D models.

2.2.1 Gap-Connected Cells

Another cell feature worth studying is the gap junction, which is an aqueous channel in the membrane through which neighbouring cells are connected. It is believed that many types of cells are connected through gap junctions. These junctions are sites for ionic exchanges, which are crucial to maintaining the equilibrium within the cell, as well as passing bio-signals. Scientists have proposed that disturbance to these gap communications could cause detrimental effect to the growth of cells, and cancer was considered as disease of cell development [27]. Other experiments have also shown that even weak EMF may affect intercellular communication [28], since gap-connected cell chains have enhanced TMP compared to single cells.

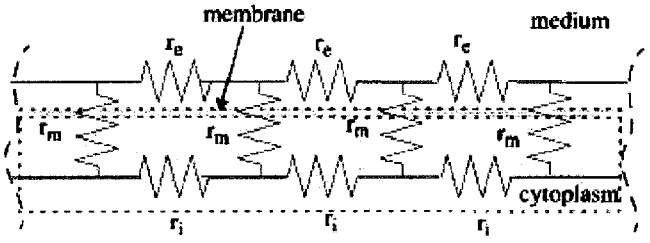

Figure 2.3: Leaky Cable Model [5]

TMP of gap-connected cells can be approximated by the leaky cable model [28] as shown in Figure 2.3. Field distributions in assemblies of cells connected by gap junctions have been computed with various cell radii, and different cell configurations [5]. The cells employed in these computations were assumed to be ellipsoidal or elongated, consisting only of membrane and cytoplasm. These cells were usually assumed to be suspending in homogenous conductive medium. Figure 2.4 is a 2D illustration of a chain of three elongated cells connected by gap junctions.

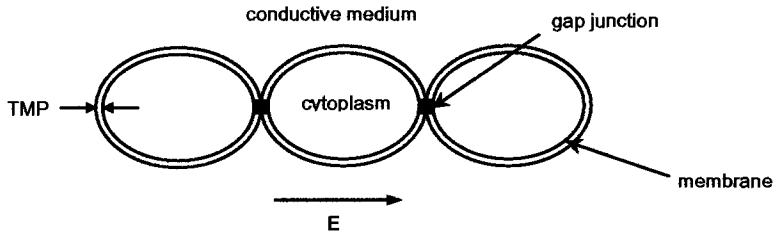

Figure 2.4: A Chain of Three Elongated Cells Connected by Gap Junctions

Although these models were much simplified, they demonstrated how cell dimensions, configurations, and even gap junction sizes could all contribute to the change in TMP, and hence distribution of electric field in the vicinity of the cells or cell assemblies.

In this thesis, bone marrow stroma cells are considered. They are connected with gap junctions and are highly irregular in shape. Although computer resources limit us from creating more complex geometry and we are only using a single cell, we believe that this is a significant step to modeling of more realistic biological cells.

3. Methods & Models

3.1 Numerical Methods

Numerical analysis can date back to before the invention of computers. While many different algorithms and methods have been proposed, the basic idea is common: if a problem can be represented by mathematical formulations, regardless of its complexity, it can be divided into subsets where simpler expressions can be readily solved. With better understanding of underlying phenomena, many physical expressions can be simplified accordingly. For example, even though the planet earth has a finite size and mass, most of the time it is sufficient to consider it as an infinite ground plane in electromagnetic propagation problems. However, when problems are discretized, some errors would inevitably be introduced. Most numerical methods available nowadays have been improved over the years; together with more powerful processors and memory resources, accuracy is usually not a problem. Researchers often compare the numerical results with known analytical solutions, and excellent agreements have been reported.

In the assessment of potential detrimental health effects of EMFs on human, the models are often so complex that analytical expressions do not exist. In order to validate our results, two different numerical methods – FEM and SPFD – are employed for each of the models.

3.1.1 Fundamental Formulations

Electromagnetic problems are governed by the well-known Maxwell's equations:

$$\begin{aligned} \nabla \times \mathbf{E} &= -\frac{\partial \mathbf{B}}{\partial t} - \mathbf{M} & \nabla \cdot \mathbf{D} &= \rho \\ \nabla \times \mathbf{H} &= \frac{\partial \mathbf{D}}{\partial t} + \mathbf{J} & \nabla \cdot \mathbf{B} &= 0 \end{aligned} \tag{3.1}$$

and the constitutive relations in generalized form are given as:

$$\begin{aligned} \mathbf{D} &= \varepsilon_0 \varepsilon_r \mathbf{E} + \mathbf{P} \\ \mathbf{B} &= \mu_0 \mu_r (\mathbf{H} + \mathbf{M}) \\ \mathbf{J} &= \sigma \mathbf{E} + \mathbf{J}^e \end{aligned} \tag{3.2}$$

where $\mathbf{P}$ is the electric polarization vector, $\mathbf{M}$ is the magnetization vector and $\mathbf{J}^e$ denotes externally generated current.

Another fundamental equation, known as the equation of continuity defines:

$$\nabla \cdot \mathbf{J} = -\frac{\partial \rho}{\partial t} \tag{3.3}$$

while the electric scalar potential (ϕ) is given by

$$\mathbf{E} = -\nabla \phi \tag{3.4}$$

With heterogeneous models, it is important to know the fields at material interfaces, as specified by the boundary conditions:

$$\begin{aligned} \hat{\mathbf{n}} \times (\mathbf{E}_1 - \mathbf{E}_2) &= \mathbf{0} \\ \hat{\mathbf{n}} \cdot (\mathbf{D}_1 - \mathbf{D}_2) &= \rho_S \\ \hat{\mathbf{n}} \times (\mathbf{H}_1 - \mathbf{H}_2) &= \mathbf{J}_S \\ \hat{\mathbf{n}} \cdot (\mathbf{B}_1 - \mathbf{B}_2) &= 0 \end{aligned} \tag{3.5}$$

which also determines the interface condition for current density:

$$\hat{\mathbf{n}} \cdot (\mathbf{J}_1 - \mathbf{J}_2) = -\frac{\partial \rho_S}{\partial t} \tag{3.6}$$

3.1.2 Electrostatic Approximation

At ELF range, the electric field and magnetic field can be decoupled. Considering the sizes of the objects of interest, the requirement for quasi-static approximation is satisfied as the cell sizes are smaller than the wavelength at 60 Hz ($\lambda = c/f = 5\times10^6$ m). At this frequency, $\omega = 2\pi f = 120\pi \approx 377$ radians, the displacement current governed by the $j\omega\varepsilon$ factor becomes very small ($\varepsilon_0 \approx 8.854\times10^{-12}$ F/m) compared to the conduction current density ($\mathbf{J} = \sigma\mathbf{E}$) term; the permittivity (ε) terms can be disregarded in the calculation and only conductivity (σ) terms need to be considered.

Since the quasi-static approximation implies that the variations in time are small, the continuity Equation (3.3) can be rewritten as:

$$\nabla \cdot \mathbf{J} = 0 \qquad (3.7)$$

and Ampère's law in Equation (3.1) becomes:

$$\nabla \times \mathbf{H} = \mathbf{J} = \sigma\mathbf{E} \qquad (3.8)$$

Magnetic fields pass through the human body mostly unchanged, while electric fields are significantly perturbed. Boundary conditions define that external electric fields are nearly perpendicular to the surface of the organism. Although human exposures to power-frequency EMFs are usually due to currents and charges on conductors, it can be assumed in most cases that the sources are far enough to assume a uniform distribution to the sub-structure of interest. These simplifications greatly reduce the amount of computation.

Our computation focuses on the enhancement of electric field, which is believed to cause biological effects (which may not necessarily be adverse) even at low-dose and low-frequencies. Since we are not estimating the actual electric field strength at the given structures, but only the ratio of the resultant fields compared to the source fields, we can assume an external field of 1 V/m for ease of comparison, although this may not be a realistic value to be present in human body.

Taking advantages of these assumptions, our models are set up as parallel plate capacitors, where the potential difference between the top and bottom plates supplies the source field. Figure 3.1 shows the generic setup for the models. Note that ample space is necessary between the subject under test and the boundaries of the computational domain. This ensures that the incident fields on the subjects are distributed uniformly, while also minimizing artifacts due to the proximity of the boundaries.

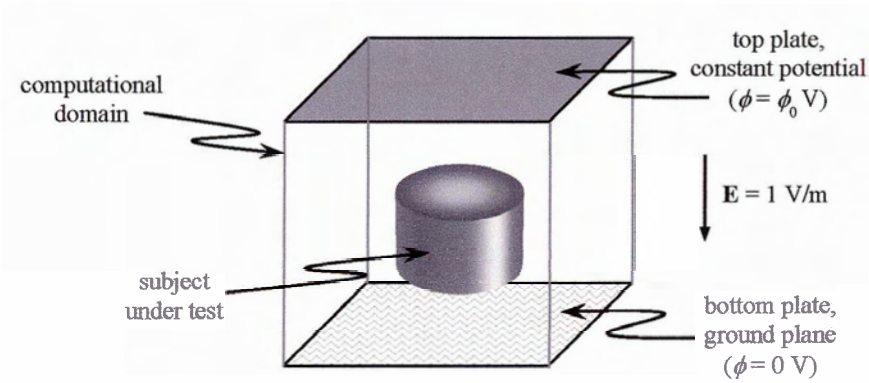

Figure 3.1: Generic Model Setup

3.1.3 Finite Element Method

FEM was originally developed for solving structural problems, but it has been employed in many different fields. Although it may not be the most widely used method in electromagnetics, it is definitely gaining popularity, especially with the availability of more powerful and flexible FEM packages.

The method gets its name from the *finite elements* composing the computational domain. These elements do not have to be identical or rectangular. Hence FEM is known for its ability to conform to irregular geometries, and therefore is our method of choice solving electromagnetic problems involving biological tissues, which hardly fit into regular grids.

Apart from commercial packages, there is an abundance of FEM resources available in the public domain. Awadhiya *et al.* published quite an extensive list lately [29]. Despite this, our research employes FEMLAB, a commercial package developed by the Swedish

company COMSOL AB. FEMLAB was selected among other FEM packages due to the many features and functionality it promised, and its ability to integrate seamlessly with MATLAB [30].

FEMLAB is intended to be a multiphysics application and, therefore, is capable of handling numerical problems in different domains from acoustics to electromagnetics to geophysics. The underlying engine is a partial differential equation (PDE) solver. The standard coefficient form stationary problems can be generalized as [31]:

$$\begin{cases} \nabla \cdot (-c\nabla u - \mathbf{A}u + \mathbf{C}) + \mathbf{B} \cdot \nabla u + au = f \\ \hat{\mathbf{n}} \cdot (c\nabla u + \mathbf{A}u - \mathbf{C}) + qu = g - h^T \mu \\ hu = r \end{cases} \tag{3.9}$$

where u is the single dependent variable; $\mathbf{A}$, $\mathbf{B}$, $\mathbf{C}$ are vectors of n dimensions, while $\hat{\mathbf{n}}$ is the outward unit normal on the boundary of the subdomain. Each finite element can be viewed as a mini-subdomain where these coefficients are constant. The first equation in (3.9) is defined in the union of the subdomains, while the other two are defined on the boundaries. The second equation is a generalized Neumann boundary condition, while the third equation can be referred to as the Dirichlet boundary condition.

At first glance our models seem to belong to electrostatic field or quasi-static field problems, but since our models consist only of isotropic materials with no external current or polarization, the "Conductive Media DC" mode would suffice.

The equation defining this mode is [31]:

$$-\nabla \cdot (\sigma \nabla \phi) = Q \tag{3.10}$$

where Q is the current source.

Equation (3.10) is essentially a classical Poisson's equation by combining Gauss' law with the equation of continuity (3.3). Writing current density in terms of electric potential:

$$\mathbf{J} = -\sigma \nabla \phi \tag{3.11}$$

the boundary conditions become:

Table 3.1: Boundary Conditions for Conductive Media DC Mode [31]

Boundary Condition	Description
$-\mathbf{n}\cdot\mathbf{J}+q\phi=g$	Inward current
$-\mathbf{n}\cdot\mathbf{J}=0$	Symmetry
$\phi=\phi_0$	Electric potential
$\phi=0$	Ground or antisymmetry

Note that the second condition is a special case for the first (when q and g are both zero) and likewise, the third condition is a special case for the fourth (when $\phi_0 = 0$). The first two conditions correspond to the Neumann condition in (3.9) while the last two correspond to the Dirichlet condition.

Comparing equation (3.10) and Table 3.1 to (3.9), the dependent variable (u) to be solved is the scalar electric potential ϕ, and the other coefficients in the system of PDE can be replaced as follows:

Table 3.2: Coefficients of the PDE

Coefficient from (3.9)	Expression	Description
c	σ	Conductivity
f	Q	Current source
g	G	Inward current density
q	Q	Film conductance
h	1	Generalization (scaling) factor
r	ϕ_0	Electric potential

The other coefficients present in (3.9) are not used in this mode and, therefore, are considered zeros.

For our particular setup, Q, g, q are zeros as the only external source is the uniform electric field produced by the constant potential on the top and bottom plate. Therefore, the top plate is assigned the third boundary condition as listed in Table 3.1 and the

bottom plate the fourth. The side faces of the computational domain are all defined to have symmetric boundary conditions.

The system of PDEs for all the finite elements can be solved iteratively. For stationary problems, FEMLAB offers three iterative algorithms: (1) Good Broyden Method, (2) Generalized Minimal Residual method (GMRES) and (3) Transpose-Free Quasi-Minimal Residual method (TFQMR). Our implementations use the Good Broyden method, which is the default option.

Prior to solving the PDEs, the computational domain must be first subdivided into finite elements. This process is known as mesh generation. FEMLAB comes with a built-in mesh generator which allows the user to control the mesh fineness by specifying element parameters such as maximum element size as a ratio of the longest length of the geometry.

Although FEMLAB provides a comprehensive interactive graphical user interface (GUI), all the features are also available as MATLAB functions. Some of our models have their geometries created using the GUI, but all of them are executed as MATLAB scripts in batch mode. The program (FEMLAB version 2.3) is installed on a Linux workstation (kernel version 2.4) with an AMD Athlon 1.6 GHz processor and 1.5 GB or RAM.

3.1.4 Scalar Potential Finite Difference Method

To compare the FEM results with a regular grid computational technique, the SPFD method is chosen due to the availability of an in-house SPFD program. The code was developed and employed previously by members of the research group in whole human model computation [32]-[34].

SPFD is a numerical approach originally designed for quasi-static magnetic field induction problems. Similar to FDTD grids, the computational domain is discretized into a uniform set of voxels. As illustrated in Figure 3.2a, potentials (ϕ) are defined at the vertices while electric field components (E_x, E_y, E_z) are defined on a staggered array along the voxel edges. The electric field values are taken from the edge centres, while magnetic field components (H_x, H_y, H_z) align with the face-normals.

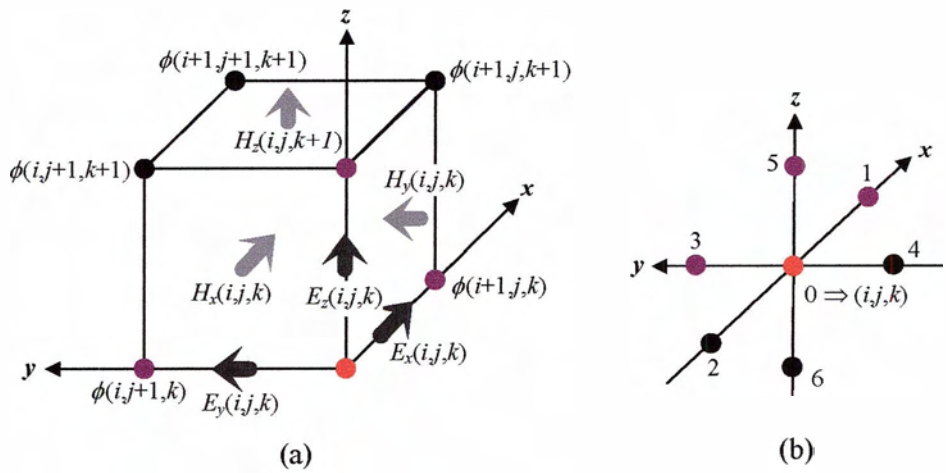

Figure 3.2: SPFD Elements [32]: (a) is a representative voxel with corresponding potentials, electric and magnetic field vectors indicated accordingly; (b) illustrates the local indexing scheme at a node

The SPFD method requires the subjects to be conducting bodies, to which the electromagnetic fields can be expanded in a power series. Under quasi-static assumptions, the internal electric field can be regarded as solely induced by the applied magnetic field; and the internal magnetic field is strictly dependent on the internal electric field. Therefore, the problem reduces to solving the differential equations for the electric field within the body:

$$\begin{aligned} \nabla \times \mathbf{E} &= -j\omega\mathbf{B} \\ \nabla \cdot (\sigma\mathbf{E}) &= 0 \end{aligned} \qquad (3.12)$$

The applied magnetic field term can be substituted by a magnetic vector potential, **A**:

$$\mathbf{B} = \nabla \times \mathbf{A} \qquad (3.13)$$

and, therefore, from the first equation of (3.12):

$$\begin{aligned} \nabla \times \mathbf{E} &= -j\omega(\nabla \times \mathbf{A}) = -\nabla \times (j\omega\mathbf{A}) \\ \nabla \times (\mathbf{E} + j\omega\mathbf{A}) &= 0 \end{aligned} \qquad (3.14)$$

Vector identities define that $\nabla \times (\nabla \psi) = 0$; therefore, the term in equation (3.14) can be replaced by the negative gradient of a scalar potential ϕ:

$$\begin{aligned} &\nabla \times (\mathbf{E} + j\omega\mathbf{A}) \Rightarrow \nabla \times (-\nabla\phi) = 0 \\ &\therefore \nabla\phi = -(\mathbf{E} + j\omega\mathbf{A}) \\ &\mathbf{E} = -\nabla\phi - j\omega\mathbf{A} \end{aligned} \qquad (3.15)$$

Combining this with the second equation in (3.12), the problem becomes:

$$\begin{aligned} &\nabla \cdot (\sigma\mathbf{E}) \Rightarrow -\nabla \cdot \sigma(\nabla\phi + j\omega\mathbf{A}) = 0 \\ &\nabla \cdot \sigma(\nabla\phi) = -\nabla \cdot (j\omega\sigma\mathbf{A}) \end{aligned} \qquad (3.16)$$

Using the indexing scheme as shown in Figure 3.2b, the discretized version of the expression is:

$$\begin{aligned} &(\sum_{n=1}^{6} s_n)\phi_0 - \sum_{n=1}^{6} s_n\phi_n = j\omega\sum_{n=1}^{6}(-1)^{n+1} s_n l_n A_n \\ &s_n = \frac{\overline{\sigma}_n a_n}{l_n} \end{aligned} \qquad (3.17)$$

where s_n is the edge conductance computed from $\overline{\sigma}_n$, the average conductivity of the four voxels containing edge n; a_n is the area of the voxel face normal to edge n; and l_n is the distance from node 0 to node n. The component of external magnetic vector potential, A_n, is also evaluated at the centre of the n-th edge.

Rewriting equation (3.17) produces the update equation:

$$\phi_0 = (\sum_{n=1}^{6} s_n)^{-1} \sum_{n=1}^{6} s_n[\phi_n - j\omega(-1)^n l_n A_n] \qquad (3.18)$$

When the equation is written for every vertex in the computation domain, the result is a heptadiagonal system of equations. The program employs the Conjugate Gradient method to solve the system of equations [32].

The SPFD method is a less computationally demanding method because of its scalar potential formulation. Instead of representing each field by its three components for each

direction, the fields are computed from the scalar electric potential at each node. Dimbylow has compared the efficiency of SPFD and impedance method (IM), which is another popular numerical technique for magnetic field induction problems [19]. He confirmed that SPFD required less memory (475 Mbytes) than IM (540 Mbytes), and computations of identical models were anywhere from about 1.5 to 11 times faster.

However, as with other regular grid finite difference methods, stair-casing error is inherent to the SPFD method. The discrepancies of the maximum values are typically larger, and the error is more significant at the air-conductor interfaces [35]. In order to address this problem, additional layers of voxels assigned with conductive properties are added in each side of the model. These layers are ignored when analyzing the resultant fields.

Our model setup is a special case for this method. In the absence of external magnetic fields, equation (3.17) becomes

$$(\sum_{n=1}^{6} s_n)\phi_0 - \sum_{n=1}^{6} s_n \phi_n = 0 \qquad (3.19)$$

which is in fact the expression for finite difference computation. While we do not really benefit from the efficiency of the SPFD code, using this program allows us the potential to conveniently change to different forms of excitation in the future.

Written in FORTRAN, the SPFD program is compiled and executed on *Minerva*, a high-performance computer at the University of Victoria. Configured to run on a single processor, each SPFD execution occurs on one the 8 nodes of *Minerva* which has a total of eight 375 MHz processors. Although each node is equipped with 8 GB of memory, the 32-bit program can only employ up to 2 GB of memory restricted by hardware architecture [36].

3.2 Cancellous Bone Model

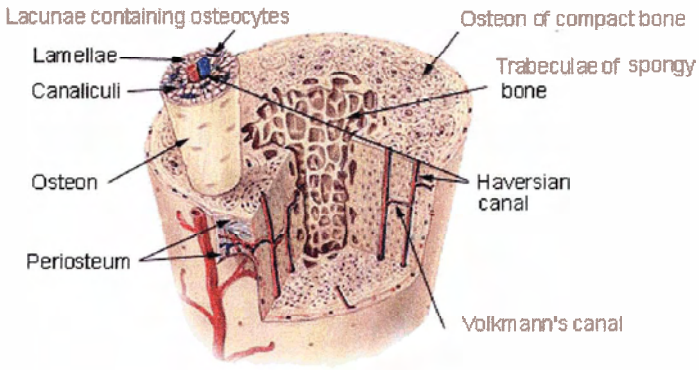

Figure 3.3: Compact Bone and Cancellous Bone [37]

Human skeletal system comprises two types of bone tissues: compact (or cortical) bone and cancellous (also known as spongy or trabecular) bone [37]. Compact bone represents most of the skeletal mass, providing support and protection around every bone in the body [38]. Cancellous bone takes up less of the mass but represents most of the bone surface. Cancellous bone consists of trabeculae and pieces of short bones. These small but rigid pieces are arranged in such a way to reinforce support to the body. Bone marrow is contained in the cavities among the trabeculae as shown in Figure 3.4.

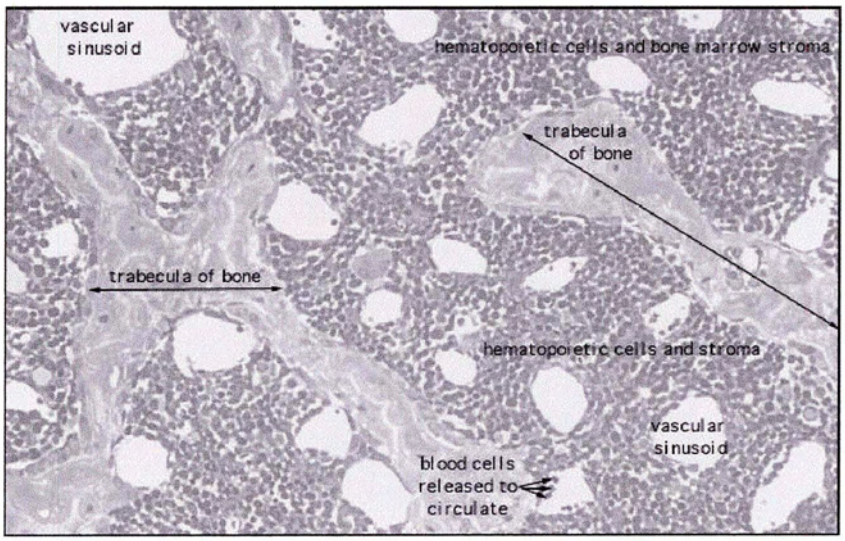

Figure 3.4: Trabeculae among Bone Marrow Cells [39]

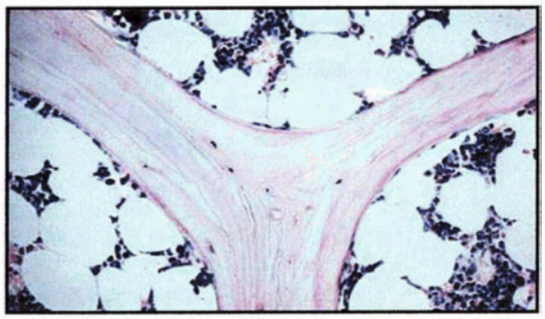

Figure 3.5: Y-shape Trabecula in Bone Marrow Cells [40]

3.2.1 Creation of the Model

Although the database of dielectric properties of tissues provides separated dielectric constant and conductivity values for compact bone, cancellous bone and bone marrow [41], tissue-specific dosimetry calculations usually regard bone marrow as everything inside the compact bone assigned with one set of bulk properties [6]. However, the irregular geometry of the cavities housing bone marrow influences the distribution of EMF. Therefore, the objective of modeling cancellous bone is to examine whether this non-uniform bone sub-structure causes any enhancement in the local electric field.

Instead of creating a cancellous bone model from primitive shapes, a set of micro-CT scan data (courtesy of Dr. B. van Riethergen of the Eindhoven University of Technology) of remodeled cancellous bone, as shown in Figure 3.6, is employed.

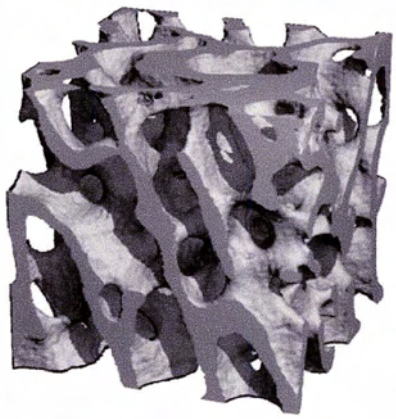

Figure 3.6: Micro-CT Scan Image of Cancellous Bone

The original data consist of 282×282×282 voxels of 14 μm resolution. Due to the limitation imposed by our computer resources, a subset of 150×150×150 voxels is extracted for computations. This subset is chosen by visual inspection to ensure features of trabeculae, short bones as well as pores of various sizes are included. The selection also checked for stray voxels at the boundaries which would introduce artifact to the results. A reconstruction of the subset using the iso-surface feature of MATLAB is shown in Figure 3.7.

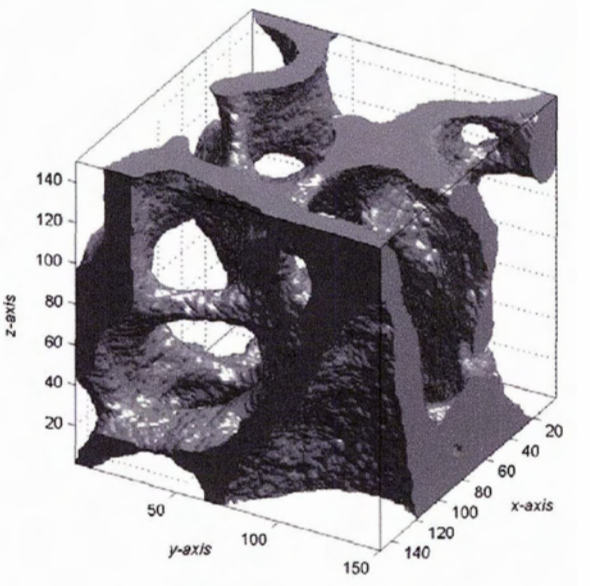

Figure 3.7: Iso-Surface Plot of the 150×150×150 Model

3.2.2 Properties of the Cancellous Bone Model

Despite the convoluted structure, the model consists of only two domains: cancellous bone and bone marrow. For this particular model, the presence of other cells (e.g., blood vessels) and the detailed cellular features (e.g., membrane and cytoplasm) are omitted to limit the scope of the problem.

Whereas bone marrow is in fact a composition of various tissues including adipose tissue, reticular tissue, lymphoid tissue, hematopoietic tissue and blood, it can also be divided into two types – red and yellow [42]. Red bone marrow is richer in erythrocytes (red blood cells), thus is considered more active. It represents a larger percentage of the bone

marrow in children. Over time, red bone marrow gradually converts to yellow bone marrow, which becomes the dominant type in adults. The yellow colour is due to greater proportion of fat cells, thus yellow bone marrow is considered less active.

Dielectric properties of human tissues are typically obtained experimentally and also compared with values estimated by the Cole-Cole expression [41]. At higher frequencies (> 1 MHz), the Cole-Cole model can be used with confidence; at lower frequencies, however, there are few values published in literature, and they show larger variations. Especially with bone, the different components are difficult to isolate and the proper application of measurement probes is challenging. The dielectric values often used in numerical modeling are thus results averaged from measurements and estimations, to the best of present knowledge.

In this computation, the cancellous bone region is assigned a conductivity (σ) of 0.04 S/m, while the heterogeneous bone marrow is treated as homogeneous, with an average conductivity of 0.05 S/m (Cancellous Model A). Since red bone marrow is more predominant in children, Cancellous Model B employs a higher conductivity of 0.07 S/m to first, represent a more realistic model for the study of childhood leukemia; and secondly, examine the parametric dependence of the field on conductivity. In light of the latter, Cancellous Model C uses a bone marrow conductivity of 0.002 S/m, which is the value reported by the Italian National Research Council on dielectric properties of human tissues at 60 Hz [43]. The conductivities of the three models are summarized in Table 3.3.

Table 3.3: Conductivities for Different Cancellous Models

Cancellous Model	Conductivity [S/m]	
	Cancellous Bone	Bone Marrow
A	0.04	0.05
B		0.07
C		0.002

In order to minimize numerical error introduced by the domain boundaries, 15 layers of voxels, with same properties as bone marrow, are added to each side of the cancellous bone model, creating a 180×180×180 matrix. These layers are trimmed off when analyzing the resultant fields. The excitation of the model is applied as boundary condition: while the side faces are defined as magnetic walls (Neumann boundary condition), the top and bottom faces are specified as Dirichlet boundaries, where the bottom plate is grounded ($\phi = 0$ V). The top plate is assigned a voltage to introduce a 1 V/m external electric field to the system. For 180 voxels of 14 μm, $\phi = 2.52$ mV. While this may *not* be a realistic field that one experiences in everyday life, the purpose of this computation is to examine the presence, if any, of local field enhancement.

3.2.3 FEM Implementation of the Cancellous Bone Model

FEM is one of the preferred numerical methods for computations involving biological features largely because of its flexibility to conform to irregular shapes. Cancellous bone is a classical example of a non-uniform structure, but the original data obtained were voxelized already. Although it is possible to import the voxels into FEMLAB, it would defeat the purpose for using FEM. After numerous attempts, the matrix presenting the voxels could be displayed as geometry. However, the re-assembled 3D object showed an amplified stair-casing artifact, and the geometry failed to be properly meshed by the software as well.

Upon consulting the FEMLAB support staff, it was decided that an alternative method be employed. The original steps for solving a problem in FEMLAB can be summarized as follows:

1. create the geometry and enclose it in a domain
2. define subdomains with corresponding dielectric properties
3. set up boundary conditions and excitation
4. generate mesh according to user-defined mesh parameters
5. solve problem iteratively
6. post-processing

The alternate approach omits the creation of the geometry. The domain is defined with its dielectric properties represented by equations. These equations are in turn written to return the interpolated values of the particular property at *any* point within the domain based on the original geometry.

Before applying this method to the cancellous model, it was first validated with more trivial models. A simple test case involves a cubic block of dielectric suspending in a parallel plate capacitor, as shown in Figure 3.8.

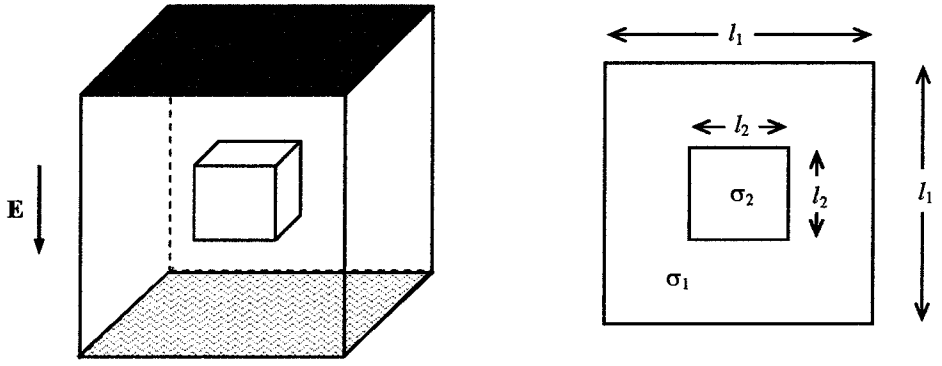

Figure 3.8: Test Case for FEM Implementation

The test case is first solved in FEMLAB with a cubic block defined in the geometry; and then the problem is solved where the domain was hollow, but the dielectric properties are represented by equations describing the presence of the block. Mesh plots of the two scenarios in Figure 3.9 illustrate the difference. Using otherwise identical parameters, the resultant electric fields are in very good agreement with a mean error of less than 0.05%.

Since electrostatic configuration is assumed, only conductivity is involved in solving the PDE. The augmented 180×180×180 voxels cancellous bone model thus is represented by a MATLAB function defining conductivities for a cubic domain of 180×14 μm per side. The code for the conductivity function is listed in Appendix A.

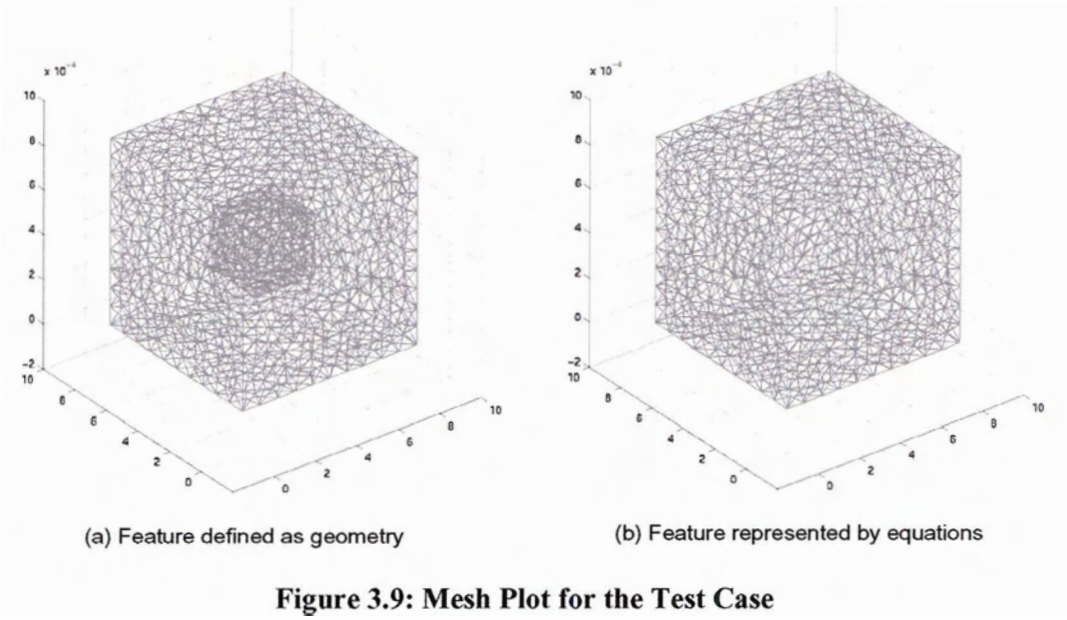

(a) Feature defined as geometry (b) Feature represented by equations

Figure 3.9: Mesh Plot for the Test Case

3.2.4 SPFD Implementation of the Cancellous Bone Model

Voxel is a native format to the SPFD program; therefore, the CT scan data can be incorporated with little modification. The two domains of the cancellous bone model are represented by two different tissue codes: `bone_cancellous` and `bone_marrow`. For electrostatic approximation, only conductivities are specified for each tissue, while relative permittivity is set to unity in both cases.

3.3 Stroma Cell Model I – Single Stroma Cell

Apart from the solid bones, also present in the bone matrix are blood vessels, blood cells, fat cells and numerous types of other cells. Unlike the term "red blood cells" (erythrocytes), which uniquely refers to one type of cells, "bone marrow stromal cells" is a "generic term used to refer to the nonhemopoietic, fixed tissue cells in the medullary cavity" [44] as shown in Figure 3.10. Although much is still to be explored regarding these stromal cells, it is believed that they are essential in the production of blood cells. For example, experiments have shown that stem cells grown *in vitro* fail to differentiate into B-lymphocytes (a type of white blood cells) if stromal cells are absent [46].

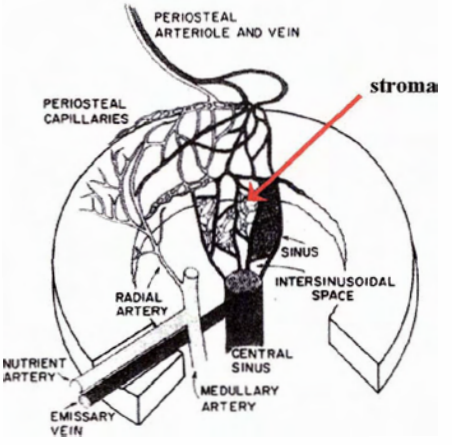

Figure 3.10: Stroma Cells in the Medullary Cavity [44]

Bone marrow stroma cells are distinct from other bone marrow cells in their shapes. Instead of roughly spherical, they are much more irregular, as illustrated in Figure 3.11 where stroma cells are wrapping around blood vessels.

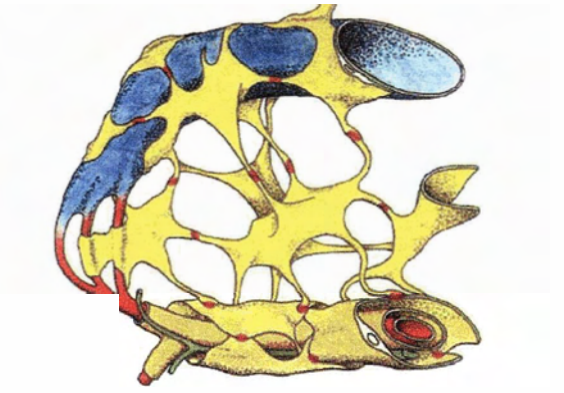

Figure 3.11: Bone Marrow Stroma: The arteriole and capillary are colored red, sinus blue; red dots represent presence of gap junction
(adapted from [45] *with kind permission from ACTA Haematologia Japonica)*

3.3.1 Creation of Stroma Cell Model

The elongated "arms" connecting to neighbouring stroma cells through gap junctions add yet another interesting feature to study. Unlike the cancellous bone model, there is no geometry data readily available for use. Therefore, the geometry of the stroma cell model used in our computations is created from primitive blocks in FEMLAB according to the pictorial views collected as in Figure 3.10 & Figure 3.11 above, as well as Figure 3.12 from an immunology textbook.

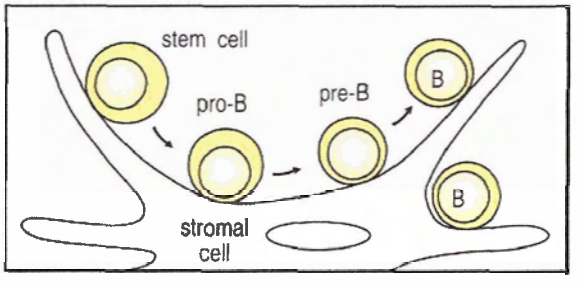

Figure 3.12: Stroma Cell in the Development of B-Lymphocytes
(reproduced from [46] *with kind permission from Garland Science/Taylor & Francis Books, Inc.)*

The geometric features to be emphasized in the model include: non-conductive membrane, funnelling of the arms, presence of gap junctions at adjoining arms, random angles between arms.

Although bone marrow stroma cells are interconnected as in a network, and each cell has multiple arms in various orientation, due to computational limitations, our stroma cell model is a planar model containing a single cell with three arms, each connected to partial arms from adjacent cells.

Based on the 2D schematic illustrated in Figure 3.13, the 3D stroma cell model is created with an ellipsoid and cones scaled in the *y*-direction, resulting in the model as shown in Figure 3.14.

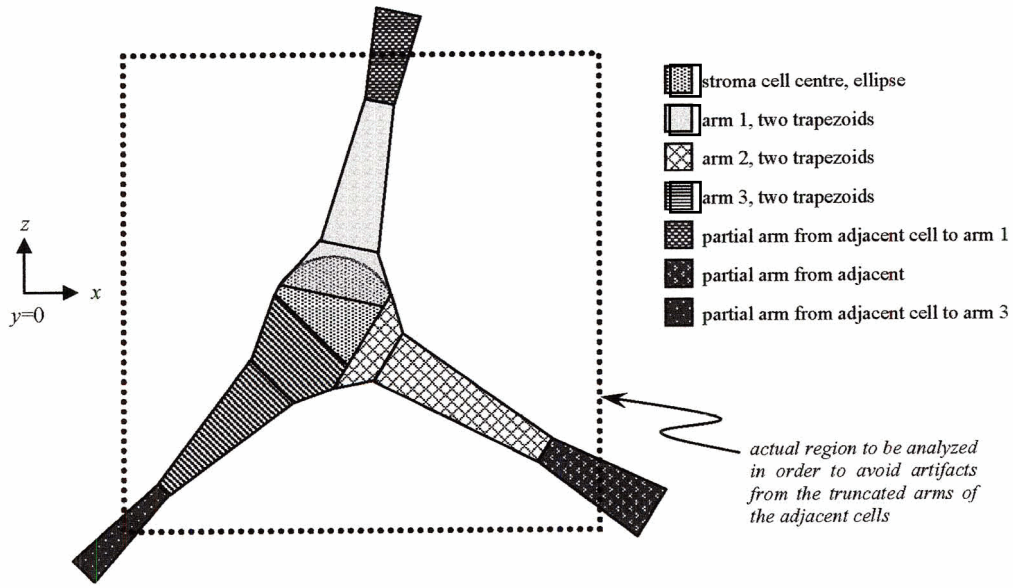

Figure 3.13: 2D Schematic for the Stroma Cell Model

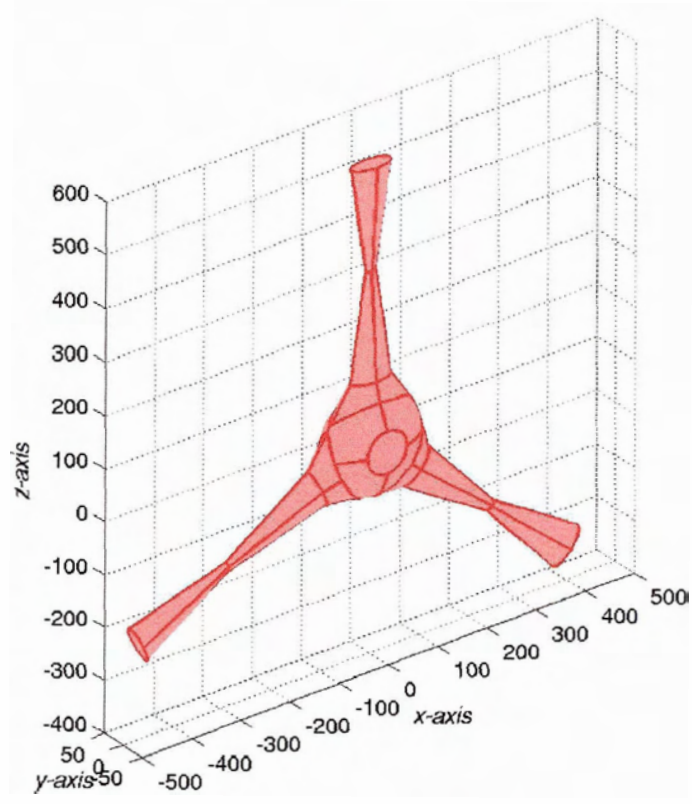

Figure 3.14: 3D Stroma Cell Model in FEMLAB

The base of the stroma cell is the ellipsoid in the middle. The ellipsoid is centred at the origin of the coordinate system. The axes in the x and z-directions are of the same radius (r), while the minor axis in the y-direction defines the *thickness* (t) of the cell. Each arm is made up of three truncated cones (frustums), as illustrated in Figure 3.15. Repeated experiments show that scaling frustum 1 with respect to t in the y-direction, and then truncating the bottom part of the frustum produces a smoother transition from the base to the arm. Figure 3.15 shows the detailed geometry of the i-th arm in the stroma cell model. The heights of the frustums are denoted as a's, while b's are the radii. The arms are rotated about the y-axis from the z-axis at angles α's.

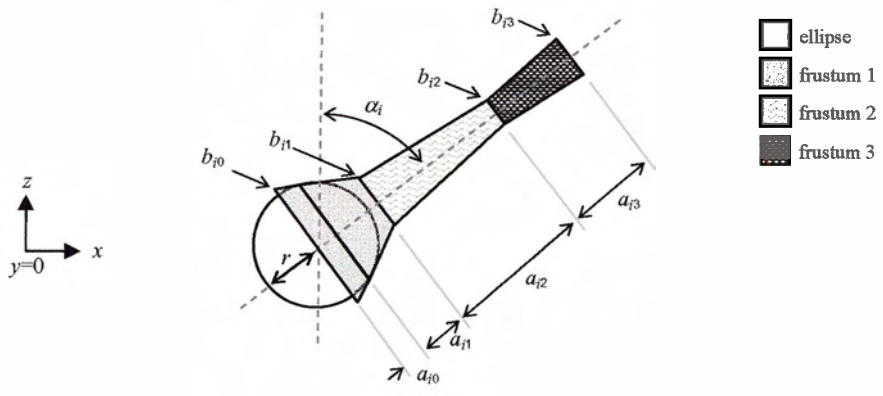

Figure 3.15: Dimensioning One Arm of the Stroma Cell Model

According to researchers we correspond with, typical cancellous bone trabeculae have diameters ranging from 100 to 200 μm, and average pore size is roughly 500 μm. Stroma cells reside within the cancellous bone matrix; however, they are seldom shown clearly in bone marrow smears. Due to the lack of information, and knowing that a bigger cell experiences greater effects due to the surrounding EMF, we assume that a single stroma cell can occupy most of the space of an average pore. Table 3.4 lists the actual dimensions used after taking these considerations into account, and Figure 3.16 shows planar views of the resultant stroma cell. Due to the scaling in the *y*-direction, all the radii in the *y*-direction are one half of those in the *x* or *z*-directions.

Table 3.4: Dimensions of the Stroma Cell Model

[μm]	r	T	a_{i0}	a_{i1}	a_{i2}	a_{i3}	b_{i0}	b_{i1}	b_{i2}	b_{i3}	α_i
Base	100	100									
Arm 1			60	60	200	200	120	40	10	40	0
Arm 2			60	60	200	200	120	40	10	40	-115°
Arm 3			60	60	200	200	120	40	10	40	130°

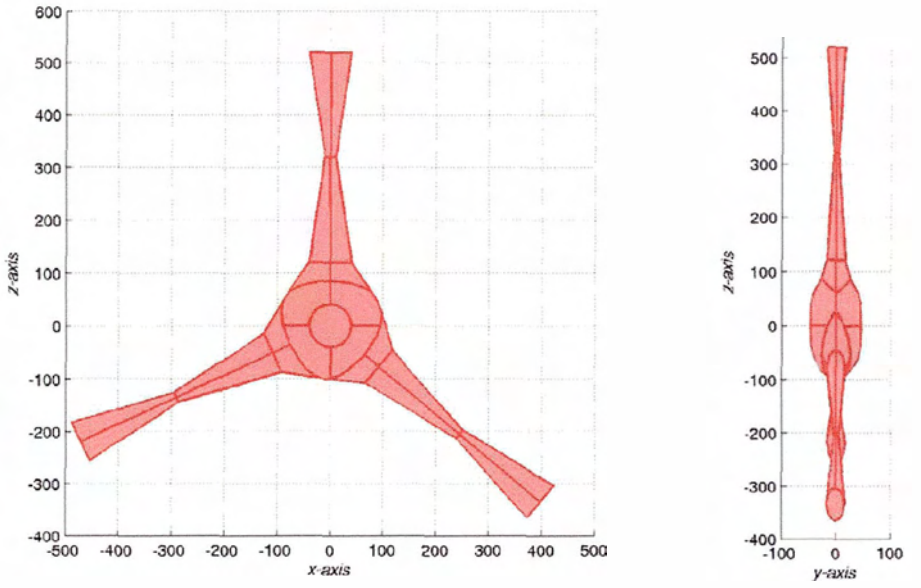

(a) (b)

Figure 3.16: Planar Views of the Stroma Cell Created Using Parameters in Table 3.4: (a) *xz*-plane; (b) *yz*-plane

Although other combinations of values within reasonable ranges would also be possible, some of them cannot be properly meshed or the solutions do not converge. Therefore, this thesis focuses only on this particular set of parameters which contains the best compromised values for a stroma cell model that still maintains sufficient resemblance to the pictorial views in Figure 3.10, Figure 3.11 and Figure 3.12.

The entire stroma cell can also be rotated about the x-axis in such a manner that the major plane would be at an angle to the incident electric field. However, to observe the maximum effect, the cell is placed to align with the incident field.

Since the truncated ends of the partial arms produce singularities that do not belong to the original model, the analysis of the computed field will be trimmed off to include the region only up to the gap connections, as indicated in Figure 3.13.

3.3.2 Electrical Properties of Model

This model consists of only two domains: stroma cell cytoplasm and conductive medium, whilst the membrane is ignored. Provided that the conductivity for blood is estimated to be 0.68 S/m, the medium should have a comparable but slightly lower conductivity; hence 0.50 S/m is chosen to be the conductivity value for the medium. For this computation, the stroma cell itself is assigned the conductivity of bone marrow, where $\sigma_{marrow} = 0.05$ S/m.

3.3.3 Implementation in FEMLAB

Similar to the cancellous cell model, an electric field of 1 V/m is applied in the *z*-direction, and the re-distribution of the field around the stroma cell is observed. The model is computed using both the FEM and SPFD.

The stroma cell model is created as a geometric object in FEMLAB; therefore, the model can be readily meshed and solved in FEMLAB after the computation space and boundary conditions are specified.

As in the cancellous cell model, the computational domain is enlarged to allow sufficient separations to the boundaries, thus minimizing boundary errors. Therefore, although Figure 3.16 shows that a 1000×200×1000 μm space would be sufficient to enclose the model, a 1560×250×1560 domain is defined instead.

3.3.4 Implementation in SPFD

In order to convert the single stroma cell model from FEMLAB geometric object to a format compatible with the SPFD program, the domain number output option of FEMLAB is employed. Domains are enumerated in Femlab. Apart from returning field values as outputs, FEMLAB is also capable of returning domain numbers at any arbitrary points in the computation domain specified. A grid size of 5 μm is chosen to create a 312×50×312 matrix out of the 1560×250×1560 μm domain. A domain number of 1 represents the surrounding medium, while a domain number of 2 denotes the stroma cell.

3.4 Stroma Cell Model II: Gap-Connected Stroma Cells

An important feature of stroma cells is the presence of gap junctions at the connection of two adjoining arms, as indicated in Figure 3.11. Whereas the mechanisms governing the behaviours of gap junctions are beyond the scope of this thesis, it is known that these aqueous channels in the membrane are capable of opening and closing. Figure 3.17 is a diagram of gap junctions made up of connexins at the interface of two adjacent cells. Since the membrane is almost an insulator while cell cytoplasm is fairly conductive, an opened or closed channel would significantly alter the electric potential distribution in the immediate surrounding.

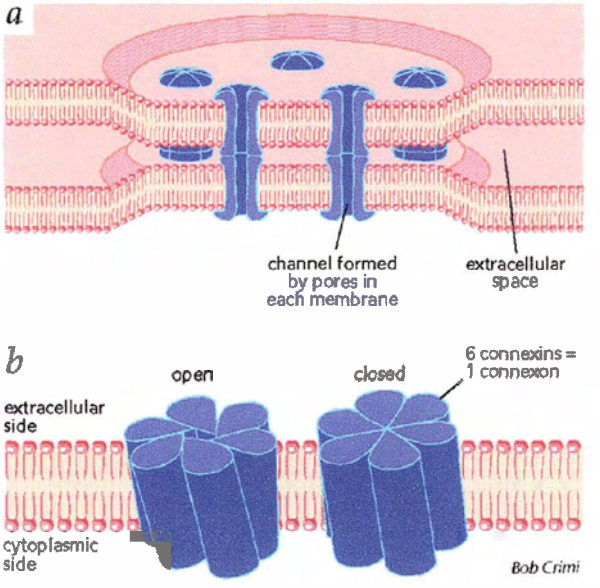

Figure 3.17: Diagram of Gap Junctions: (a) Membranes of two adjacent cells become closely apposed and the connexons of the gap junctions dock with their counterparts in the membrane of the neighbouring cell; (b) Each connexon is made up of six connexins

(adapted from [47] *with kind permission from Nature Genetics © Nature Publishing)*

3.4.1 Computational Method

Typical cell membrane has a thickness of 10 to 30 nm, which creates a huge contrast in dimension compared to the approximated size of roughly 100 μm. Focusing only at the tips where the stroma cells connect to each other, our estimated diameter of the interface is 10 μm, resulting in a ratio of the order of 1:1000. Without the capability of a graded mesh, the SPFD program cannot be readily applied due to the enormous matrix it would otherwise create in order to incorporate one layer of membrane to the stroma cell. Although the FEM should be able to handle more complex geometries with irregular shapes, such contrast in dimension is beyond the capacity of the auto-mesh generator in FEMLAB. Nonetheless, an alternative approach was available where the membrane conductivity is introduced as boundary conditions at the interface of the stroma region to the surrounding medium.

3.4.2 Thin Film Approximation [48]

Consider a "sandwich" structure consisting of a thin layer with thickness δ between two other regions, as shown in Figure 3.18. Current density for the electrostatic model is given by $\mathbf{J} = -\sigma\nabla\phi$, and the equation of continuity defines

$$\nabla \cdot \mathbf{J} = \nabla \cdot \left(-\sigma\nabla\phi\right) = 0 \qquad (3.20)$$

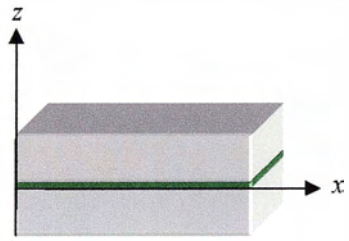

Figure 3.18: Sandwich Structure with a Thin Middle Layer

If the conductivity of the thin layer is small compared with the surrounding materials, it can be assumed that the tangential current density is small while the normal component dominates. In the middle layer, the equation of continuity can be reduced to a

one-dimensional expression as

$$\nabla \cdot \mathbf{J} = \frac{\partial}{\partial z}(-\sigma \frac{\partial \phi}{\partial z}) = -\sigma \frac{\partial^2 \phi}{\partial z^2} = 0 \qquad (3.21)$$

Integrating analytically, the solution for (3.21) is in the form of

$$\phi(z) = az + b \qquad (3.22)$$

where a and b are integration constants.

Let the potential on the lower and upper surfaces of the middle layer be denoted as ϕ_1 and ϕ_2. By placing the origin of the coordinate reference at the lower surface (i.e., $z = 0$), the expressions at the lower and upper surfaces are

$$\begin{aligned} \phi(0) &= b = \phi_1 \\ \phi(\delta) &= a\delta + b = a\delta + \phi_1 = \phi_2 \end{aligned} \qquad (3.23)$$

Rearranging the second expression, the constant a can be solved as

$$a = \frac{\phi_2 - \phi_1}{\delta} \qquad (3.24)$$

Therefore the potential function can be rewritten as

$$\phi(z) = \frac{\phi_2 - \phi_1}{\delta} z + \phi_1 \qquad (3.25)$$

Then current density can be defined as

$$\mathbf{J}_z = -\sigma \frac{\partial \phi}{\partial z} = -\sigma \frac{\phi_2 - \phi_1}{\delta} \qquad (3.26)$$

Provided σ and δ for the thin middle layer are indeed small, the layer can be replaced by inward current boundary conditions to the top and bottom regions. Instead of solving for one unknown, ϕ, for the entire structure, the lower and upper regions are first solved separately for ϕ_1 and ϕ_2. At the interface as highlighted in Figure 3.19, equation (3.26)

is substituted for g in the first boundary condition as listed in Table 3.1. Note that the sign for the lower and upper regions is different due to the reverse direction of current flow when observing in the different regions.

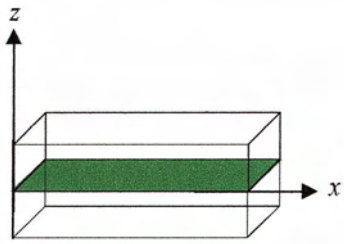

Figure 3.19: Thin Film Approximation of a Sandwich Structure

3.4.3 Simplified Model

Computation of the entire single stroma cell model does not show significant field enhancement. Since the emphasis of this computation is on the gap junction, the model can be reduced to only the gap junction region. Our model assumes the arms of the stroma cell to be on the same plane, and basic electromagnetics theories suggest that the potential drop is sharpest, if the major axis of the geometry is parallel to the applied field; therefore, the simplified model for computation of gap junction TMP shown in Figure 3.20 is chosen.

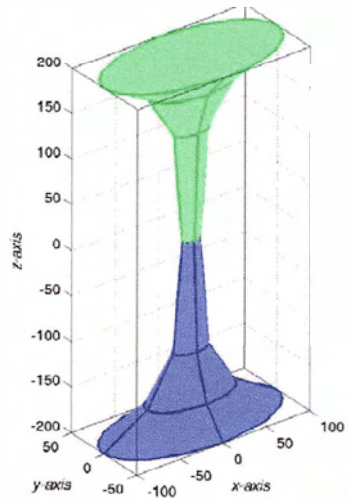

Figure 3.20: Simplified Model for Gap-Connected Stroma Cells: blue and green regions each represent an "arm" of two connected stroma cells

The geometric dimensions are similar to those of the previous model; however, with a smaller computational domain, more details can be implemented and, therefore, the diameter of the "arm" can be changed more gradually. Each arm is presented by three frustums, although the thickness and base radius remain the same (100 μm and 100 μm respectively, resulting in a width of 200 μm). The other radii are 50, 20 and 10 μm respectively, while the lengths are 30, 50 and 120 μm from the shortest to longest.

Due to symmetry, only a quarter of the model needs to be computed to reduce the size of the problem. The actual model for computation is shown in Figure 3.21.

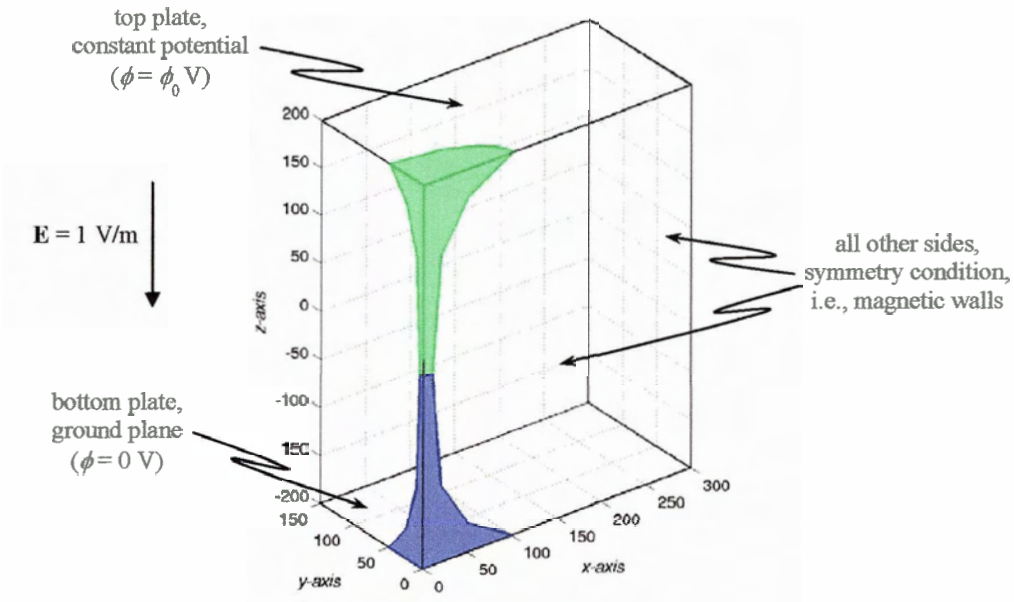

Figure 3.21: Computation Model for Gap-Connected Stroma Cells

Cell biologists suggest that at each gap-connected membrane interface, there exist many tiny channels as illustrated in Figure 3.17. However, to simplify our model, we incorporate the gap junction as a single channel with a larger radius, which is sufficient to represent the collective properties. Therefore, the gap junction is embedded as a quarter of a circle of radius r_{gap}, as shown in the zoomed-in view of Figure 3.22.

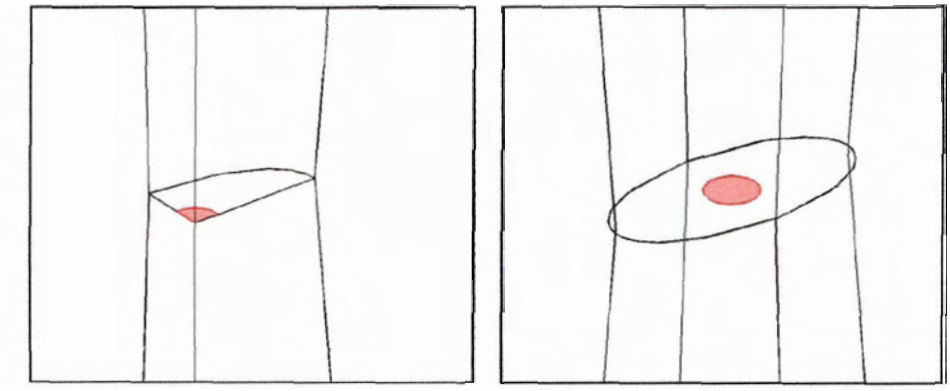

Gap junction embedded in the computational model

Gap junction as represented by the highlighted circle in the entire model

Figure 3.22: Implementation of Gap Junction to the Stroma Cell Model

The diameter of each individual gap junction is as small as a few nanometers. Our cluster of gap junction has a larger diameter of 1 μm, which can be varied.

3.4.4 Electrical Properties of Model

The insulating membrane layer is assumed to have a very low conductivity of $\sigma_{membrane} = 10^{-7}$ S/m. The conductivities for the medium and the inside of the stroma cell (cytoplasm) remain as $\sigma_{medium} = 0.5$ S/m and $\sigma_{cytoplasm} = 0.05$ S/m respectively. The conductivity of the gap junction varies from the completely closed stage, when it equals to $\sigma_{membrane} = 1\times10^{-7}$ S/m, to the completely open stage, when it is equal to $\sigma_{cytoplasm} = 0.05$ S/m.

4. Results

Computational results for different models are tabulated and summarized. Some of the observations are presented here, but more detailed implications will be discussed in the next chapter.

4.1 Cancellous Bone

The field of interest in the computation of cancellous bone model is the electric field. It is expected that the highly irregular geometry will enhance the field in certain areas. The current density distributions are evaluated as well. The orientation of the cancellous bone model is arbitrary; therefore, the analysis focuses on the magnitudes of the field strengths instead of the field vectors.

4.1.1 Method of Evaluation

The cancellous bone model is computed using both the FEM and SPFD methods. FEM meshes consist of tetrahedrons of various sizes, while SPFD employs regular grids. In order to efficiently compare the resultant fields computed by the two different methods, a 3D matrix equivalent to the SPFD grid for the same model is set up in FEMLAB. The post-interpolation option of FEMLAB evaluates values at each of the cells, hence creating matrices comparable to those of the SPFD program.

As discussed in the previous chapter, 15 layers of voxels are added to each side of the cancellous bone model to reduce boundary errors; these layers can be discarded in the evaluation. Furthermore, since the 150×150×150 voxels model is truncated from a larger CT data set, the edges consist of singularities that do not belong to the actual structure. In order to eliminate the artifacts due to these singularities, another 15 layers (10% of the length) of each model are disregarded in the analysis. Hence, out of the 180×180×180 voxels in the entire computational space, only the center 120×120×120 (= 1,728,000) voxels are actually included in the analysis.

The processing of the electric field and current density strength distributions for the cancellous bone model data includes the following aspects:

- cumulative distributions of both the electric field strength and current density for each of the three models, as listed in Figure 4.1, Figure 4.2 and Figure 4.3, respectively

- histograms created by dividing the ranges of field values (as defined by the maximum and minimum values between both methods) into 10 evenly distributed sub-ranges, whose centre values are shown under the plots in Figure 4.4 and Figure 4.5

- statistical values – namely maximum, minimum, mean and standard deviation, 99.5, 99, 1 and 0.5 percentiles – are tabulated in Table 4.1 and Table 4.2 where relative difference (RD) between two values is calculated by the formula:

$$RD = \frac{2|Value_1 - Value_2|}{Value_1 + Value_2}$$

- maximum and minimum values and their respective locations (voxel indices) for each model are listed in Table 4.7 and Table 4.8

Apart from the statistical distribution for the overall matrices, tissue-specific data are also generated by separating the voxels representing cancellous bone and bone marrow. Out of the 1,728,000 voxels evaluated, 456,751 belong to the former, while 1,271,249 fall into the latter category. Their cumulative distributions, histograms and statistical values can be found in Figure 4.6 to Figure 4.11, Figure 4.12 to Figure 4.15, and Table 4.3 to Table 4.6, respectively.

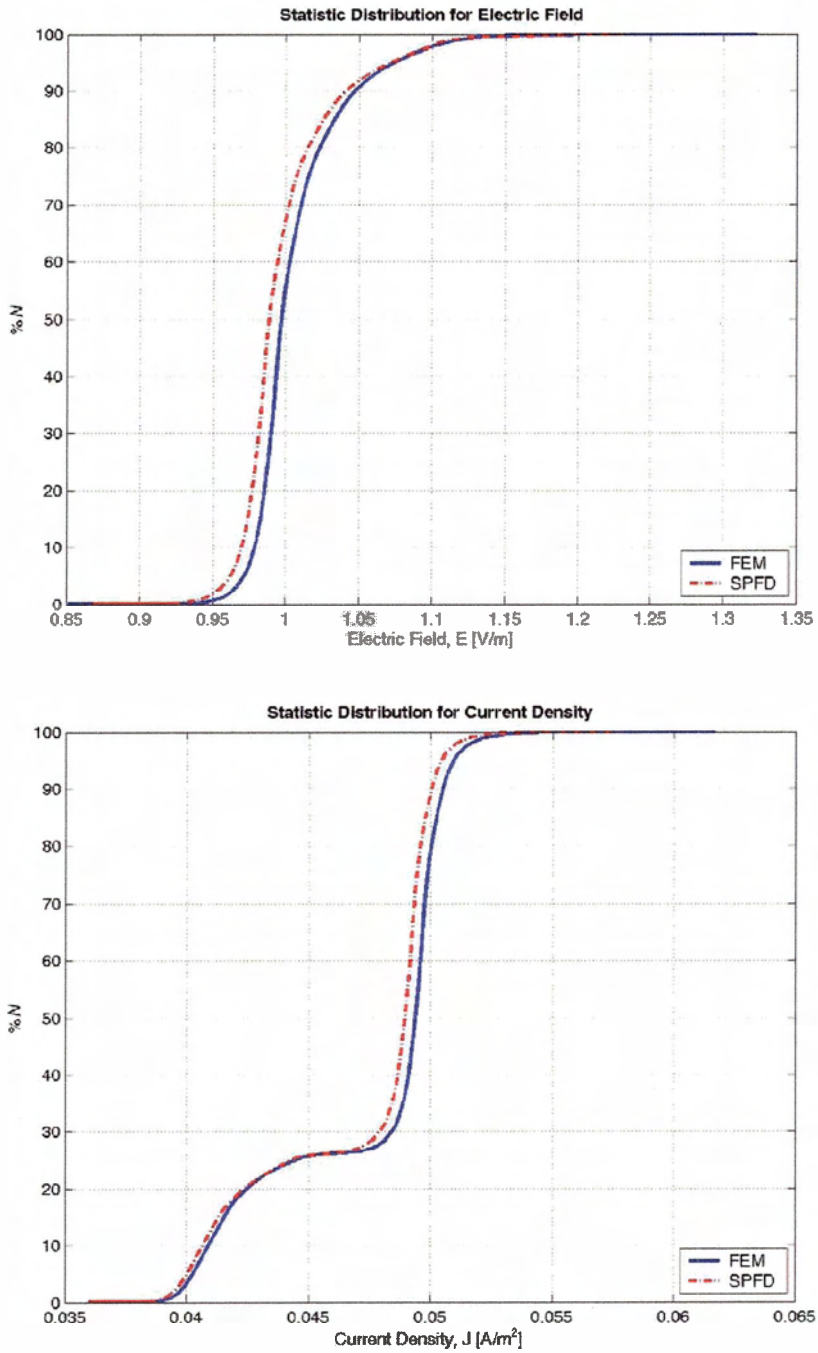

Figure 4.1: Cumulative Distributions for Cancellous Bone Model A

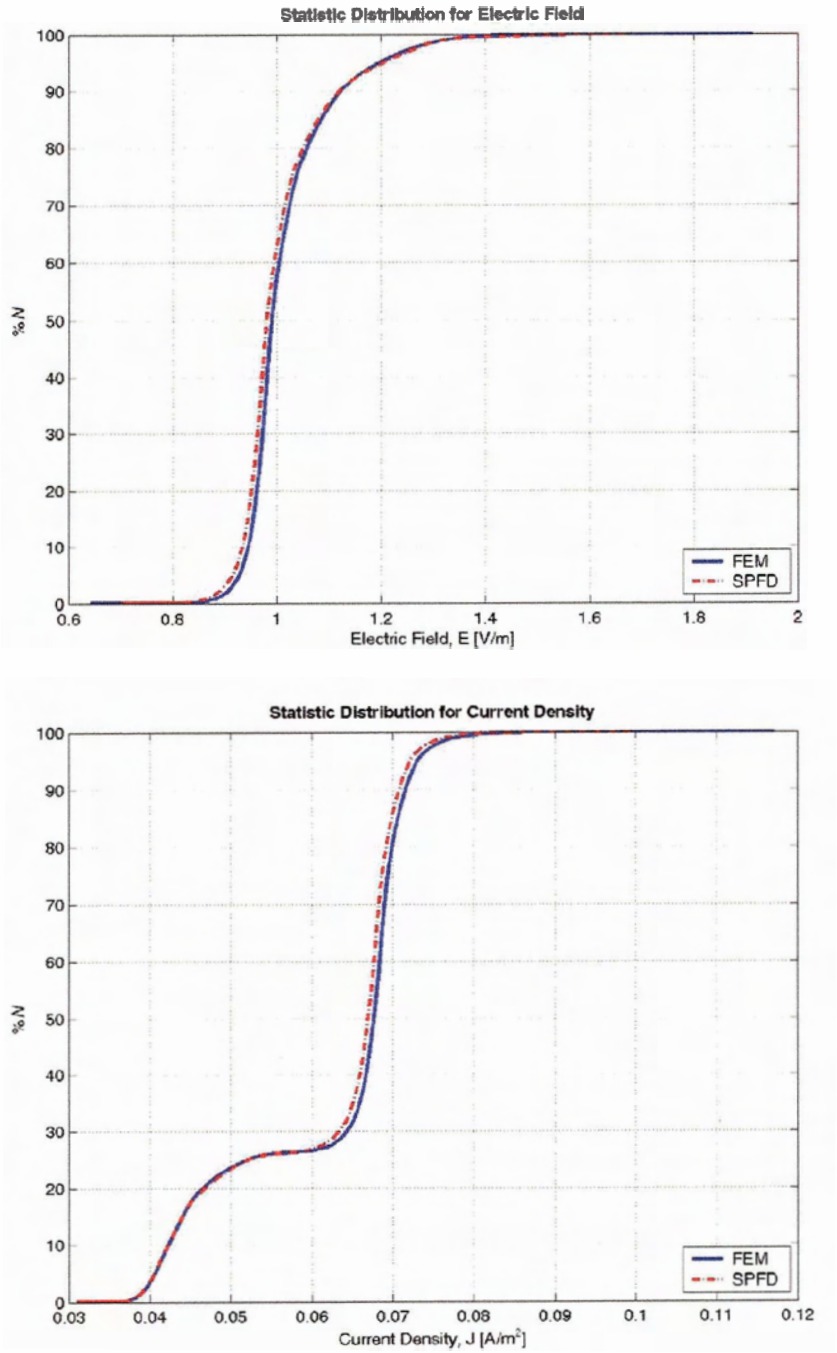

Figure 4.2: Cumulative Distributions for Cancellous Bone Model B

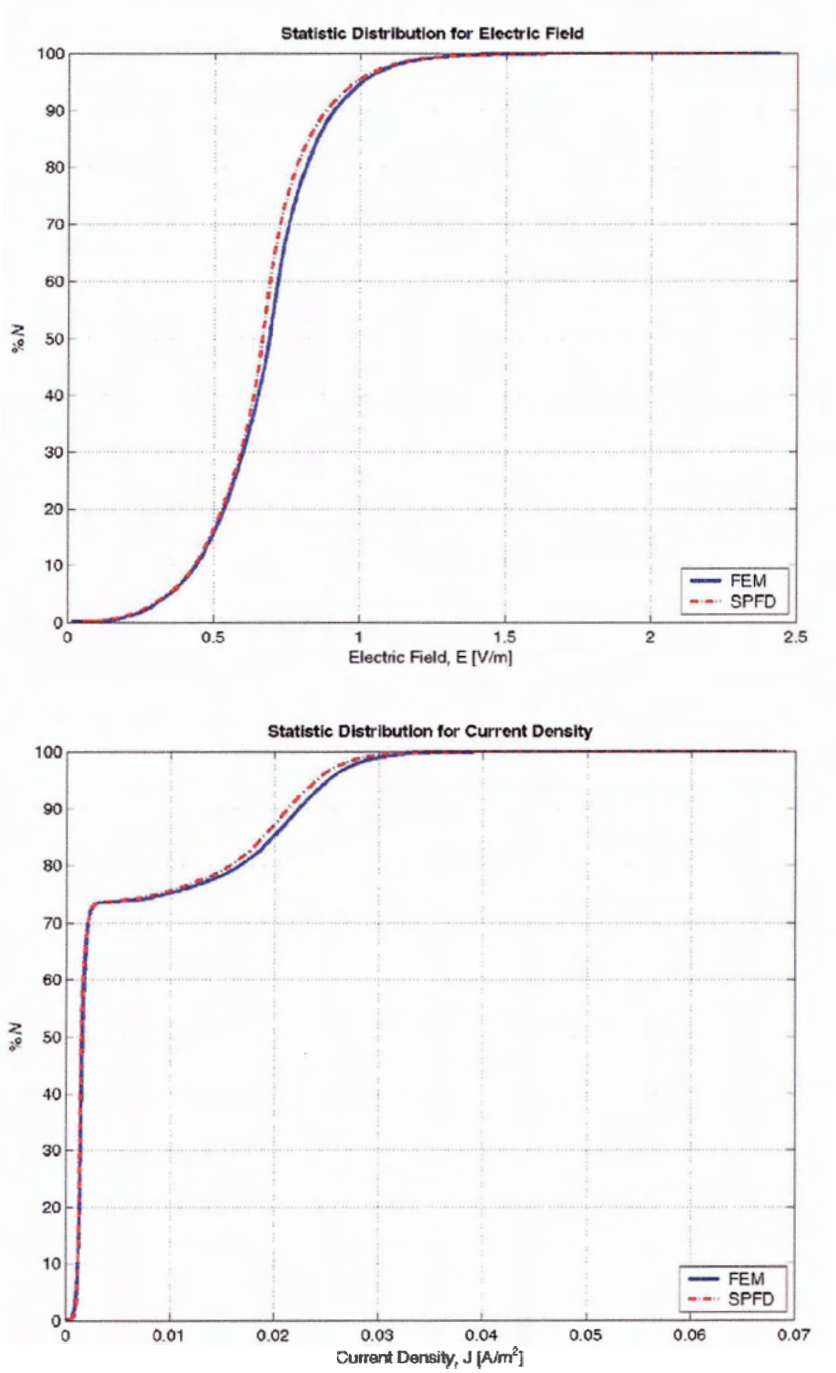

Figure 4.3: Cumulative Distributions for Cancellous Bone Model C

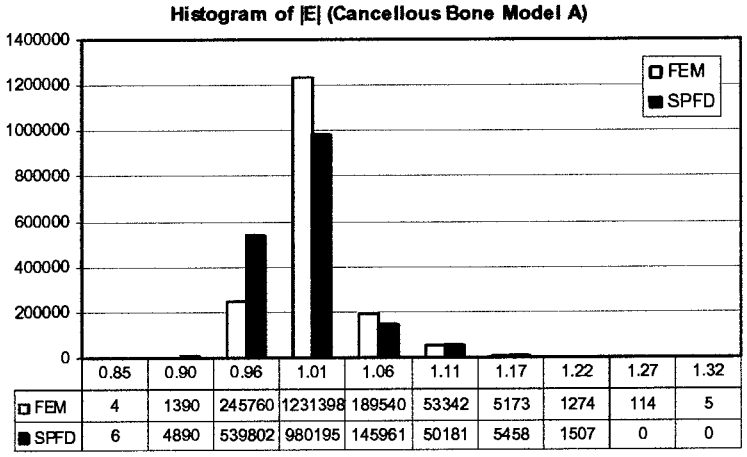

	0.85	0.90	0.96	1.01	1.06	1.11	1.17	1.22	1.27	1.32
FEM	4	1390	245760	1231398	189540	53342	5173	1274	114	5
SPFD	6	4890	539802	980195	145961	50181	5458	1507	0	0

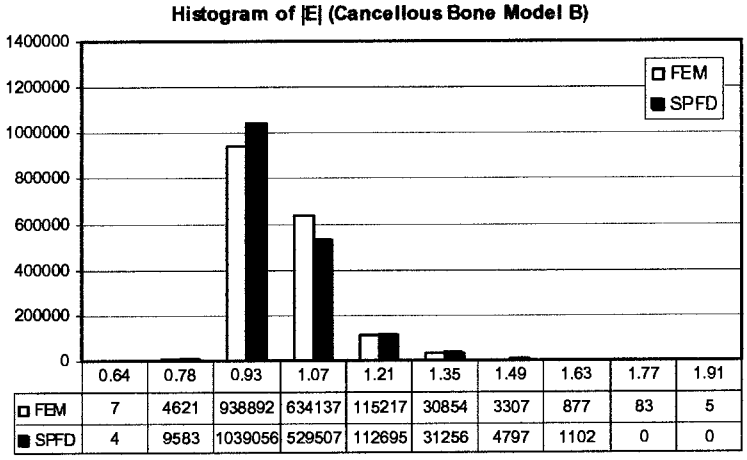

	0.64	0.78	0.93	1.07	1.21	1.35	1.49	1.63	1.77	1.91
FEM	7	4621	938892	634137	115217	30854	3307	877	83	5
SPFD	4	9583	1039056	529507	112695	31256	4797	1102	0	0

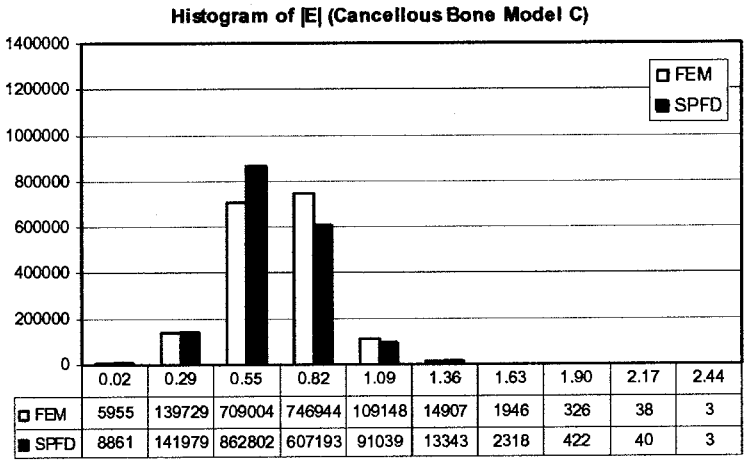

	0.02	0.29	0.55	0.82	1.09	1.36	1.63	1.90	2.17	2.44
FEM	5955	139729	709004	746944	109148	14907	1946	326	38	3
SPFD	8861	141979	862802	607193	91039	13343	2318	422	40	3

Figure 4.4: Histograms of Electric Field Strength

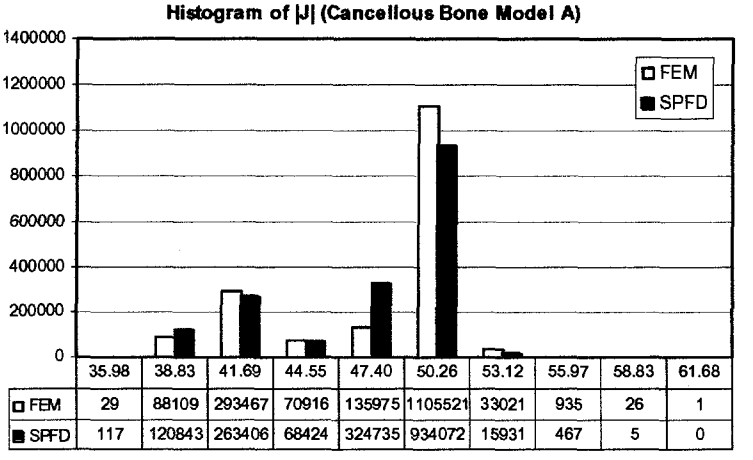

	35.98	38.83	41.69	44.55	47.40	50.26	53.12	55.97	58.83	61.68
FEM	29	88109	293467	70916	135975	1105521	33021	935	26	1
SPFD	117	120843	263406	68424	324735	934072	15931	467	5	0

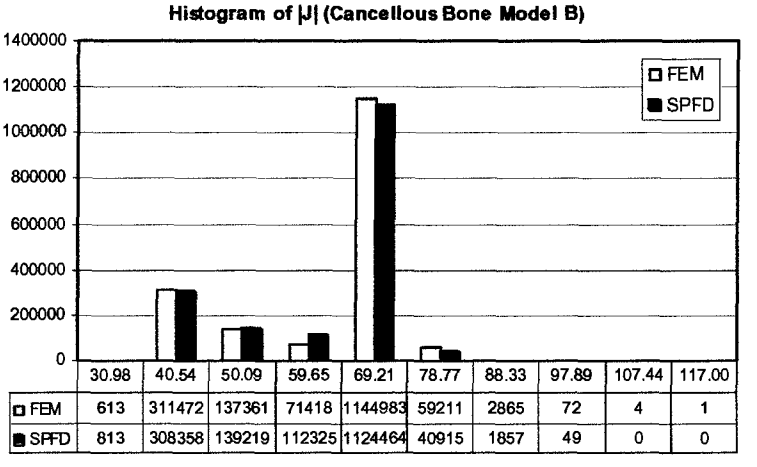

	30.98	40.54	50.09	59.65	69.21	78.77	88.33	97.89	107.44	117.00
FEM	613	311472	137361	71418	1144983	59211	2865	72	4	1
SPFD	813	308358	139219	112325	1124464	40915	1857	49	0	0

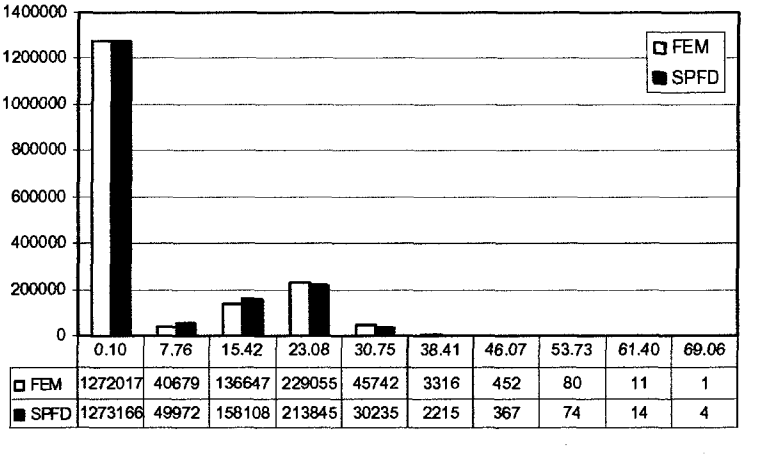

	0.10	7.76	15.42	23.08	30.75	38.41	46.07	53.73	61.40	69.06
FEM	1272017	40679	136647	229055	45742	3316	452	80	11	1
SPFD	1273166	49972	158108	213845	30235	2215	367	74	14	4

Figure 4.5: Histograms of Current Density

Table 4.1: Comparisons of Statistical Distributions for Electric Field

|E| [V/m]	Cancellous Model A			Cancellous Model B			Cancellous Model C		
	FEM	SPFD	RD	FEM	SPFD	RD	FEM	SPFD	RD
Minimum	0.852	0.868	1.90%	0.643	0.702	8.78%	1.57e-2	5.03e-2	104.64%
Maximum	1.32	1.23	7.10%	1.91	1.68	13.10%	2.44	2.38	2.39%
Mean	1.01	1.00	0.80%	1.02	1.01	0.79%	0.684	0.665	2.78%
Standard deviation	3.19e-2	3.36e-2	4.94%	8.50e-2	8.98e-2	5.41%	1.96e-1	1.90e-1	2.73%
$E_{99.5\%}$	1.13	1.13	0.13%	1.36	1.37	0.83%	1.33	1.32	0.79%
$E_{99\%}$	1.12	1.11	0.48%	1.32	1.32	0.06%	1.23	1.22	0.84%
$E_{1\%}$	0.955	0.943	1.21%	0.886	0.869	1.97%	0.208	0.194	7.29%
$E_{0.5\%}$	0.948	0.936	1.25%	0.869	0.852	2.01%	0.168	0.149	12.26%

Table 4.2: Comparisons of Statistical Distributions for Current Density

|J| [mA/m^2]	Cancellous Model A			Cancellous Model B			Cancellous Model C		
	FEM	SPFD	RD	FEM	SPFD	RD	FEM	SPFD	RD
Minimum	36.9	36.0	1.90%	32.1	31.0	3.63%	0.096	0.177	59.47%
Maximum	61.7	57.8	7.10%	117.0	100.0	15.66%	67.3	69.1	2.56%
Mean	47.6	47.2	0.80%	62.3	61.8	0.92%	6.47	6.17	4.70%
Standard deviation	3.75	3.65	4.94%	11.4	11.0	3.07%	8.85	8.42	5.04%
$J_{99.5\%}$	52.9	52.3	0.13%	80.3	78.8	1.95%	32.3	30.9	4.40%
$J_{99\%}$	52.3	51.6	0.48%	77.9	76.6	1.77%	30.3	28.8	4.87%
$J_{1\%}$	39.4	39.2	1.21%	38.5	38.4	0.29%	0.720	0.843	15.81%
$J_{0.5\%}$	39.2	38.9	1.25%	37.9	37.7	0.38%	0.606	0.741	20.09%

4.1.2 General Observations

All electric field distributions as well as tissue-specific current density curves resemble the typical normal distribution, while the current density distributions for the entire model (Figure 4.1b, Figure 4.2b, Figure 4.3b) indicate two peaks. This is consistent with the constitutive relation $\mathbf{J} = \sigma\mathbf{E}$: considering the average electric field in each of the models, the peaks correspond to the two conductivities of the two distinct regions. Since the total

number of bone marrow voxels (1,271,249) is higher than that of cancellous bone (456,751), the peaks corresponding to bone marrow are higher too.

Due to the same reason, for all tabulated values in Table 4.1 to Table 4.6, RDs of the same variable from the same model are identical between electric field and current density.

4.1.3 FEM vs. SPFD

The results for the three cancellous bone models show good agreement between the two computational methods. All pairs of cumulative distribution curves match nicely, as supported by the statistical values. For Cancellous Model A and B, where conductivities of cancellous bone and bone marrow are within the same order of magnitude, RDs for mean and all the percentile values are less than or around 2%.

The cumulative distribution curves clearly show that the resultant fields from SPFD are slightly weaker across all three models. Comparing the RDs across the three models, generally greater discrepancies are observed between the two methods as the two conductivities are more distinct. Also, from the histograms of Model A and B, the results from FEM span slightly wider ranges than SPFD. These differences may be due to the different formulations and grids of the two numerical methods. The FEM mesh for the overall cancellous bone model has 23,812 nodes and 121,363 elements of assorted sizes. The SPFD computation solves for each of the 180×180×180 = 5,832,000 voxels of uniform size. Since there are more bone marrow voxels than cancellous bone voxels, the interpolations in the FEM computation inevitably shifts the average material properties slightly. For Model C, the conductivities are more distinct with $\sigma_{bone\_marrow} << \sigma_{cancellous\_bone}$; the interpolation effects thus are more distributed.

4.1.4 Tissue-Specific Observations

Not only were different conductivities assigned to the different tissues, each of the regions consists of different cells serving unique biological functions. Therefore, tissue-specific results are crucial to the understanding of any potential adverse health effects.

Recalling that $\sigma_{cancellous\_bone}$ is kept constant (0.04 S/m) for all models, while $\sigma_{bone\_marrow} > \sigma_{cancellous\_bone}$ in Model A and B, but $\sigma_{bone\_marrow} << \sigma_{cancellous\_bone}$ in Model C. Comparing the mean values in Table 4.1 to Table 4.6, greater average electric field strengths are obtained for tissue with lower conductivities, and vice versa for the current density.

Table 4.3: Comparisons of Statistic Distributions for Electric Field in Cancellous Bone Voxels

$\lvert E_{bone} \rvert$ [V/m]	Cancellous Model A			Cancellous Model B			Cancellous Model C		
	FEM	SPFD	RD	FEM	SPFD	RD	FEM	SPFD	RD
Minimum	0.923	0.899	2.62%	0.803	0.774	3.63%	1.57e-2	5.03e-2	104.64%
Maximum	1.32	1.23	7.10%	1.91	1.68	13.10%	1.68	1.73	2.56%
Mean	1.04	1.03	0.46%	1.10	1.11	0.11%	0.508	0.482	5.22%
Standard deviation	3.89e-2	4.04e-2	3.80%	1.06e-1	1.10e-1	3.64%	1.50e-1	1.47e-1	2.06%
$E_{99.5\%}$	1.18	1.18	0.48%	1.49	1.52	2.02%	0.915	0.878	4.15%
$E_{99\%}$	1.15	1.16	0.87%	1.41	1.45	2.86%	0.851	0.820	3.73%
$E_{1\%}$	0.974	0.967	0.69%	0.933	0.930	0.39%	0.140	0.119	16.27%
$E_{0.5\%}$	0.968	0.961	0.70%	0.919	0.914	0.44%	0.116	0.100	14.50%

Table 4.4: Comparisons of Statistic Distributions for Current Density in Cancellous Bone Voxels

$\lvert J_{bone} \rvert$ [mA/m^2]	Cancellous Model A			Cancellous Model B			Cancellous Model C		
	FEM	SPFD	RD	FEM	SPFD	RD	FEM	SPFD	RD
Minimum	36.9	36.0	2.62%	32.1	31.0	3.63%	0.630	2.011	104.64%
Maximum	52.9	49.3	7.10%	76.5	67.1	13.10%	67.3	69.1	2.56%
Mean	41.6	41.4	0.46%	44.2	44.2	0.11%	20.3	19.3	5.22%
Standard deviation	1.56	1.62	3.80%	4.24	4.40	3.64%	5.98	5.86	2.06%
$J_{99.5\%}$	47.1	47.3	0.48%	59.4	60.6	2.02%	36.6	35.1	4.15%
$J_{99\%}$	46.0	46.4	0.87%	56.5	58.2	2.86%	34.0	32.8	3.73%
$J_{1\%}$	39.0	38.7	0.69%	37.3	37.2	0.39%	5.59	4.75	16.27%
$J_{0.5\%}$	38.7	38.5	0.70%	36.7	36.6	0.44%	4.65	4.02	14.50%

Table 4.5: Comparisons of Statistic Distributions for Electric Field in Bone Marrow Voxels

$\|E_{marrow}\|$ [V/m]	Cancellous Model A			Cancellous Model B			Cancellous Model C		
	FEM	SPFD	RD	FEM	SPFD	RD	FEM	SPFD	RD
Minimum	0.852	0.868	1.90%	0.643	0.702	8.78%	4.80e-2	8.87e-2	59.47%
Maximum	1.23	1.16	6.54%	1.67	1.43	15.66%	2.44	2.38	2.39%
Mean	0.994	0.985	0.92%	0.983	0.972	1.16%	0.747	0.731	2.19%
Standard deviation	1.75e-2	1.72e-2	1.56%	4.36e-2	4.33e-2	0.88%	1.70e-1	1.59e-1	6.82%
$E_{99.5\%}$	1.06	1.05	1.31%	1.16	1.14	1.95%	1.37	1.36	0.65%
$E_{99\%}$	1.05	1.04	1.31%	1.13	1.11	1.87%	1.27	1.26	0.60%
$E_{1\%}$	0.952	0.940	1.24%	0.879	0.862	2.04%	0.333	0.400	18.11%
$E_{0.5\%}$	0.945	0.933	1.29%	0.862	0.845	2.04%	0.281	0.349	21.76%

Table 4.6: Comparisons of Statistic Distributions for Current Density in Bone Marrow Voxels

$\|J_{marrow}\|$ [mA/m^2]	Cancellous Model A			Cancellous Model B			Cancellous Model C		
	FEM	SPFD	RD	FEM	SPFD	RD	FEM	SPFD	RD
Minimum	42.6	43.4	1.90%	45.0	49.1	8.78%	0.096	0.177	59.47%
Maximum	61.7	57.8	6.54%	117.0	100.0	15.66%	4.88	4.77	2.39%
Mean	49.7	49.3	0.92%	68.8	68.0	1.16%	1.49	1.46	2.19%
Standard deviation	0.874	0.861	1.56%	3.06	3.03	0.88%	0.340	0.318	6.82%
$J_{99.5\%}$	53.2	52.5	1.31%	81.4	79.8	1.95%	2.74	2.73	0.65%
$J_{99\%}$	52.6	51.9	1.31%	79.0	77.5	1.87%	2.54	2.53	0.60%
$J_{1\%}$	47.6	47.0	1.24%	61.6	60.3	2.04%	0.666	0.799	18.11%
$J_{0.5\%}$	47.2	46.6	1.29%	60.4	59.1	2.04%	0.561	0.698	21.76%

Similar to the overall statistics, the results from the FEM computations produce slightly larger values than the SPFD results. Larger variations are observed in the statistical values of Model C; however, tissue-specific statistical values of Model A and B show RDs well below 4%, with the exception of maximum and minimum values.

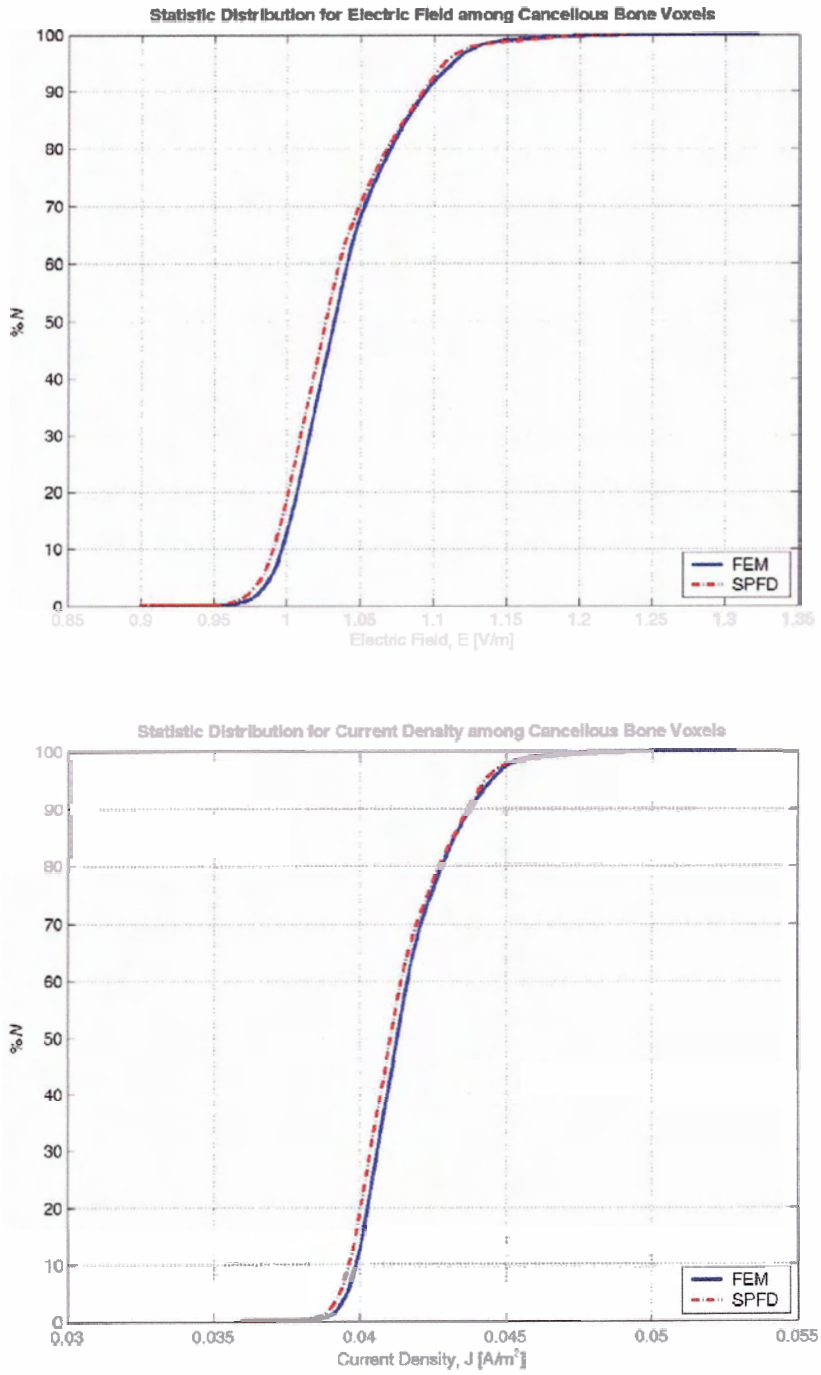

Figure 4.6: Cumulative Distributions of Cancellous Bone Voxels only for Cancellous Bone Model A

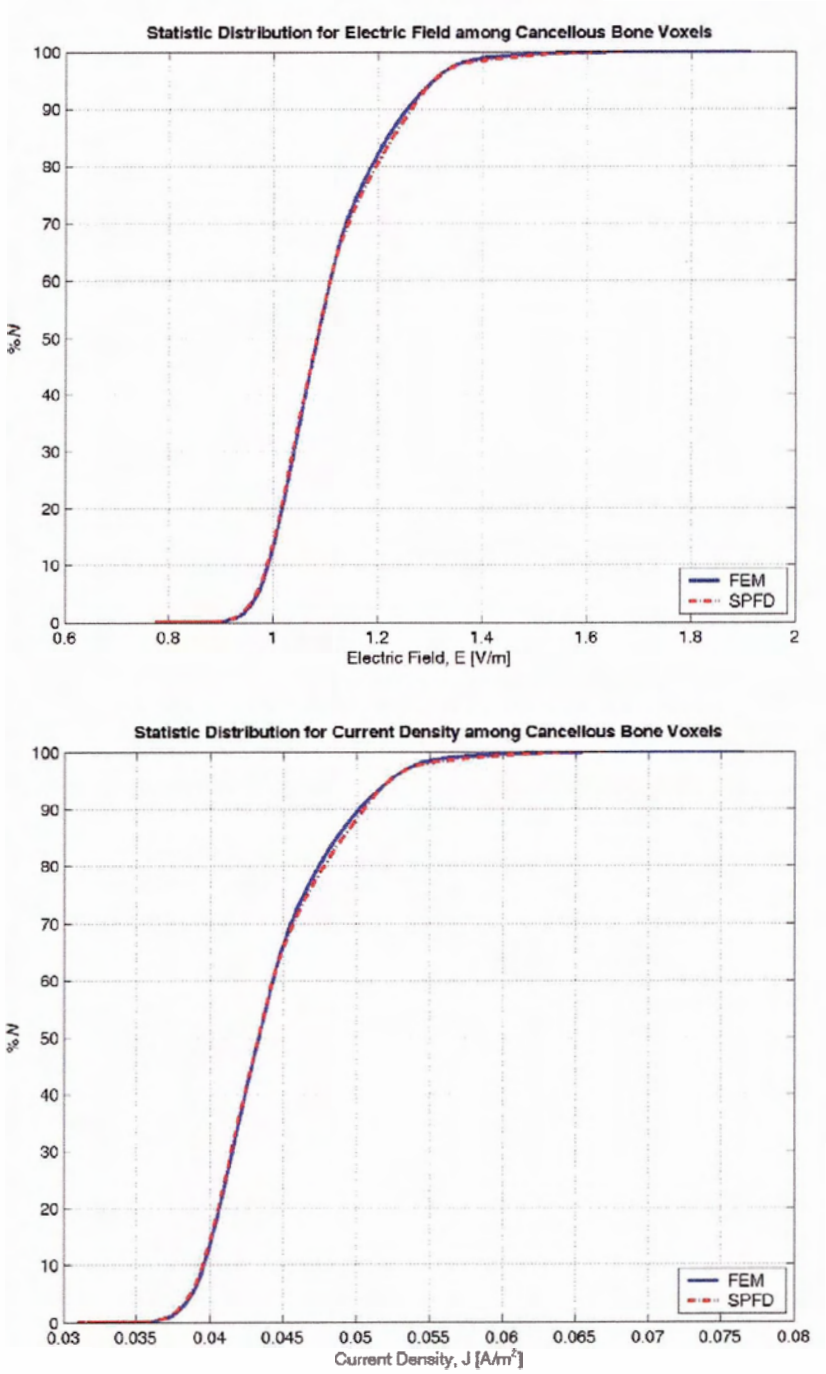

Figure 4.7: Cumulative Distributions of Cancellous Bone Voxels only for Cancellous Bone Model B

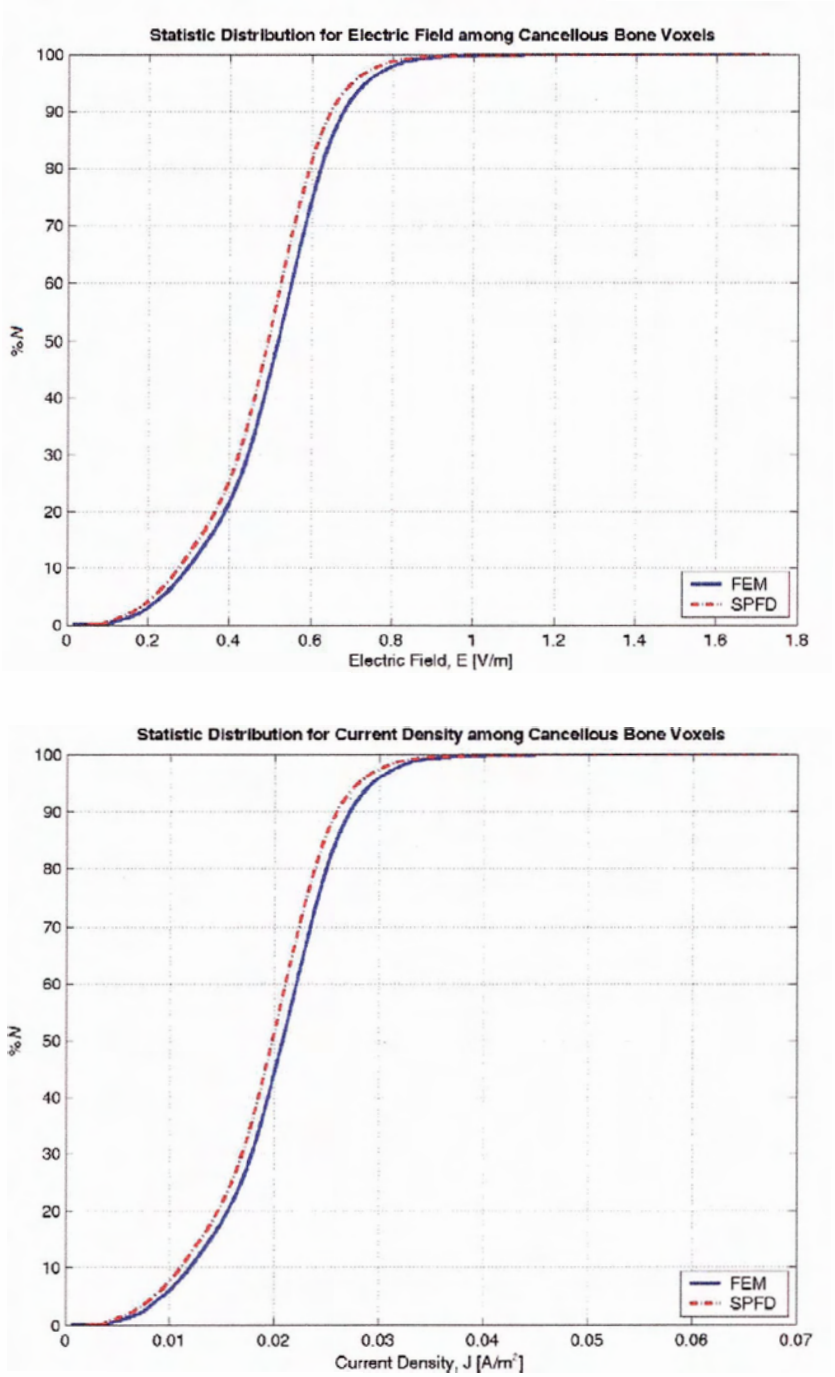

Figure 4.8: Cumulative Distributions of Cancellous Bone Voxels only for Cancellous Bone Model C

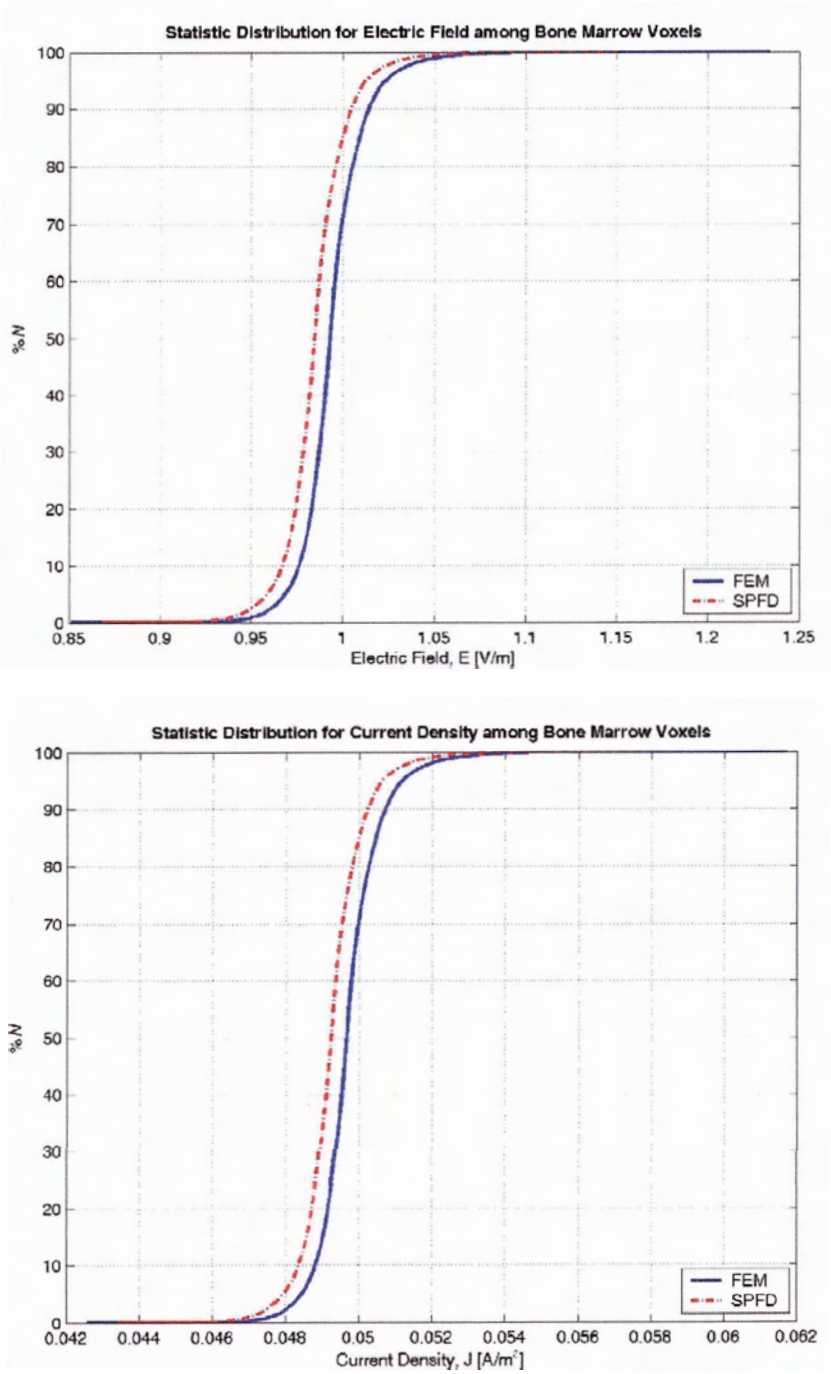

Figure 4.9: Cumulative Distributions of Bone Marrow Voxels only for Cancellous Bone Model A

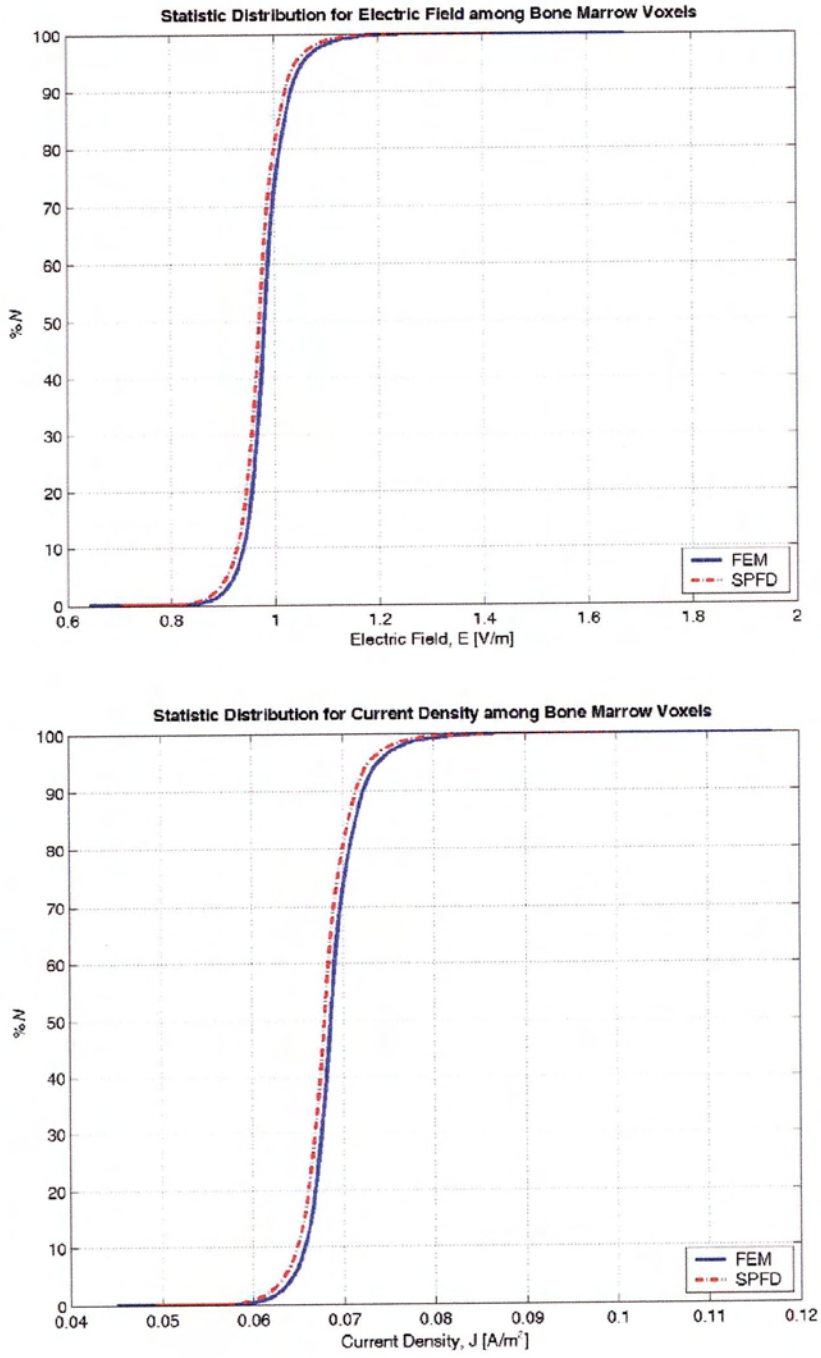

Figure 4.10: Cumulative Distributions of Bone Marrow Voxels only for Cancellous Bone Model B

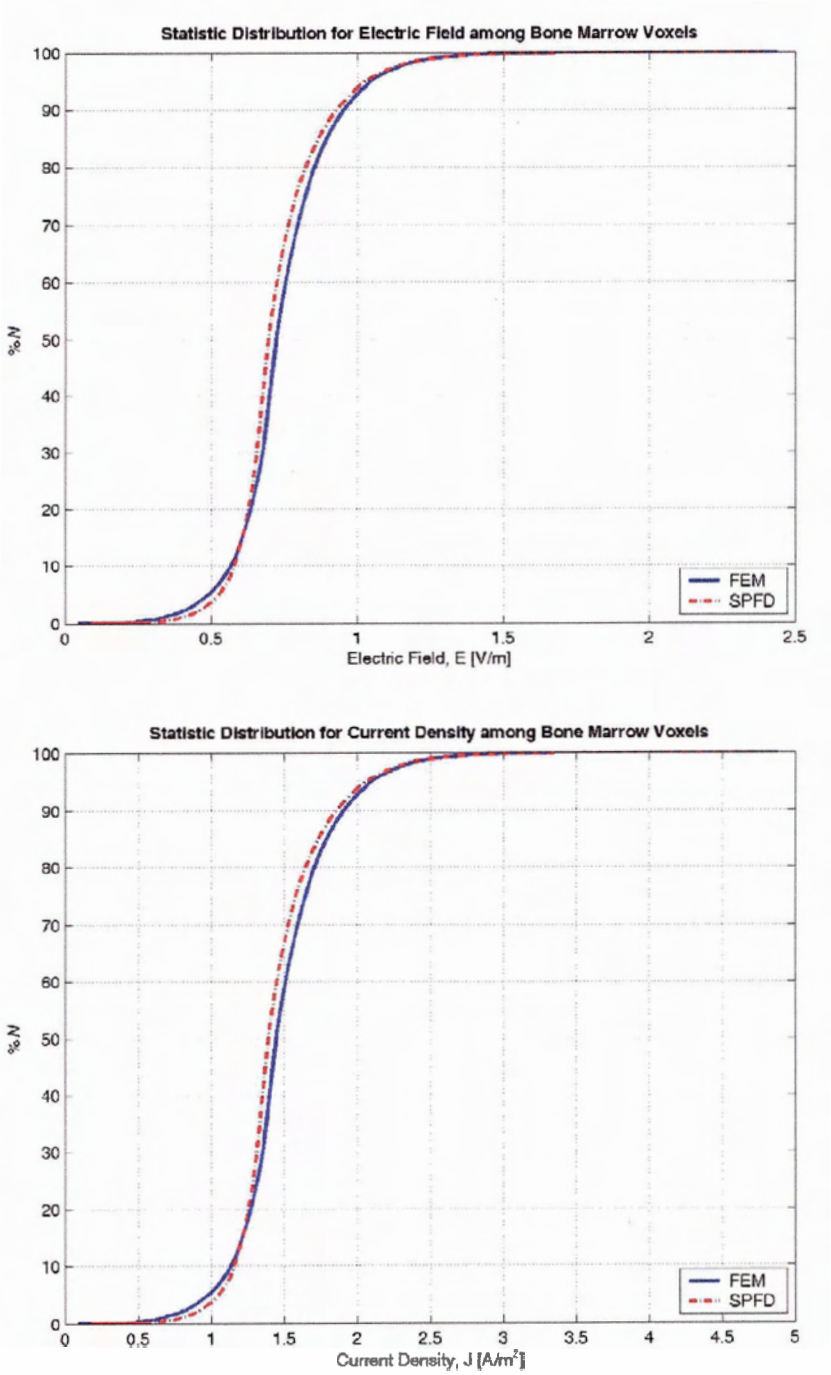

Figure 4.11: Cumulative Distributions of Bone Marrow Voxels only for Cancellous Bone Model C

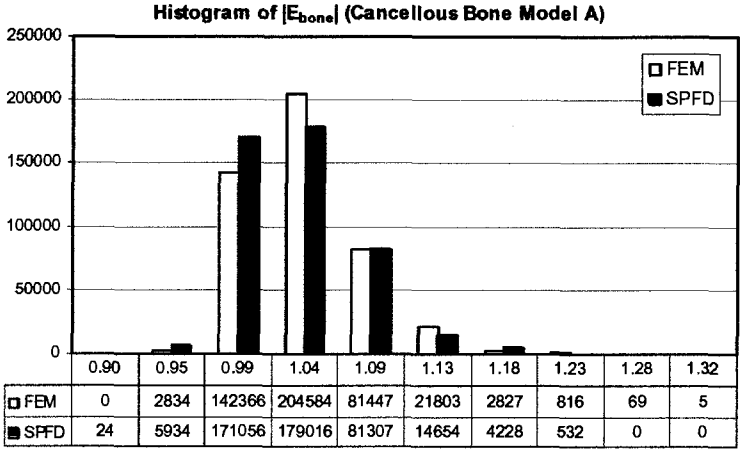

	0.90	0.95	0.99	1.04	1.09	1.13	1.18	1.23	1.28	1.32
FEM	0	2834	142366	204584	81447	21803	2827	816	69	5
SPFD	24	5934	171056	179016	81307	14654	4228	532	0	0

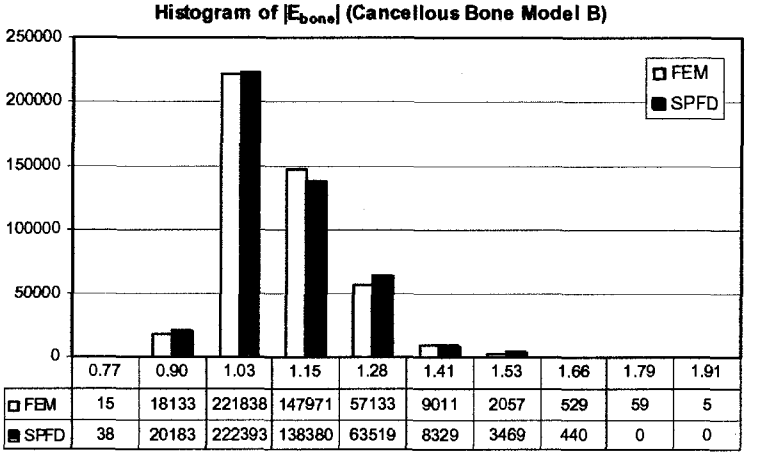

	0.77	0.90	1.03	1.15	1.28	1.41	1.53	1.66	1.79	1.91
FEM	15	18133	221838	147971	57133	9011	2057	529	59	5
SPFD	38	20183	222393	138380	63519	8329	3469	440	0	0

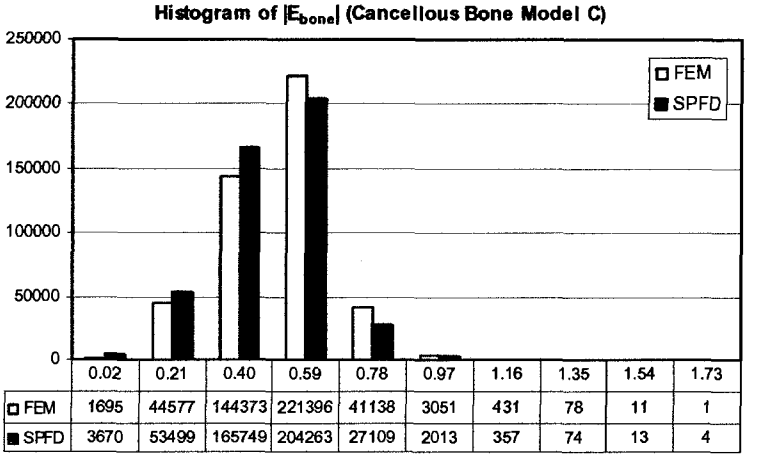

	0.02	0.21	0.40	0.59	0.78	0.97	1.16	1.35	1.54	1.73
FEM	1695	44577	144373	221396	41138	3051	431	78	11	1
SPFD	3670	53499	165749	204263	27109	2013	357	74	13	4

Figure 4.12: Histograms of Electric Field in Cancellous Bone Voxels only

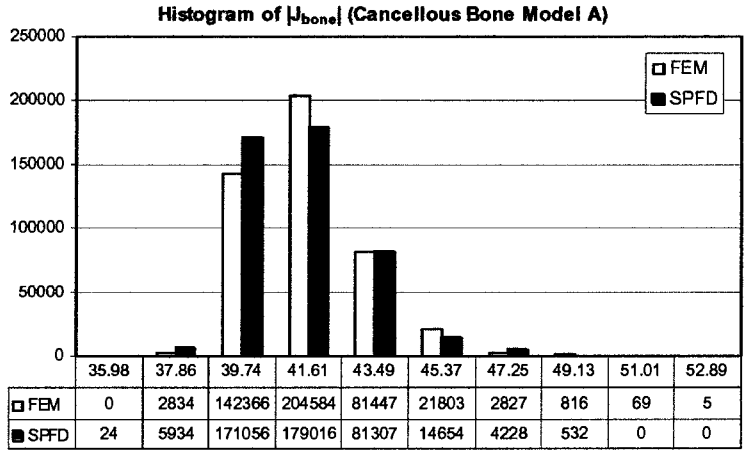

	35.98	37.86	39.74	41.61	43.49	45.37	47.25	49.13	51.01	52.89
FEM	0	2834	142366	204584	81447	21803	2827	816	69	5
SPFD	24	5934	171056	179016	81307	14654	4228	532	0	0

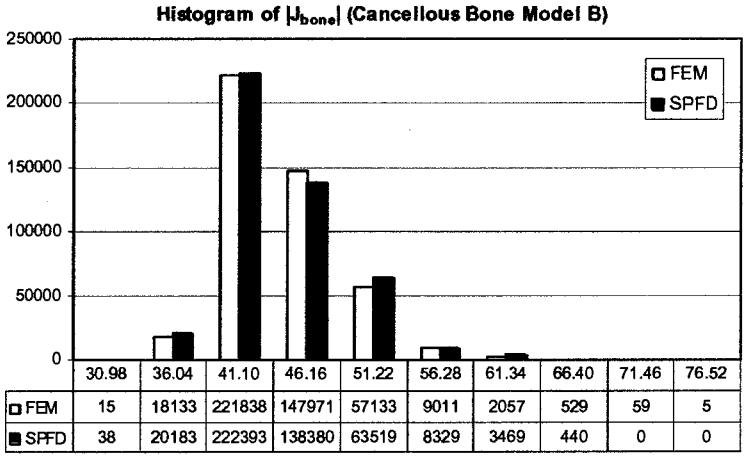

	30.98	36.04	41.10	46.16	51.22	56.28	61.34	66.40	71.46	76.52
FEM	15	18133	221838	147971	57133	9011	2057	529	59	5
SPFD	38	20183	222393	138380	63519	8329	3469	440	0	0

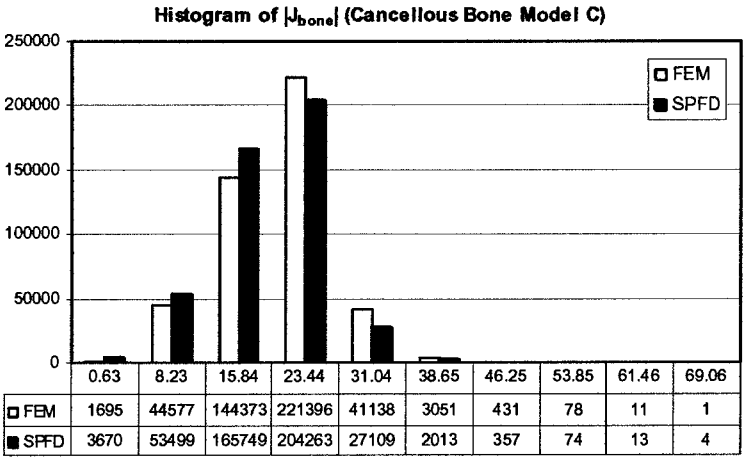

	0.63	8.23	15.84	23.44	31.04	38.65	46.25	53.85	61.46	69.06
FEM	1695	44577	144373	221396	41138	3051	431	78	11	1
SPFD	3670	53499	165749	204263	27109	2013	357	74	13	4

Figure 4.13: Histograms of Current Density in Cancellous Bone Voxels only

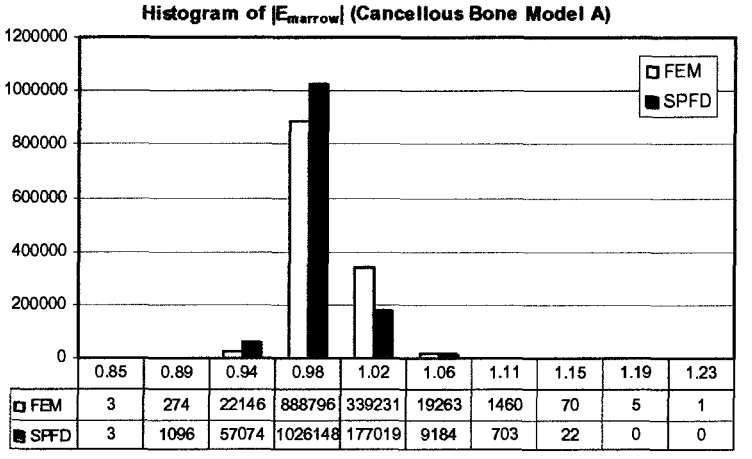

	0.85	0.89	0.94	0.98	1.02	1.06	1.11	1.15	1.19	1.23
FEM	3	274	22146	888796	339231	19263	1460	70	5	1
SPFD	3	1096	57074	1026148	177019	9184	703	22	0	0

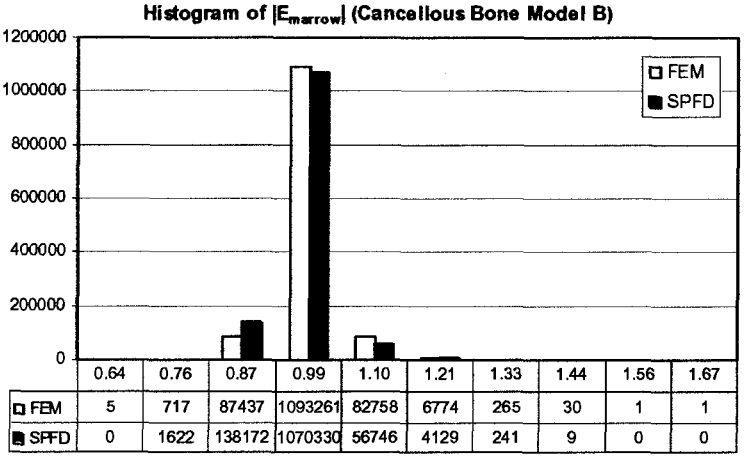

	0.64	0.76	0.87	0.99	1.10	1.21	1.33	1.44	1.56	1.67
FEM	5	717	87437	1093261	82758	6774	265	30	1	1
SPFD	0	1622	138172	1070330	56746	4129	241	9	0	0

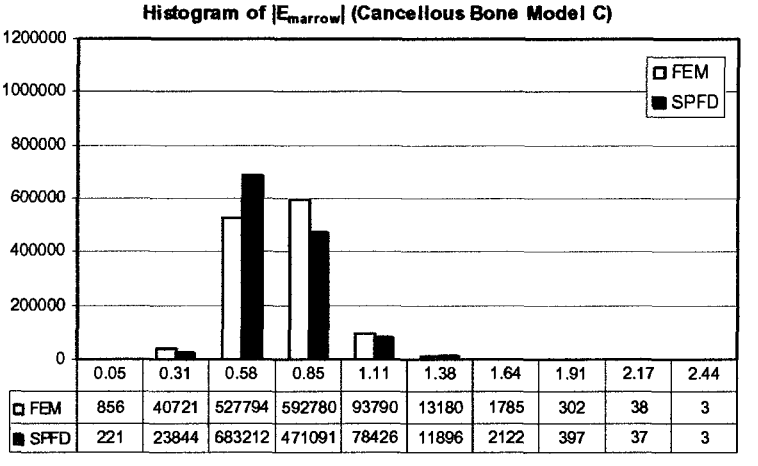

	0.05	0.31	0.58	0.85	1.11	1.38	1.64	1.91	2.17	2.44
FEM	856	40721	527794	592780	93790	13180	1785	302	38	3
SPFD	221	23844	683212	471091	78426	11896	2122	397	37	3

Figure 4.14: Histograms of Electric Field in Bone Marrow Voxels only

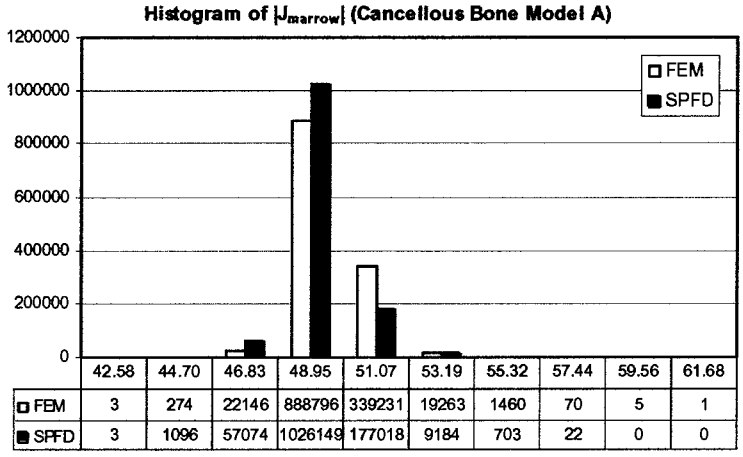

	42.58	44.70	46.83	48.95	51.07	53.19	55.32	57.44	59.56	61.68
FEM	3	274	22146	888796	339231	19263	1460	70	5	1
SPFD	3	1096	57074	1026149	177018	9184	703	22	0	0

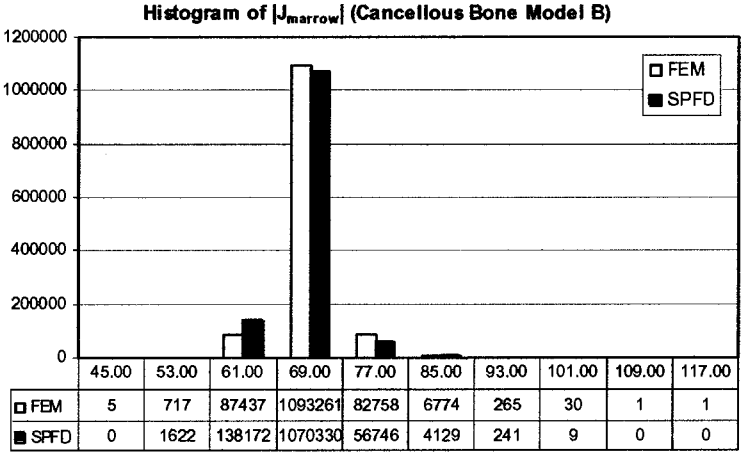

	45.00	53.00	61.00	69.00	77.00	85.00	93.00	101.00	109.00	117.00
FEM	5	717	87437	1093261	82758	6774	265	30	1	1
SPFD	0	1622	138172	1070330	56746	4129	241	9	0	0

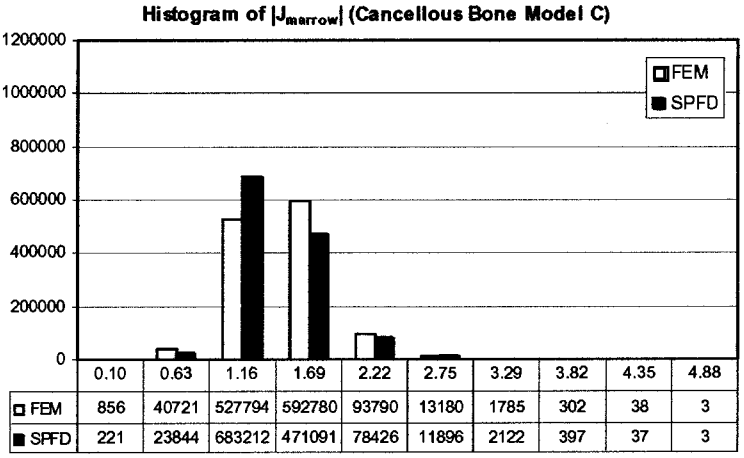

	0.10	0.63	1.16	1.69	2.22	2.75	3.29	3.82	4.35	4.88
FEM	856	40721	527794	592780	93790	13180	1785	302	38	3
SPFD	221	23844	683212	471091	78426	11896	2122	397	37	3

Figure 4.15: Histograms of Current Density in Bone Marrow Voxels only

4.1.5 Maxima and Minima

It is known that disagreement between two computational methods is usually more prominent at extrema. Therefore, apart from comparing the values at extrema, the locations of the extrema are represented as matrix indices.

Examining the maxima and minima for each model, it is confirmed that for the electric field, the maxima are found at the tissue with lower conductivity, while the minima are located within the tissue with higher conductivity; and for the current density, it is just the reverse. Table 4.7 and Table 4.8 list the values and locations of the electric field and current density extrema for the three models respectively.

Table 4.7: Maxima and Minima of Electric Field Distributions

|E| [V/m]	Cancellous Model A		Cancellous Model B		Cancellous Model C	
	FEM	SPFD	FEM	SPFD	FEM	SPFD
Maximum	1.32	1.23	1.91	1.68	2.44	2.38
Voxel index of Maximum	<111,19,6>	<107,23,3>	<111,19,6>	<107,23,3>	<83,36,120>	<89,40,120>
Minimum	0.852	0.868	0.643	0.702	1.57E-02	5.03E-02
Voxel index of Minimum	<45,50,79>	<4,73,23>	<45,50,79>	<4,74,23>	<119,28,4>	<105,21,6>

Table 4.8: Maxima and Minima of Current Density Distributions

|J| [mA/m^2]	Cancellous Model A		Cancellous Model B		Cancellous Model C	
	FEM	SPFD	FEM	SPFD	FEM	SPFD
Maximum	61.7	57.8	117.0	100.0	67.3	69.1
Voxel index of Maximum	<102,32,2>	<109,19,6>	<102,32,2>	<102,20,4>	<41,120,34>	<38,120,37>
Minimum	36.9	36.0	32.1	31.0	0.096	0.177
Voxel index of Minimum	<25,79,73>	<38,120,37>	<25,79,73>	<38,120,37>	<103,34,59>	<108,19,6>

All the extrema for Model A and Model B are located at the same voxel or vicinity for the same method. Plots of the electric field distributions in 3D and cross-sectional views can be found in Figure 4.16 to Figure 4.19. Due to the identical locations between Model A and B, only results from Model B and Model C are included.

Except for the minimum values of Model A and B, although the location indices for the FEM and SPFD results are different, the cross-sectional plots indicate that they are actually in the same region, or around the same geometric features. For example, the electric field maxima for Model A and B are located in a relatively large piece of trabecula encapsulating a small hole which can be seen from the first cross-sectional plane of Figure 4.16. Also, it should be noted that the minimum electric field for Model C, where $\sigma_{cancellous\_bone} > \sigma_{bone\_marrow}$ as opposed to $\sigma_{bone\_marrow} > \sigma_{cancellous\_bone}$ as in Model A and B, occurs at the same region too. This observation confirms the role of geometry in field distribution.

4.1.6 Distribution of Fields

Although the statistical results show good agreements, the field distribution plots from SPFD are clearly smoother than those of the FEM. The latter appeared to be "patchy", and the geometry borders are not as clearly defined. As described in the previous section, the FEM mesh is created without the geometry. Hence the boundaries for the cancellous bone are expected to be fuzzy. Nonetheless, the comparable statistic values prove that it is still a satisfactory approach.

Figure 4.16: Locations of Electric Field Maxima (Cancellous Model B)

The maxima are indicated by the intersections of the dotted lines in each figure. On the left column are 3D plots of the *xy*, *yz* and *zx*-planes on which the maxima are located. The view angles are adjusted to obtain best viewing of the features. On the right column are cross-sectional *xy*-planes. The geometry overlaid on the field distributions is represented by the black solid line. Note that the color scales are different to optimize viewing of each set of data.

Computed by FEM

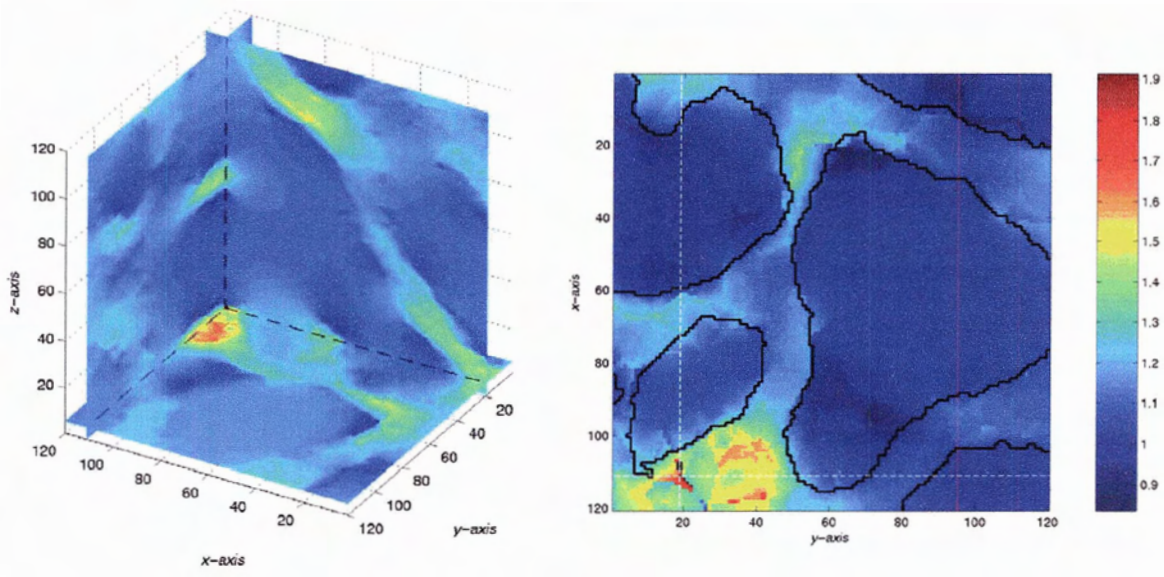

Computed by SPFD

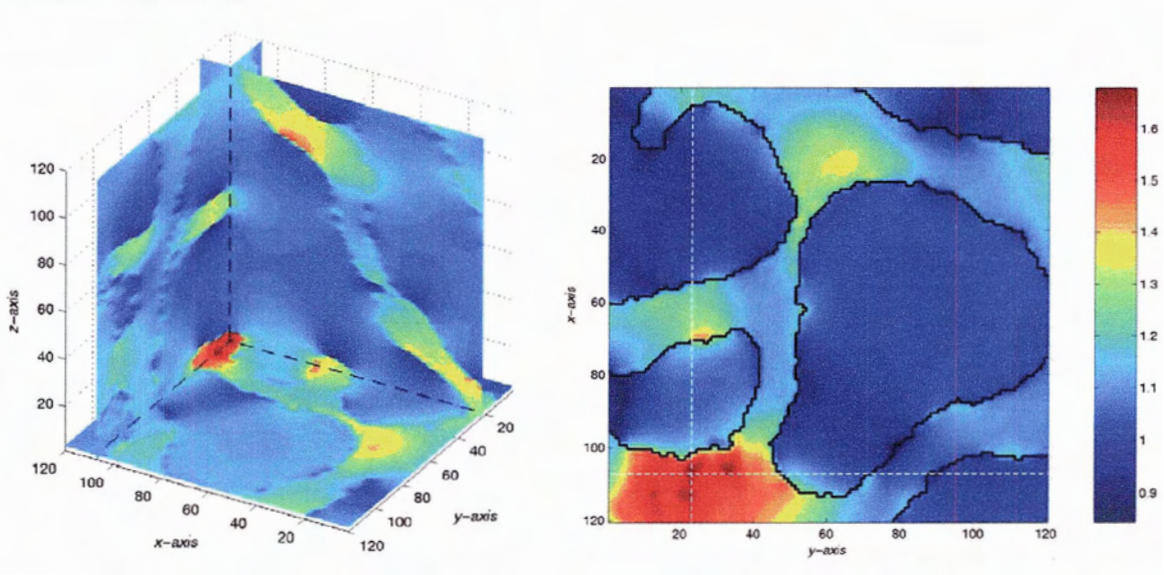

Figure 4.17: Locations of Electric Field Minima (Cancellous Model B)

The minima are indicated by the intersections of the dotted lines in each figure. On the left column are 3D plots of the *xy*, *yz* and *zx*-planes on which the minima are located. The view angles are adjusted to obtain best viewing of the features. On the right column are cross-sectional *xy*-planes. The geometry overlaid on the field distributions is represented by the black solid line. Note that the color scales are different to optimize viewing of each set of data.

Computed by FEM

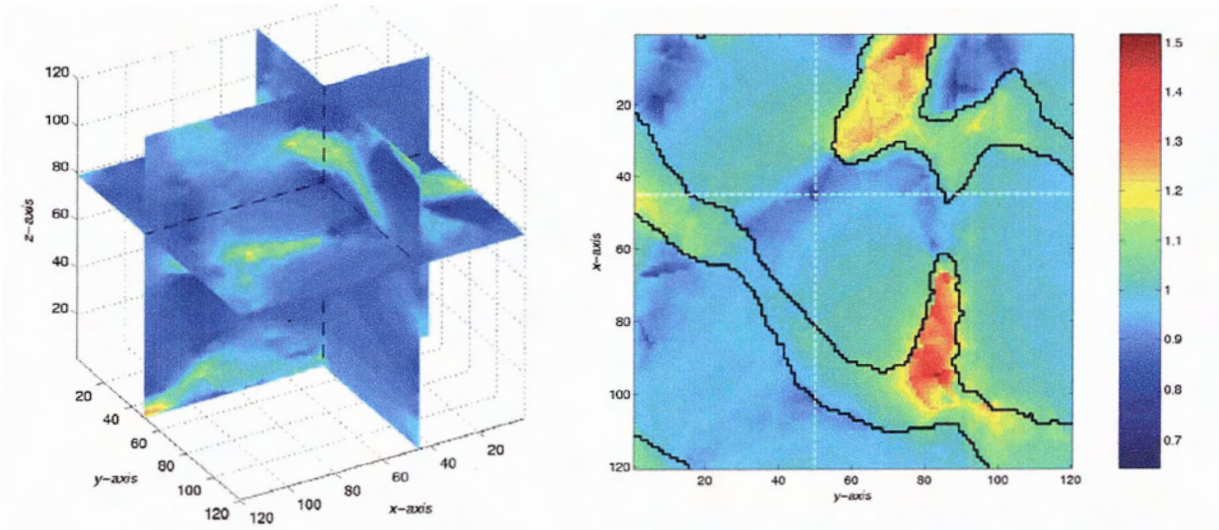

Computed by SPFD

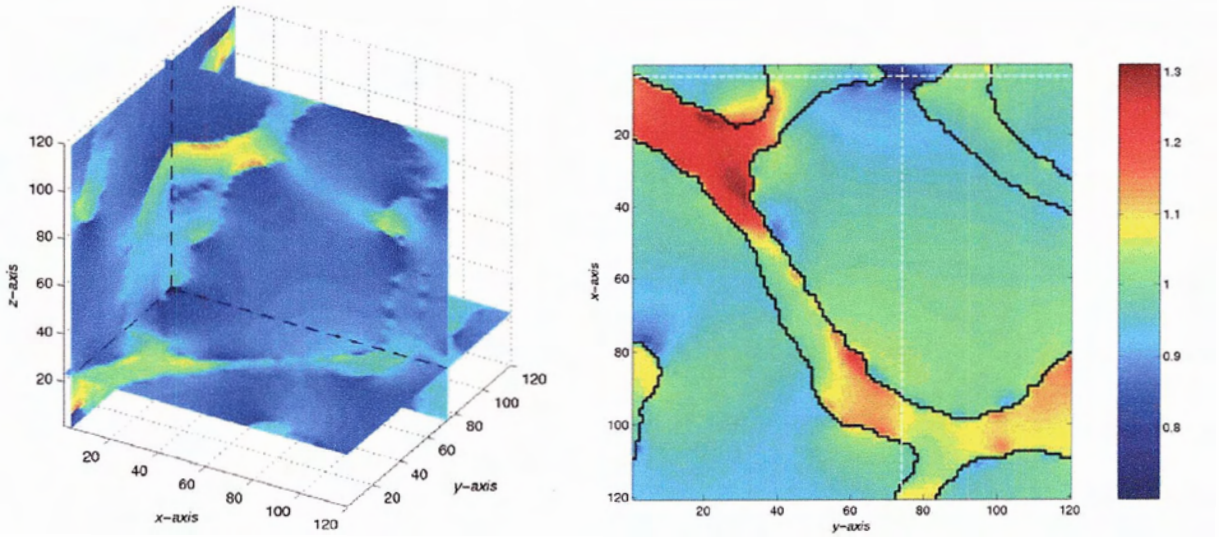

Figure 4.18: Locations of Electric Field Maxima (Cancellous Model C)

The maxima are indicated by the intersections of the dotted lines in each figure. On the left column are 3D plots of the *xy*, *yz* and *zx*-planes on which the maxima are located. The view angles are adjusted to obtain best viewing of the features. On the right column are cross-sectional *xy*-planes. The geometry overlaid on the field distributions is represented by the black solid line. Note that the color scales are different to optimize viewing of each set of data.

Computed by FEM

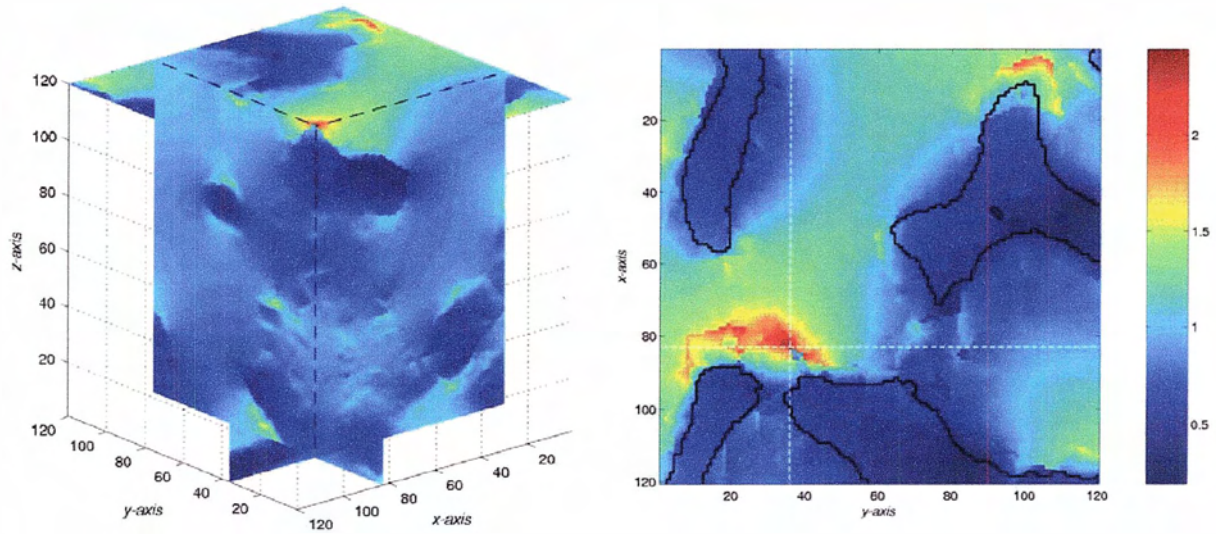

Computed by SPFD

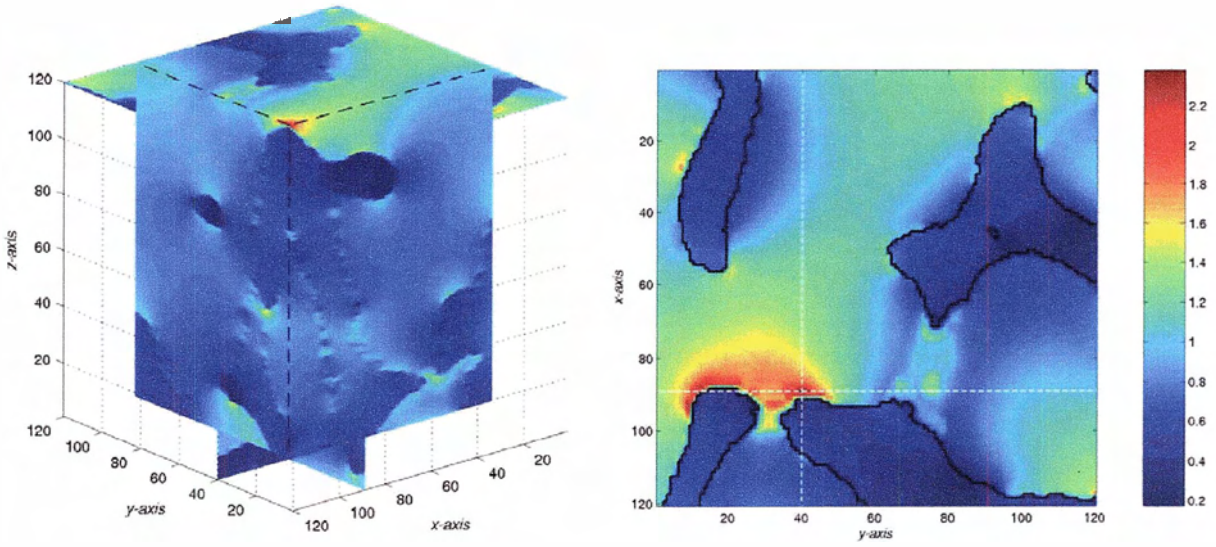

Figure 4.19: Locations of Electric Field Minima (Cancellous Model C)

The minima are indicated by the intersections of the dotted lines in each figure. On the left column are 3D plots of the *xy*, *yz* and *zx*-planes on which the minima are located. The view angles are adjusted to obtain best viewing of the features. On the right column are cross-sectional *xy*-planes. The geometry overlaid on the field distributions is represented by the black solid line. Note that the color scales are different to optimize viewing of each set of data.

Computed by FEM

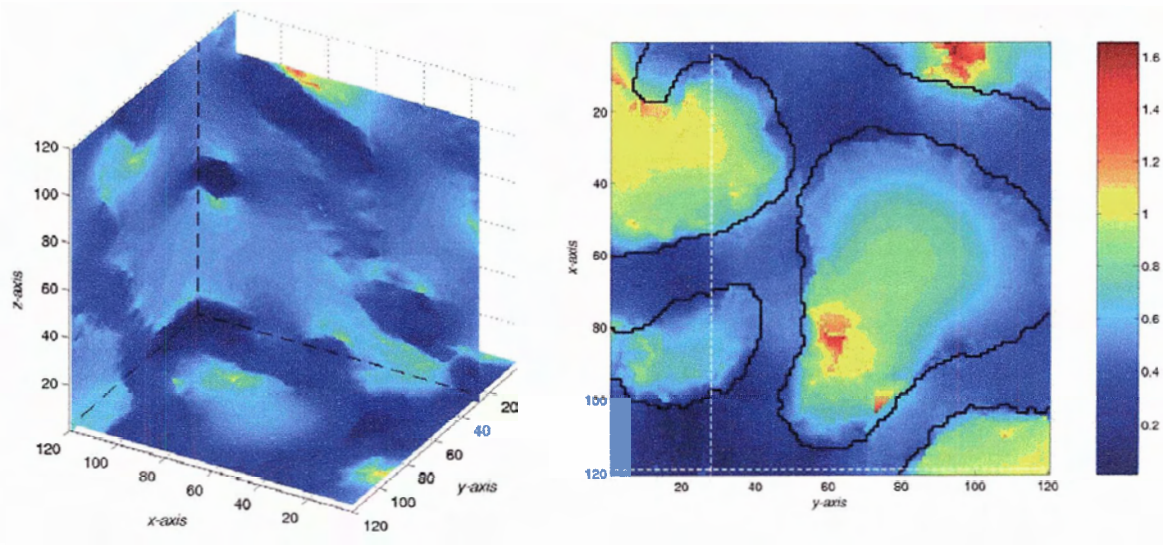

Computed by SPFD

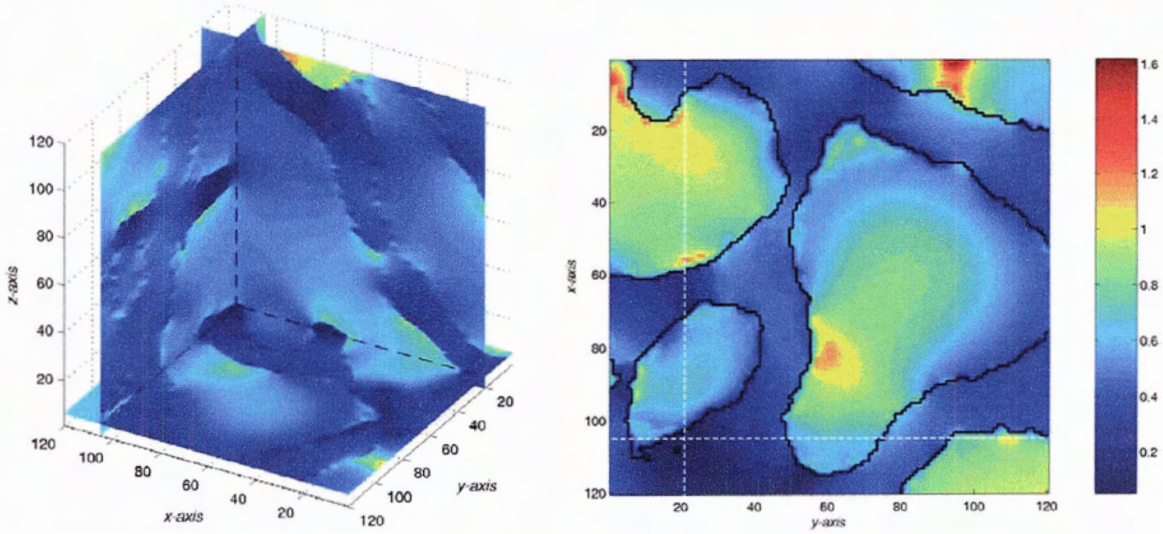

4.1.7 Electric Field Enhancement

The main focus of this research is electric field enhancement within the bone marrow sub-structures. As numerical discrepancies are inevitable in such computations, the 99.5 percentile values are used instead of the maximum values to avoid including artifacts.

With a constant $\sigma_{cancellous\_bone}$ (0.04 S/m) for all models, varying σ_{bone_marrow} results in different degrees of conductivity gradient at the interfaces between the two domains. Model A to C represent an increasing conductivity gradient, as indicated by computed standard deviations; the more distinct the conductivities, the wider the range of resultant fields; and hence the larger the relatively field enhancement comparing the $E_{99.5\%}$ values to the mean values.

However, although the σ_{bone_marrow} = 0.002 S/m used in Model C is listed on the Italian National Research Council web site on dielectric properties of human tissues, we find this value highly improbable, especially when compared to $\sigma_{cancellous\_bone}$. As discussed in the section 3.2, bone marrow is a composition of various active developing tissues including blood cells. Cancellous bone in the model represents the skeletal structure composed mainly of calcium compounds. Even though cancellous bone is also composed of living cells, it seems to lack the activity and low viscosity for a higher conductivity than bone marrow. Hence, we believe that Model A and B represent more realistic dielectric values for the bone sub-structure.

Narrowing our analysis to Model A and B, the mean electric field strengths are very close to the applied field of 1 V/m, which is regarded as the reference field strength. Then the largest enhancements averaged over the entire block are 13% and 37% respectively for Model A and B. Within the less conductive cancellous bone region, the peak enhancements can be as high as 18% and over 50%, respectively. On the other hand, the strongest enhancements in bone marrow region are 6% and 16% for the two models.

While these values do not suggest that the tissue experiences a 50% field enhancement in average, we may conclude that the active developing bone marrow cells experience a

wide range of electric field strength in their immediate surrounding. This range is wider with a steeper conductivity gradient.

4.2 Single Stroma Cell Model

Stroma cells were chosen among the various bone marrow cell types mostly due to their irregular shapes. Therefore, the evaluation of the single stroma cell results focuses on the possible influence of its geometry features to electric field distribution. This model disregards the presence of the non-conductive membrane surrounding the cell; hence there are only two materials: interior or cytoplasm of the stroma cell ($\sigma_{cytoplasm} = 0.05$ S/m) and surrounding medium ($\sigma_{medium} = 0.5$ S/m).

The single stroma cell data for the SPFD program are extracted from the FEMLAB geometry object as a 312×50×312 matrix. To facilitate comparisons, the field outputs of the FEM computation are also specified to be 312×50×312 matrices.

4.2.1 FEM Results: Electric Field Distribution

An electric field distribution color-map plotted across the middle of the single stroma cell is shown in Figure 4.20 with the geometry of the stroma cell outlined. Most of the areas of the plot indicate the same color corresponding approximately to the applied field of 1 V/m. However, the color bar indicates that the maximum and minimum of the resultant electric field were in the vicinity of -22 and 30 V/m. The negative values violate the definition of electric field magnitude which should always be positive.

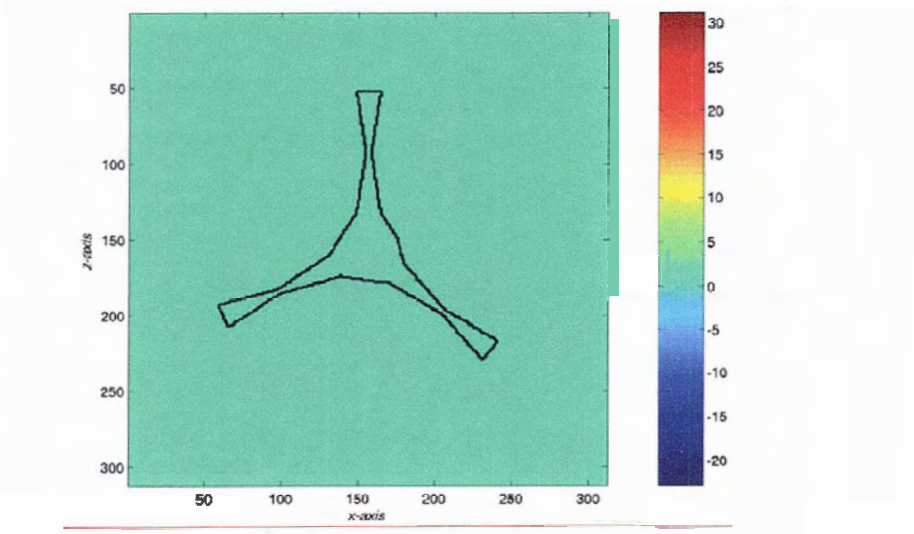

Figure 4.20: Electric Field Distribution across the Cross-section of the Single Stroma Cell Computed by the FEM

Examining the plot closer we find a few voxels of different color near the surface of the stroma cell. Zooming into the region, as in Figure 4.21, indicates a few discontinuous data points.

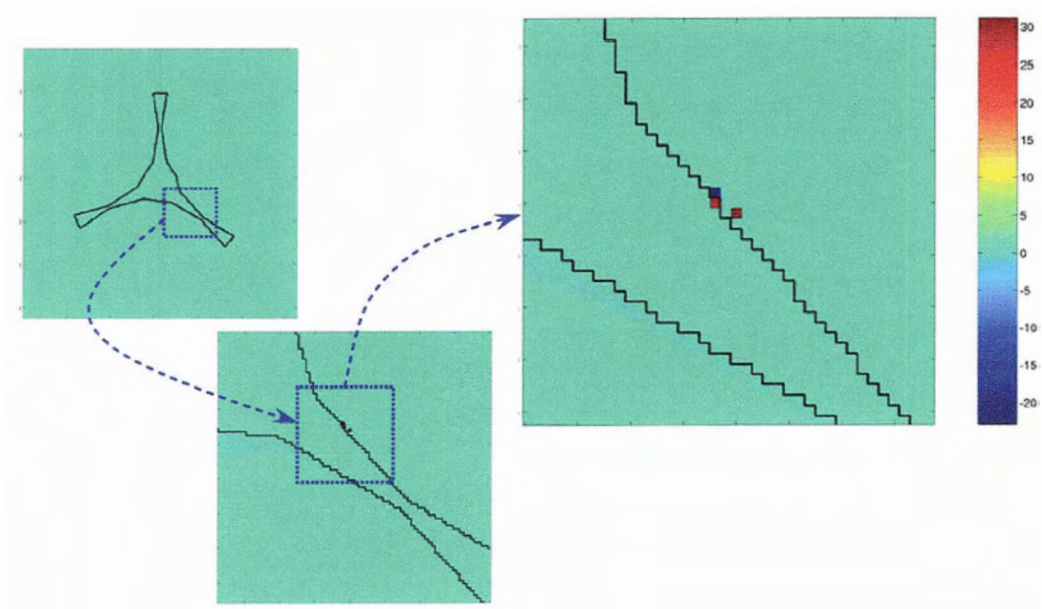

Figure 4.21: Zooming into the Locations of the Maximum and Minimum Points

Performing a statistical analysis on the 312×50×312 = 4,867,200 data points with MATLAB, it was noticed that several values were denoted 'NaN', i.e., not-a-number.

Processing after removing the five 'NaN' data points, the results of statistical analysis for the 4,867,195 points are listed in Table 4.9.

Table 4.9: Statistical Distributions of Electric Field Strength in the Single Stroma Cell Model Computed by the FEM

|E| [V/m]	FEM Results
Minimum	-22.93
Maximum	31.25
Mean	1.00
Standard deviation	3.82e-2
$E_{99.5\%}$	1.24
$E_{99\%}$	1.14
$E_{1\%}$	0.958
$E_{0.5\%}$	0.935

The mean value is equal to the applied electric field strength, while $E_{99.5\%}$ and $E_{0.5\%}$ are 1.24 and 0.94 V/m respectively. These values indicate that the maximum and minimum values of 31.2 and -22.9 V/m are probably numerical errors rather than field enhancements. Hence, with a range of 0.94 to 1.24 V/m, the FEM computation does not indicate any significant electric field enhancement when the single stroma cell model is subjected to an applied field of 1 V/m.

4.2.2 SPFD Results: Electric Field Distribution

Unlike the FEM results, no apparent artifacts are observed in the SPFD results. Figure 4.22 shows a plot of the electric field across the middle of the cell in the *xz*-plane.

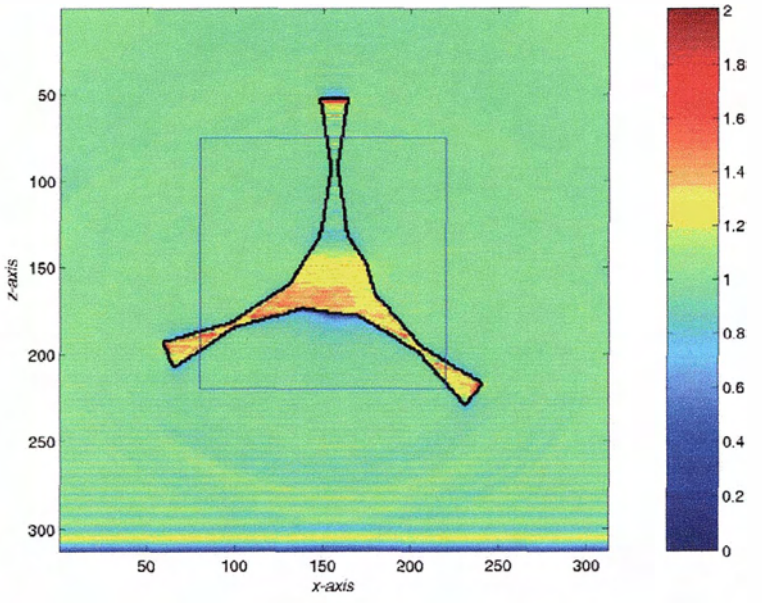

Figure 4.22: Electric Field Distribution across the Cross-section of the Single Stroma Cell Computed by the SPFD Method

The high electric field region at the truncated ends of the stroma cell arms are artifacts as predicted. As described in Figure 3.13, those regions should be trimmed off. For this particular model, the area inside the blue frame in Figure 4.22 produces Figure 4.23 after adjusting the color scale.

The range of electric field distribution is limited; slightly higher field is nonetheless observed at the middle of the stroma arms where the diameter is reduced. Little effect is shown at the arm parallel to the applied electric field, which is an expected behaviour as the tangential electric field is continuous. Regions just outside the surface of the stroma cell show lower, or even close to zero, electric field strength. This is due to the curved surfaces of the stroma cell and the fact that at the tip, the field on the opposite directions cancel each other. As illustrated by the two blue arrows in Figure 4.24, the vectors on one side of the symmetry line are mirror images of the vectors on the other side.

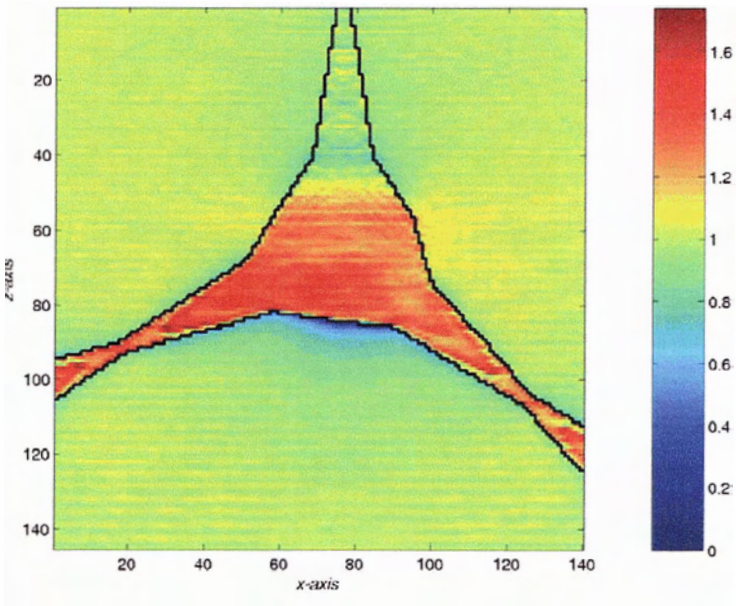

Figure 4.23: Trimmed Electric Field Distribution across the Cross-section of the Single Stroma Cell Computed by the SPFD Method

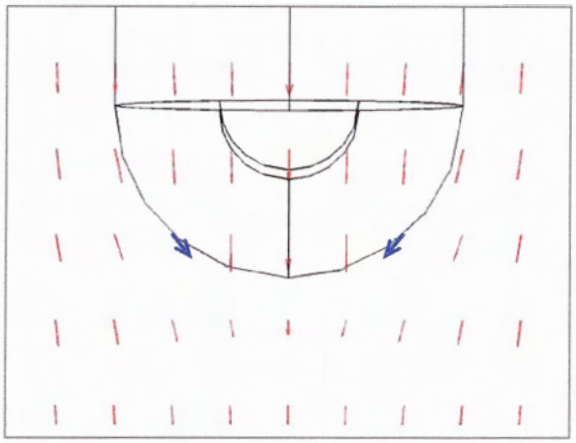

Figure 4.24: Electric Field Vectors (red arrows) at the Tip of a Curved Structure

However, some wavy pattern can be observed obviously in both Figure 4.22 and Figure 4.23 of the electric field, especially at regions closer to boundaries. These are most likely caused by the insufficient distance between the stroma cell and the boundaries, thus portion of the field is reflected and refracted at the boundaries.

The values from the statistical analysis of all the 4,867,200 data points are listed in Table 4.10.

Table 4.10: Statistical Distributions of Electric Field Strength in the Single Stroma Cell Model Computed by the SPFD Method

|E| [V/m]	SPFD Results
Minimum	0
Maximum	2.01
Mean	1.00
Standard deviation	7.15e-2
$E_{99.5\%}$	1.23
$E_{99\%}$	1.20
$E_{1\%}$	0.684
$E_{0.5\%}$	0.496

Table 4.11 gives the comparisons between the two methods using the relative difference formula as for the cancellous bone models. Since the maximum and minimum values from the FEM result are probably invalid, they are disregarded in the comparison.

Table 4.11: Comparisons of Statistical Distributions of Single Stroma Cell Model Computed by the FEM and SPFD Methods

|E| [V/m]	FEM Results	SPFD Results	RD
Mean	1.00	1.00	0.013%
Standard deviation	3.82e-2	7.15e-2	60.7%
$E_{99.5\%}$	1.24	1.23	0.30%
$E_{99\%}$	1.14	1.20	5.68%
$E_{1\%}$	0.958	0.684	33.3%
$E_{0.5\%}$	0.935	0.496	61.4%

With an almost identical mean value, and very close 99.5 percentile values, the electric field strength computed by the SPFD method covers a wider range and thus more voxels with weaker electric field strength. Referring to the explanation illustrated in Figure 4.24, the electric field vectors are more likely to cancel each other with the regular grid of the SPFD method as compared to the FEM mesh containing tetrahedrons of various sizes.

4.2.3 Validity of Model

Despite relatively good agreements for the mean and percentile values for the two methods, neither the FEM nor the SPFD result should really be relied upon. The void data points in the FEM result and the observed boundary errors in the SPFD result suggest that a finer mesh and larger domain would be necessary to properly solve this model. Unfortunately, due to limitations imposed by computer resources, such a model cannot be implemented.

4.3 Gap-Connected Stroma Cell Model

This model could only be implemented with the FEM. Instead of studying electric field enhancement directly, the transmembrane potential (TMP) across the gap junction is computed.

With all other parameters maintained constant, the conductivity of the gap junction is varied from the completely open scenario of $\sigma_{gap} = \sigma_{membrane} = 10^{-7}$ S/m to the completely closed case when $\sigma_{gap} = \sigma_{cytoplasm} = 0.05$ S/m. Over the same range of σ_{gap}, two gap junction radii: 1 and 0.5 μm are computed. For the latter, different values for membrane thickness – 10, 20 and 30 nm – are also attempted.

4.3.1 Evaluation of TMP

Since the thin layer of membrane is incorporated into the model as boundary conditions, there is no physical "layer" in the model where the TMP "measurement" can be taken. Numerous experiments with FEMLAB found that a small δ of 1e-6 μm from each side of the boundary produces reliable data to compute the TMP.

Apart from the TMP across the gap junction, the TMPs at the top and bottom plate are also computed for reference. Figure 4.25 illustrates the TMP reported and their corresponding locations. The potentials along the *z*-axis (as indicated by the red dotted line in the figure) were also compared. A detailed listing of the values indicated in

Figure 4.25, together with properties like number of elements and time required to solve the FEM problem, can be found in Appendix B.

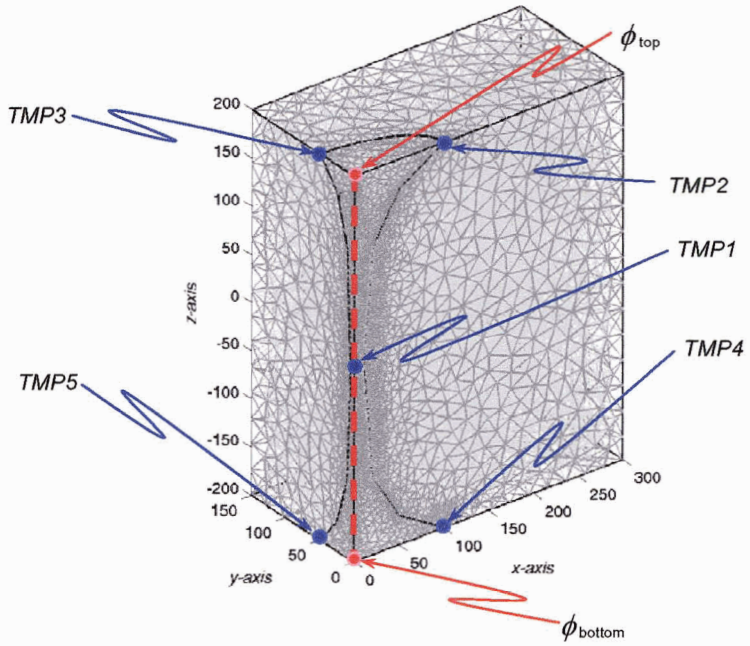

Figure 4.25: FEM mesh for the gap-connected stroma cell model and locations when different electric potential values were taken

4.3.2 TMP across Gap Junction

The TMP across the interface of two gap-connected stroma cells is summarized in Table 4.12 against varying gap conductivity for different trials with various gap radius (r_{gap}) and membrane thickness ($t_{membrane}$).

Table 4.12: TMP across Gap Junction [μV]

σ_{gap} [S/m]	1.0e-7	1.0e-6	1.0e-5	1.0e-4	1.0e-3	1.0e-2	5.0e-02
r_{gap} = 1 μm; $t_{membrane}$ = 10 nm	224.81	222.54	212.92	151.08	35.48	4.60	1.12
r_{gap} = 0.5 μm; $t_{membrane}$ = 10 nm	218.15	221.36	219.15	189.18	81.77	17.03	7.44
r_{gap} = 0.5 μm; $t_{membrane}$ = 20 nm	219.32	228.42	230.19	210.94	122.27	23.49	10.22
r_{gap} = 0.5 μm; $t_{membrane}$ = 30 nm	230.91	219.18	242.77	243.51	143.70	28.46	11.24

As predicted, when σ_{gap} is relatively small, the membrane acts as insulator; and thus the TMP is high. However, as σ_{gap} increases, more current enters into the stroma cell in the lower part of the model, thus the difference of electric potential at the interface drops. Figure 4.26 illustrates the flow of current at different σ_{gap}. When $\sigma_{gap} = \sigma_{membrane}$, more current tends to flow towards the side of the stroma cell which has a lower resistance due to a greater surface area. When $\sigma_{gap} = \sigma_{cytoplasm}$, more current passes through the gap junction; and hence the current tends to flow towards the centre.

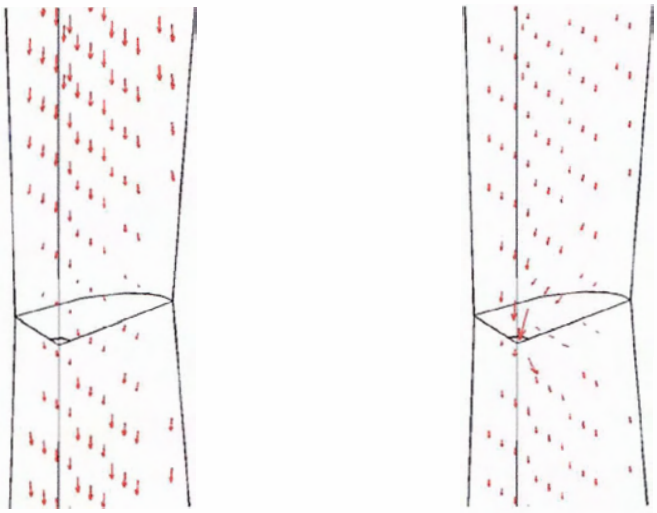

(a) gap closed
$\sigma_{gap} = \sigma_{membrane} = 1.0\times10^{-7}$ S/m

(b) gap open
$\sigma_{gap} = \sigma_{cytoplasm} = 0.05$ S/m

Figure 4.26: Diagrams of Current Flow across the Gap Junction: (a) gap closed; (b) gap open

Figure 4.27 shows the TMPs given in Table 4.12 plotted in the log scale of σ_{gap}. It should be noticed that although all four curves demonstrate a similar tendency as σ_{gap} increases, those with thinner membranes seem to be more consistent. Recalling that one criterion for the thin film approximation is that the thickness of the interface must be small, it is not surprising to notice more significant numerical fluctuation as $t_{membrane}$ increases.

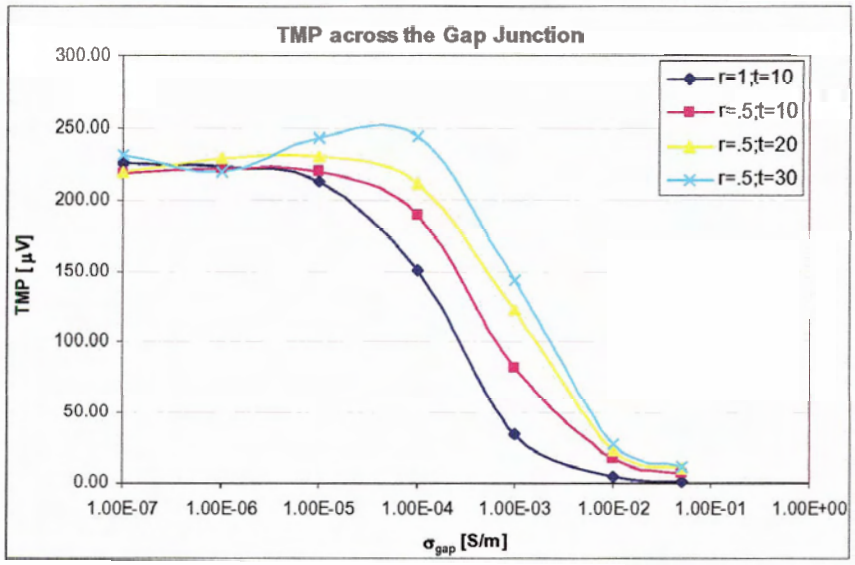

Figure 4.27: TMP across Gap Junction for Various Gap Conductivities

Although TMP is much smaller when $\sigma_{gap} = \sigma_{cytoplasm}$, it does not go to zero. In fact, a plot of the electric potential change along the entire z-axis as shown in Figure 4.28 indicates that the potential changes much more rapidly as it approaches the interface of the two cells (which is half-way between the entire length of the domain in z-direction). This phenomenon is due to the fact that the gap junction does not occupy the entire interface between the two cells, as illustrated in Figure 4.26. The region right next to the gap junction still possesses low conductivity of $\sigma_{membrane} = 10^{-7}$ S/m.

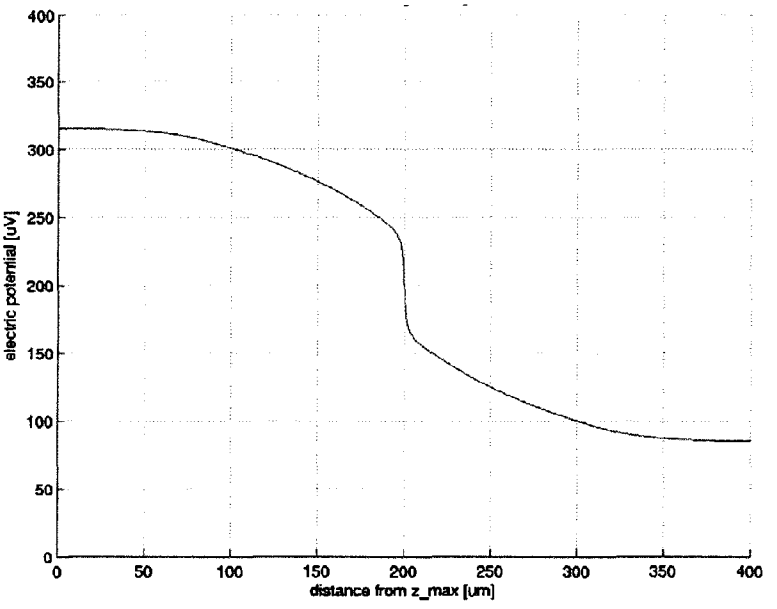

Figure 4.28: Electric Potential Change along *z*-axis when $\sigma_{gap} = \sigma_{cytoplasm}$

Also observed from Figure 4.28 is the fact that the potential does not drop linearly with distance. Because of the shape of the stroma cell model, the radius of the stroma arm changes more rapidly towards the top and bottom boundaries. This is evidence that the funnel shape of the stroma cell does have an impact on the electric potential distribution too.

More plots and discussion of other potential values as indicated in Figure 4.25 can be found in Appendix B.

5. Discussion

Recalling that this thesis is motivated by the hypothesis linking childhood leukemia to strong electric fields in bone marrow, this chapter relates the obtained results to the known biological conditions and mechanisms in an attempt to further examine this hypothesis. However, first of all, due to the lack of analytical data, and the employment of various numerical assumptions and simplifications, the validity of the results needs to be confirmed.

5.1 Verification of Numerical Results

Unlike some other numerical computation research reviewed in section 2, there is no known published literature on comparable models that the results can be directly compared with. Thus these results must be verified based on other means.

5.1.1 Cancellous Bone Model

Voltage excitation is employed for our computations; therefore, no current source is used. The cancellous bone model would have been a straight forward computation of Laplace's equation of the form $-\nabla\cdot(\sigma\nabla\phi)=0$ if each element or voxel of the grid contained single homogeneous material only. For the SPFD computation, this is indeed the case since each voxel either represents cancellous bone or bone marrow; thus σ is constant for a single element, and potentials are defined at the vertices.

The FEM meshes generated for defined geometric structures also ensure that each element contains only one material. However, due to the complexity of the cancellous bone model, the FEM mesh is created *without* the geometry as discussed in section 3.2.3 and illustrated in Figure 3.9. As a result, certain FEM elements inevitably overlap different material regions. To assign proper conductivity values to these elements, interpolation is incorporated to the conductivity function written for the cancellous bone FEM model.

As observed in some of the graphical plots of the resultant fields (Figure 4.16 to Figure 4.19), the material boundaries are indeed not as clearly displayed, especially when compared to the SPFD results. Nonetheless, the overall statistical comparison between the FEM and SPFD results shows reasonable agreement, and most of the extrema are found to locate in the same regions of the model. Therefore, the alternative approach in the FEM computation is proven to be a viable implementation, which can be employed to other irregular and complex structures such as cancellous bone.

5.1.2 Gap-Connected Stroma Cell Model

Many studies on TMP of gap junction connected cells focus on the single cell or cell assemblies. However, the gap-connected stroma cell model consists of partial elongations of a highly irregularly-shaped cell type. Also, computations for cell clusters usually solve for the TMP at the end of cell assemblies, as shown in Figure 2.4. This model, instead, takes TMP across the gap junction directly. However, while the values are dissimilar, the response of TMP to changing gap conductivity should behave in a comparable manner.

Consider two elongated cells connected by a gap junction as illustrated in Figure 5.1. If the applied electric field is constant, then electric potentials ϕ_a and ϕ_b taken outside the cells in the surrounding medium should stay more or less constant. The potential within the membrane-covered cells does not vary much. Therefore the magnitude of TMP across the gap junction depends on the TMP at the membrane ($TMP_{membrane}$). If the latter decreases, the potential across the gap junction will increase to maintain the potential gradient outside the cells.

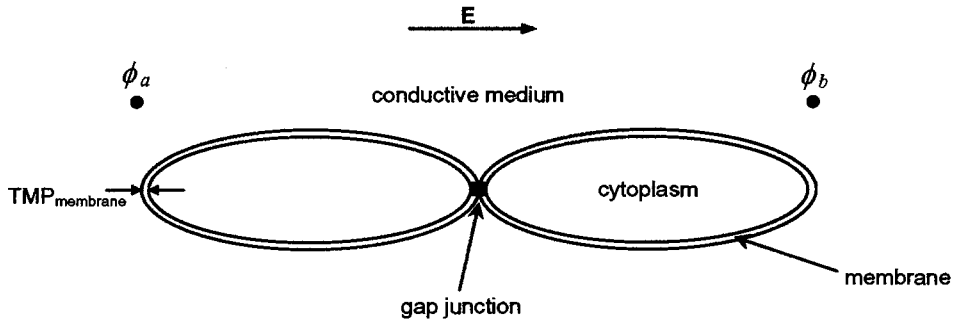

Figure 5.1: Model of Two Gap-Connected Elongated Cells

Previous studies have shown that with small σ_{gap} (10^{-7} to 10^{-5} S/m), close to that of $\sigma_{membrane} = 10^{-7}$ S/m, $TMP_{membrane}$ is about that of a single cell [5]. Between $\sigma_{gap} = 10^{-5}$ S/m to a conductivity close to that of the cytoplasm at about 0.05 S/m, $TMP_{membrane}$ increases logarithmically according to the expression:

$$TMP_{membrane} = TMP_{single} + [(TMP_{elongated} - TMP_{single}) \times (5 - \log(\sigma_{gap}))] / 3.7 \qquad (5.1)$$

where TMP_{single} and $TMP_{elongated}$ denote TMP of a single cell and an equivalent cell (as proposed by Fear and Stuchly [5]). At σ_{gap} close to 0.05 S/m, $TMP_{membrane}$ can be approximated by that of a cell chain connected by cytoplasm-filled gaps. In summary, with a log scale, $TMP_{membrane}$ shows a flat line at low σ_{gap}, then a linear increase to about 0.05 S/m where it levels.

If TMP across the gap (TMP_{gap}) has an opposite behaviour, then at low σ_{gap}, TMP_{gap} is high but changes little; between roughly 10^{-5} S/m to 0.05 S/m, a near linear drop should be observed until it flattens at low TMP_{gap} when σ_{gap} is high. The resultant TMP_{gap} as shown in Figure 4.27 exhibits a similar pattern. Therefore, it can be concluded that the gap-connected stroma cell model, with its thin film approximation, successfully represented the TMP change across the interface of two stroma cells.

5.2 Biophysical Implications

The hypothesis that EMF at power-line frequencies does indeed have a plausible correlation to childhood leukemia cannot be supported by this thesis unless sufficiently strong electric fields are found to be induced within the bone marrow regions.

5.2.1 Cancellous Bone Model

Cancellous bone serves almost as housing for bone marrow. On one hand, its relatively lower conductivity provides a shielding to the bone marrow cells from external EMF. On the other hand, its irregular geometry can create regions of higher electric field strength.

Assuming that Model A with relatively close conductivities between the cancellous bone ($\sigma_{cancellous}$ = 0.04 S/m) and bone marrow (σ_{marrow} = 0.05 S/m) is a realistic representation for adult human properties, then Model B with higher bone marrow conductivity (σ_{marrow} = 0.07 S/m) may represent that of children. Comparing the results of the two models, it may be proposed that children are more vulnerable to influences induced by low frequency EMFs.

However, although the electric field within the cancellous bone model varies over a wide range, the overall averages for both models are close to the applied field. Thus most of the bone marrow cells experience an electric field not much higher than the tissue average. Closer examination of the maxima locations suggests that if $\sigma_{marrow} > \sigma_{cancellous}$, then the strongest fields occurs within the bone region instead of the bone marrow region, as shown in Figure 4.16. Therefore, likely not enough disturbances can be caused by the EMF in the surrounding environment to induce biological effects to the bone marrow cells.

5.2.2 Stroma Cell Model

Biological cells are actively developing and communicating all the time. Gap junctions are believed to be channels for such inter-cellular communication as well as ionic exchange. Thus the junctions constantly vary between the open and closed states. The computed TMP for the stroma cell model shows that the gap junction experiences a range from several to over 200 μV potential difference between the two states. However, this kind of magnitudes is only possible if the cells are subjected to an immediate environment of 1 V/m electric field.

Suppose that 1 mV is a reasonable benchmark for significant TMP change, then an electric field of about 5 V/m would be needed in the bone marrow region. The maximum enhancement of the electric field in the bone marrow regions is 16% as computed in the cancellous bone Model B (Table 4.5). An applied field of over 4 V/m would have to be present in the tissue. The ICNIRP guidelines suggest a 0.5 mA contact current limit for power-line frequencies [49]. Dawson *el al.* reported that the average electric field for such contact current would be about 2.53 V/m in the lower arm of children (the region where resultant electric field was strongest) and 0.83 V/m for adults [9]. Hence, it is unlikely for a stroma cell to experience a strong enough electric field to cause significant TMP change. Furthermore, the typical resting TMP is about 60 to 90 mV, whereas a change in exceed of 20 mV is usually required for any biological activation [50]. Therefore a contact current much stronger than that laid out by the guidelines would be needed to stimulate biological responses at cell membranes.

5.2.3 Limitations of the Models

The human body is a highly complex biological system. Despite our attempts in creating realistic models, they suffer from several limitations imposed by computer resources and power of the numerical solvers. Many simplifications are necessary to implement the models with reasonable complexity to be handled by the numerical programs. Other simplifications are made due to the existence of details or mechanisms yet to be fully understood at the sub-cellular level in the biological realm.

The following assumptions are known to be over-simplifications, even though they should not affect the validity of the results:

a) *Homogeneous tissues*

The cancellous bone model assumes constant conductivity for each tissue group, but in reality, bone marrow is known to be an assortment of many different cell types, neither is cancellous bone made up of a single cell type. In fact, dielectric properties cannot really be measured for an individual cell type; published data are mostly bulk properties representing the average values of the cell mixtures too.

b) *Other cells or components present in the system are ignored*

One obvious omission is blood vessels or capillaries which should weaver around the bone matrix, and to which some stroma cells may be attached. Also, considering the roles of stroma cells in lymphocyte development, there may be developing or differentiating cells adhere to their surfaces.

c) *Actual stroma cells should probably have more complex shapes*

Stroma cells do not show up well in blood smears, and we do not have any microscopic photos of them. From the pictorial views sketched by microbiologists, a typical stroma cell should have more convoluted geometry than that depicted in our models. For example, the cells are not rigid, thus the arms, where two stroma cells connect, are not likely to be straight. Nevertheless, the model maintains the key features of non-conducting membrane, funneling shape, as well as the gap junction connection.

d) *Biological systems are dynamic, not static*

Both bone and bone marrow are actively developing organs; the static models are only snapshots of the ever-changing structures. Some of the field enhancements may only be transient.

5.3 Significance of Tissue Conductivity Assignment

It is evident from the computations that under electrostatic assumption, the conductivity values assigned to different tissues are crucial to the results. Although we propose that Model C of the cancellous bone computation does not represent realistic human properties, it is a good demonstration on how sensitive the results are to material properties.

Realistic dielectric values are obtained experimentally. However, most published figures are bulk properties at tissue levels. With their microscopic sizes and dynamic nature, few data are available at sub-cellular level. More experiments are required to enhance the database of dielectric properties for biological tissues in order to form the basis for reliable numerical computations.

6. Conclusions

This thesis is not meant to be an extensive study on the hypothetic correlation between EMF and childhood leukemia. Instead, it intends to supplement existing knowledge of EMF interactions with human body at power-line frequencies, from a sub-cellular perspective using numerical computations.

This chapter will first summarize the work accomplished in this thesis, and then propose directions for future research.

6.1 Bone Marrow Sub-structures & Electric Field Enhancements

One way to study leukemia is to get down to the cause of the problem – bone marrow cells. The computations in this thesis attempt to investigate the local EMF at the bone structures where bone marrow cells reside. Previous tissue-specific computations of the whole human body models considered *everything* located between the compact bones in the long bones as *bone marrow*. The cancellous bone model attempts to separate the bone marrow cells from the cancellous bone matrix. The stroma cell model tries to zoom in even closer to the potential change experienced by one of the cells from the bone marrow family.

Unfortunately, or maybe fortunately, our computations conclude that although it is inarguable that electromagnetic fields redistribute within bone marrow sub-structures according to geometries and presence of gap junctions, none of the changes observed would be significant enough to cause detrimental biological effects.

6.2 Numerical Methods

Powerful computers and advancements in numerical techniques promise ever-increasing accuracy and efficiency in solving more complicated problems. From primitive shapes to MRI data, numerical methods have certainly gone a long way. Unfortunately, these techniques still have their own shortcomings. For example, although finite difference methods can solve very large problems if they are properly discretized into voxels, even

graded grids are not the best representation of most biological objects which usually have smooth and curved surfaces. The FEM is typically recognized as the method of choice for irregular geometries. Despite the development of different mesh generation algorithms, dividing the computation domain into fine meshes that conform well to the geometry can be computationally expensive.

This thesis explores two alternative ways to expand the capability of the FEM:

- Meshing a domain without the geometric object whose information enters into the computation as interpolated material properties
- Replacing thin membrane with boundary conditions in the neighbouring material interfaces

These two approaches are proven to produce good results. They open the possibility of computing problems which would otherwise be too computationally expensive, or numerically unstable.

6.3 Future Research

This thesis provides only a glimpse to the subject of solving bioelectromagnetic problems with numerical techniques. It is a promising step forward in analyzing more realistic biological structures, especially at cellular or sub-cellular level. Apart from extending the work to other models or applications, due to time constraints and scope of the thesis, the established methods and models are yet to be fully explored.

6.3.1 Cancellous Bone Model

Only one set of CT data is employed in this thesis. If multiple sets of cancellous bone data can be acquired, results can be compared and analyzed to identify geometric features which induce greater influences in the electric field distributions.

With the existing set of data, more combinations of conductivities can still be assigned to further investigate the sensitivity of the responses with respect to the parameters, as well as with respect to the numerical methods.

6.3.2 Stroma Cell Models

The single stroma cell model can be fine-tuned for more reliable results. Taking advantage of symmetries, the model can be reduced, thus finer mesh and largest distances to the boundaries can be implemented.

Instead of a separate model for gap junctions, the thin film approximation can be introduced directly to the single stroma cell at the various locations where it connects to adjoining cells.

6.3.3 Combining Both Models

Since stroma cells are part of the bone marrow network, a combination of the two models would provide a bigger picture. However, introducing stroma cells into the cancellous bone model may result in problems beyond the capability of existing numerical solvers and computer resources. Alternatively, the results obtained from the cancellous bone model can be utilized as initial or boundary conditions for the stroma cell model, thus implementing the combined model as a two-step procedure.

Bibliography

[1] Nancy Wertheimer and Ed Leeper, "Electrical Wiring Configurations and Childhood Cancer", *American Journal of Epidemiology*, vol. 109 (3), pp. 273-284, 1979

[2] L.E. Anderson, "Biological Effects of Extremely Low-Frequency and 60 Hz Fields", *Biological Effects and Medical Applications of Electromagnetic Energy*, pp. 196-235, Prentice Hall, 1990

[3] Kenneth R. Foster and Arthur E. Sowers, "Dielectrophoretic Forces and Potentials Induced on Pairs of Cells in an Electric Field", *Biophysical Journal*, vol. 69, pp. 777-784, September 1995

[4] J. Bernhardt and H. Pauly, "On the Generation of Potential Differences across the Membranes of Ellipsoidal Cells in an Alternating Electrical Field", *Biophysik*, vol. 10, pp. 89-98, 1973

[5] Elise C. Fear and Maria A. Stuchly, "Biological Cells with Gap Junctions in Low-Frequency Electric Fields", *IEEE Transactions on Biomedical Engineering*, vol. 45, pp. 856-866, July 1998

[6] Maria A. Stuchly and Trevor W. Dawson, "Interaction of Low-Frequency Electric and Magnetic Fields with the Human Body", *Proceeding of the IEEE*, vol. 88(5), pp. 643-664, May 2000

[7] National Cancer Institute, Cancer.gov Dictionary, Internet resource, <http://www.cancer.gov/dictionary/>, last visited February 4, 2004

[8] R. Kavet, L. E. Zaffanella, J. P. Daigle, and K. L. Ebi, "The Possible Role of Contact Current in Cancer Risk Associated With Residential Magnetic Fields", *Bioelectromagnetics*, vol. 21(7), pp. 538-553, October 2000

[9] Trevor W. Dawson, Krys Caputa, Maria A. Stuchly and R. Kavet, "Electric fields in the human body resulting from 60-Hz contact currents", *IEEE Transactions on Biomedical Engineering*, vol. 48(9), pp. 1020-1026, Sep 2001

[10] Stephan P. Albert Bren, "60Hz EMF Health Effects - A Scientific Uncertainty", *IEEE Engineering in Medicine and Biology Magazine*, vol. 14(4), pp. 370-374, July/Aug 1995

[11] Poole, C.; Ozonoff, D., "Magnetic Fields and Childhood Cancers", *IEEE Engineering in Medicine and Biology Magazine*, vol. 15(4), pp. 41-49, July/Aug 1996

[12] Ashley, J.R.; Beatie, R.E.; Heneage, J.F., "Evaluation of power line measurements of the link with cancer", *Proceedings of the IEEE Southeastcon '96 "Bringing Together Education, Science and Technology"*, pp. 41-50, April 1996

[13] Kenneth R. Foster, Linda S. Erdreich, John E. Moulder, "Weak Electromagnetic Fields and Cancer in the Context of Risk Assessment", *Proceedings of the IEEE*, vol. 85(5), pp. 733-746, May 1997

[14] Edward P. Richards, "Litigating Fear: Electrical and Magnetic Fields (EMF) and the Law", *IEEE Engineering in Medicine and Biology Magazine*, vol. 16(5), pp. 176-178, Sept/Oct 1997

[15] National Institute of Environmental Health Sciences (NIEHS), "NIEHS Report on Health Effects from Exposure to Power-Line Frequency Electric and Magnetic Fields", May 1999. Internet resource, <http://www.niehs.nih.gov/emfrapid/home.htm>

[16] Hiraku Takebe, Takeshi Shiga, Masamichi Kato, Eisuke Masada, *Biological and Health Effects from Exposure to Power-Line Frequency Electromagnetic Fields*, IOS Press, 2001

[17] Donald E. Livesay and Kun-Mu Chen, "Electromagnetic Fields Induced Inside Arbitrarily Shaped Biological Bodies", *IEEE Transactions on Microwave Theory and Techniques*, vol. 22(12), pp. 1273-1280, Dec 1974

[18] Kun-Mu Chen and Bhag S. Guru, "Internal EM Field and Absorbed Power Density in Human Torsos Induced by 1-500 MHz EM Waves", *IEEE Transactions on Microwave Theory and Techniques*, vol. 25(9), pp. 746-756, Sep 1977

[19] P J Dimbylow, "Induced Current Densities from Low-Frequency Magnetic Fields in a 2 mm Resolution Anatomically Realistic Model of the Body", *Physics in Medicine and Biology*, vol. 43, pp. 221-230, 1998

[20] O.P. Gandhi and J.-Y. Chen, "Numerical Dosimetry at Power-Line Frequencies using Anatomically Based Models", *Bioelectromagnetics*, supplement 1, pp. 43-60, Sep 1992

[21] C Gabriel, R.W. Lau and S Gabriel, "The Dielectric Properties of Biological Tissues: Measurements in the Frequency Range 10 Hz to 20 GHz", *Physics in Medicine and Biology*, vol. 41(11), pp. 2251-2269, Nov 1996

[22] M.A. Stuchly and O.P. Gandhi, "Inter-laboratory Comparison of Numerical Dosimetry for Human Exposure to 60 Hz Electric and Magnetic Fields", *Bioelectromagnetics*, vol. 21(3), pp. 167-174, April 2000

[23] Kenneth R. Foster and Herman P. Schwan, "Dielectric Properties of Tissues", *Handbook of Biological Effects of Electromagnetic Fields*, chapter 1, 2nd ed., CRC Press, 1996

[24] J. Bernhardt and H. Pauly, "On the Generation of Potential Differences across the Membranes of Ellipsoidal Cells in an Alternating Electrical Field", *Biophysik*, vol. 10, pp. 89-98, 1973

[25] E.C. Fear and M.A. Stuchly, "Modeling Assemblies of Biological Cells Exposed to Electric Fields", *IEEE Transactions on Biomedical Engineering*, vol. 45, pp. 1259-1271, October 1998

[26] Robert Susil, Dejan Šemrov and Damijan Miklavčič, "Electric Field-Induced Transmembrance Potential Depends on Cell Density and Organization", *Electro- and Magnetobiology*, vol. 17(3), pp. 391-399, 1998

[27] J.W. Holder, E. Elmore and J.C. Barrett, "Gap Junction Function and Cancer", *Cancer Research*, vol. 53, pp. 3475-3485, 1993

[28] M. Cooper, "Gap Junctions Increase the Sensitivity of Tissue Cells to Exogenous Electric Fields", *Journal of Theoretical Biology*, vol. 111, pp. 123-130, 1984

[29] Abhishek Awadhiya, Pedro Barba and Leo Kempel, "Finite-element method programming made easy???", *IEEE Antennas and Propagation Magazine*, vol. 45(4), pp. 73-79, August 2003

[30] COMSOL AB, "COMSOL: FEMLAB – Multiphysics Modeling", Internet resource, <http://www.femlab.com>, last visited March 11, 2004

[31] COMSOL AB, *FEMLAB® Reference Manual*, version 2.2, 2001

[32] Trevor W. Dawson, Jan De Moerloose and Maria A. Stuchly, "Comparison of Magnetically Induced ELF Fields in Humans Computed by FDTD and Scalar Potential FD Codes", *Applied Computational Electromagnetics Society Journal*, vol. 11, pp. 63-71, 1996

[33] Trevor W. Dawson and Maria A. Stuchly, "Analytic Validation of a Three-Dimensional Scalar-Potential Finite-Difference Code for Low-Frequency Magnetic Induction", *Applied Computational Electromagnetics Society Journal*, vol. 11, pp. 72-81, 1996

[34] Trevor W. Dawson, Jan De Moerloose and Maria A. Stuchly, "Hybrid Finite-Difference Method for High-Resolution Modelling of Low-Frequency Electric Induction in Humans", *Journal of Computational Physics*, vol. 136, pp. 640-653, 1997

[35] T.W. Dawson, M. Potter and M.A. Stuchly, "Evaluation of Modeling Accuracy of Power Frequency Field Interactions with the Human Body", *Applied Computational Electromagnetics Society Journal*, vol. 16(2), 2001

[36] University of Victoria, "Minerva High Performance Computer Facility: Frequently Asked Questions", Internet resource, <http://minervaweb.uvic.ca/uvdoc/faq.html>

[37] U.S. National Cancer Institute, "Skeletal System / Structure of Bone Tissue", SEER's Training Web Site, Internet resource, <http://training.seer.cancer.gov/module_anatomy/unit3_2_bone_tissue.html>

[38] European Research In Space And Terrestrial Osteoporosis (ERISTO), The French Institute for Space Medicine and Physiology (MEDES), "Bone Physiology". Internet resource, <http://www.medes.fr/Eristo/Osteoporosis/BonePhysiology.html>

[39] Boston University, "Bone Marrow and Hemopoiesis", *Histology Learning System*. Internet resource, <http://www.bu.edu/histology/p/02005loa.htm>

[40] Loyola University Chcago Stritch School of Medicine, "Bone Marrow and Hemopoiesis", Loyola Univerity Medical Education Network (LUMEN), January 2001, Internet resource, <http://www.meddean.luc.edu/lumen/MedEd/Histo/HistoImages/hl5-02.jpg>

[41] Camelia Gabriel and Sami Gabriel, "Compilation of the Dielectric Properties of Body Tissues at RF and Microwave Frequencies", June 1996, Internet resource, <http://www.emfdosimetry.org/dielectric/Report/Report.html>

[42] James A. Hightower, "The Basics of Bone Marrow", 1999. Internet resource <http://www.med.sc.edu/hightower/dbmBSBi/index.htm>

[43] Italian National Research Council, "Dielectric Properties of Human Tissues", Internet resource, <http://niremf.iroe.fi.cnr.it/tissprop/>

[44] Dorshkind K., "Regulation of Hemopoiesis by Bone Marrow Stromal Cells and Their Products", *Annual Review of Immunology*, vol. 8, pp. 111-137, April 1990

[45] Yonosuke Watanabe, "Fine Structure of Bone Marrow Stroma", *ACTA Haematologica Japonica*, vol. 48, pp. 1688-1700, 1985

[46] Charles A. Janeway, Jr. and Paul Travers, "The Development of B Lymphocytes", *Immunobiology: The Immune System in Health and Disease*, Current Biology Ltd./Garland Publishing Inc., chapter 5, 1994

[47] Karen P. Steel, "One Connexin, Two Diseases", *Nature Genetics*, vol. 20, pp. 319-320, 1998

[48] COMSOL, "Thin Film Approximation", FEMLAB Knowledge Base #902, March 2004. Internet resource, <http://www.comsol.com/support/knowledgebase/902.php>

[49] International Commission on Non-Ionizing Radiation Protection (ICNIRP), "Guidelines for limiting exposure to time-varying electric, magnetic and electromagnetic fields (up to 300 GHz)", *Health Phys.*, vol. 74, pp. 494-522, 1998

[50] Jaakko Malmivuo and Robert Plonsey, "Anatomical and Physiological Basis of Bioelectromagnetism", *Bioelectromagnetism*, Oxford University Press, section I, 1995

Appendix A: MATLAB Conductivity Function for the Cancellous Bone Model

```
function sigma=cancellous_sigmas(x,y,z)
% cancellous_sigmas returns the conductivity at any given point
% of the 180x180x180 cancellous bone model
%   sigma = cancellous_sigmas(x,y,z)
%   (x,y,z) is the coordinates of interest
%   sigma is the returned conductivity
% The original sample has two tissue code:
%   1 => marrow and 127 => bone,
% with corresponding conductivity
%
% Reference: flafun(x,y) provided by FEMLAB
% Created by Roanna on 2003 Nov 27

sigma_marrow = 5e-02;
sigma_cancellous = 4e-02;

% Cancellous bone model has 180 voxels per side
nn = 180;

% Load the sample
S = myLoadGeom('cancellous.dat',nn,nn,nn);

% We also know that each side of the voxel is 14 microns
dd = 14e-6;

% In order to account for the boundaries we add more buffer
S0 = ones(nn+2,nn+2,nn+2);
S0(2:nn+1,2:nn+1,2:nn+1) = S;
clear S;

% Assign conductivity
sigma1 = sigma_marrow;
sigma2 = sigma_cancellous;
S = sigma1 + (sigma2 - sigma1) * (S0 >= 64);
clear S0;

% Create sample coordinates, shifting by half a cell
% such that the value represents "mid-point" value
[xx,yy,zz] = meshgrid((0:dd:(nn+1)*dd)-(dd/2),...
                      (0:dd:(nn+1)*dd)-(dd/2),...
                      (0:dd:(nn+1)*dd)-(dd/2));

% Interpolate from rectangular grid to any arbitrary grid
sigma = interp3(xx,yy,zz,S,x,y,z);
```

Conductivities for Model A where $\sigma_{cancellous}$ = 0.04 S/m, σ_{marrow} = 0.05 S/m

cancellous.dat is the binary file containing CT data

Appendix B: More Results from the Gap-Connected Stroma Cell Model

Table B.1: Complete Listing of the Results for the Gap-Connected Stroma Cell Model

Conductivity [S/m]	σ_{medium}	0.5							0.5						
	$\sigma_{cytoplasm}$	0.05							0.05						
	$\sigma_{membrane}$	1.0e-7							1.0e-7						
	σ_{gap}	1.0e-7	1.0e-6	1.0e-5	1.0e-4	1.0e-3	1.0e-2	5.0e-2	1.0e-7	1.0e-6	1.0e-5	1.0e-4	1.0e-3	1.0e-2	5.0e-2
Geometry [μm]	$t_{membrane}$	0.01							0.01						
	r_{gap}	1							0.5						
TMP1 [μV]	ϕ_{inside}	313.20	311.34	305.80	271.70	216.22	201.53	201.12	304.67	309.02	309.71	291.11	239.22	207.31	203.42
	ϕ_{inside}	88.39	88.80	92.88	120.62	180.73	196.93	200.00	86.53	87.66	90.55	101.93	157.45	190.28	195.98
	TMP	224.81	222.54	212.92	151.08	35.48	4.60	1.12	218.15	221.36	219.15	189.18	81.77	17.03	7.44
TMP2 [μV]	ϕ_{inside}	400.00	400.00	400.00	400.00	400.00	400.00	400.00	400.00	400.00	400.00	400.00	400.00	400.00	400.00
	ϕ_{inside}	337.26	337.66	337.46	327.52	320.39	317.29	317.70	331.53	334.73	338.15	331.19	327.96	323.12	323.05
	TMP	62.74	62.34	62.54	72.48	79.61	82.72	82.30	68.47	65.27	61.85	68.81	72.04	76.88	76.95
TMP3 [μV]	ϕ_{inside}	400.00	400.00	400.00	400.00	400.00	400.00	400.00	400.00	400.00	400.00	400.00	400.00	400.00	400.00
	ϕ_{inside}	336.28	336.66	336.43	326.33	319.01	315.82	316.23	330.45	333.70	337.16	330.08	326.75	321.80	321.72
	TMP	63.72	63.34	63.57	73.67	80.99	84.18	83.77	69.55	66.30	62.84	69.92	73.25	78.20	78.28
TMP4 [μV]	ϕ_{inside}	0.00	0.00	0.00	0.00	0.00	0.00	0.00	0.00	0.00	0.00	0.00	0.00	0.00	0.00
	ϕ_{inside}	63.47	63.60	64.08	67.02	77.22	81.61	83.08	62.28	62.96	64.18	63.94	69.99	75.89	76.98
	TMP	63.47	63.60	64.08	67.02	77.22	81.61	83.08	62.28	62.96	64.18	63.94	69.99	75.89	76.98
TMP5 [μV]	ϕ_{inside}	0.00	0.00	0.00	0.00	0.00	0.00	0.00	0.00	0.00	0.00	0.00	0.00	0.00	0.00
	ϕ_{inside}	64.47	64.61	65.09	68.12	78.56	83.05	84.55	63.26	63.95	65.18	64.96	71.16	77.19	78.32
	TMP	64.47	64.61	65.09	68.12	78.56	83.05	84.55	63.26	63.95	65.18	64.96	71.16	77.19	78.32
$\phi1$ [μV]	$\phi1$	335.80	336.19	335.96	325.75	318.35	315.13	315.54	329.91	333.20	336.70	329.54	326.18	321.17	321.09
$\phi2$ [μV]	$\phi2$	64.95	65.09	65.58	68.65	79.20	83.74	85.25	63.73	64.43	65.67	65.45	71.72	77.81	78.95
Mesh	#nodes	8484	8484	8484	8484	8484	8484	8484	8677	8677	8677	8677	8677	8677	8677
	#elements	38150	38150	38150	38150	38150	38150	38150	38831	38831	38831	38831	38831	38831	38831
Solver	#iterations	173	214	197	304	296	258	346	304	247	149	253	192	308	227
	Time [sec]	161.85	186.82	174.27	234.21	228.12	208.55	256.39	234.87	270.21	197.91	494.97	180.03	250.31	263.34

Table B.1 (continued): Complete Listing of the Results for the Gap-Connected Stroma Cell Model

Conductivity [S/m]	σ_{medium}	0.5							0.5						
	$\sigma_{cytoplasm}$	0.05							0.05						
	$\sigma_{membrane}$	1.0e-7							1.0e-7						
	σ_{gap}	1.0e-7	1.0e-6	1.0e-5	1.0e-4	1.0e-3	1.0e-2	5.0e-2	1.0e-7	1.0e-6	1.0e-5	1.0e-4	1.0e-3	1.0e-2	5.0e-2
Geometry [μm]	$t_{membrane}$	0.02							0.03						
	r_{gap}	0.5							0.5						
TMP1 [μV]	ϕ_{inside}	292.46	304.31	307.84	296.24	260.54	210.57	205.93	302.23	287.52	318.32	330.73	266.01	209.54	205.14
	ϕ_{inside}	73.14	75.89	77.65	85.30	138.27	187.08	195.71	71.32	68.33	75.55	87.22	122.31	181.08	193.90
	TMP	219.32	228.42	230.19	210.94	122.27	23.49	10.22	230.91	219.18	242.77	243.51	143.70	28.46	11.24
TMP2 [μV]	ϕ_{inside}	400.00	400.00	400.00	400.00	400.00	400.00	400.00	400.00	400.00	400.00	400.00	400.00	400.00	400.00
	ϕ_{inside}	310.27	320.33	323.91	319.72	320.68	308.83	306.75	313.75	300.65	326.90	344.23	312.81	294.30	293.58
	TMP	89.73	79.67	76.09	80.28	79.32	91.17	93.25	86.25	99.35	73.10	55.77	87.19	105.70	106.42
TMP3 [μV]	ϕ_{inside}	400.00	400.00	400.00	400.00	400.00	400.00	400.00	400.00	400.00	400.00	400.00	400.00	400.00	400.00
	ϕ_{inside}	309.53	319.68	323.30	319.06	319.99	307.99	305.89	313.27	300.10	326.52	343.93	312.29	293.64	292.90
	TMP	90.47	80.32	76.70	80.94	80.01	92.01	94.11	86.73	99.90	73.48	56.07	87.71	106.36	107.10
TMP4 [μV]	ϕ_{inside}	0.00	0.00	0.00	0.00	0.00	0.00	0.00	0.00	0.00	0.00	0.00	0.00	0.00	0.00
	ϕ_{inside}	60.81	63.03	63.88	64.80	78.37	89.98	95.24	62.70	60.03	65.97	71.68	77.22	98.01	106.25
	TMP	60.81	63.03	63.88	64.80	78.37	89.98	95.24	62.70	60.03	65.97	71.68	77.22	98.01	106.25
TMP5 [μV]	ϕ_{inside}	0.00	0.00	0.00	0.00	0.00	0.00	0.00	0.00	0.00	0.00	0.00	0.00	0.00	0.00
	ϕ_{inside}	61.30	63.54	64.40	65.32	79.05	90.81	96.12	63.04	60.35	66.33	72.07	77.67	98.63	106.92
	TMP	61.30	63.54	64.40	65.32	79.05	90.81	96.12	63.04	60.35	66.33	72.07	77.67	98.63	106.92
ϕ1 [μV]	ϕ1	309.16	319.36	322.99	318.73	319.67	307.60	305.48	313.04	299.82	326.33	343.79	312.05	293.33	292.58
ϕ2 [μV]	ϕ2	61.53	63.77	64.64	65.57	79.37	91.20	96.53	63.19	60.50	66.50	72.26	77.88	98.92	107.24
Mesh	#nodes	8677	8677	8677	8677	8677	8677	8677	8677	8677	8677	8677	8677	8677	8677
	#elements	38831	38831	38831	38831	38831	38831	38831	38831	38831	38831	38831	38831	38831	38831
Solver	#iterations	321	328	392	344	340	290	438	423	350	257	336	297	646	519
	Time [sec]	253.49	251.55	291.43	283.04	261.05	228.55	310.49	234.87	270.21	197.91	494.97	180.03	402.64	263.34

(please refer to Figure 4.25 for the corresponding location of each potential measurement)

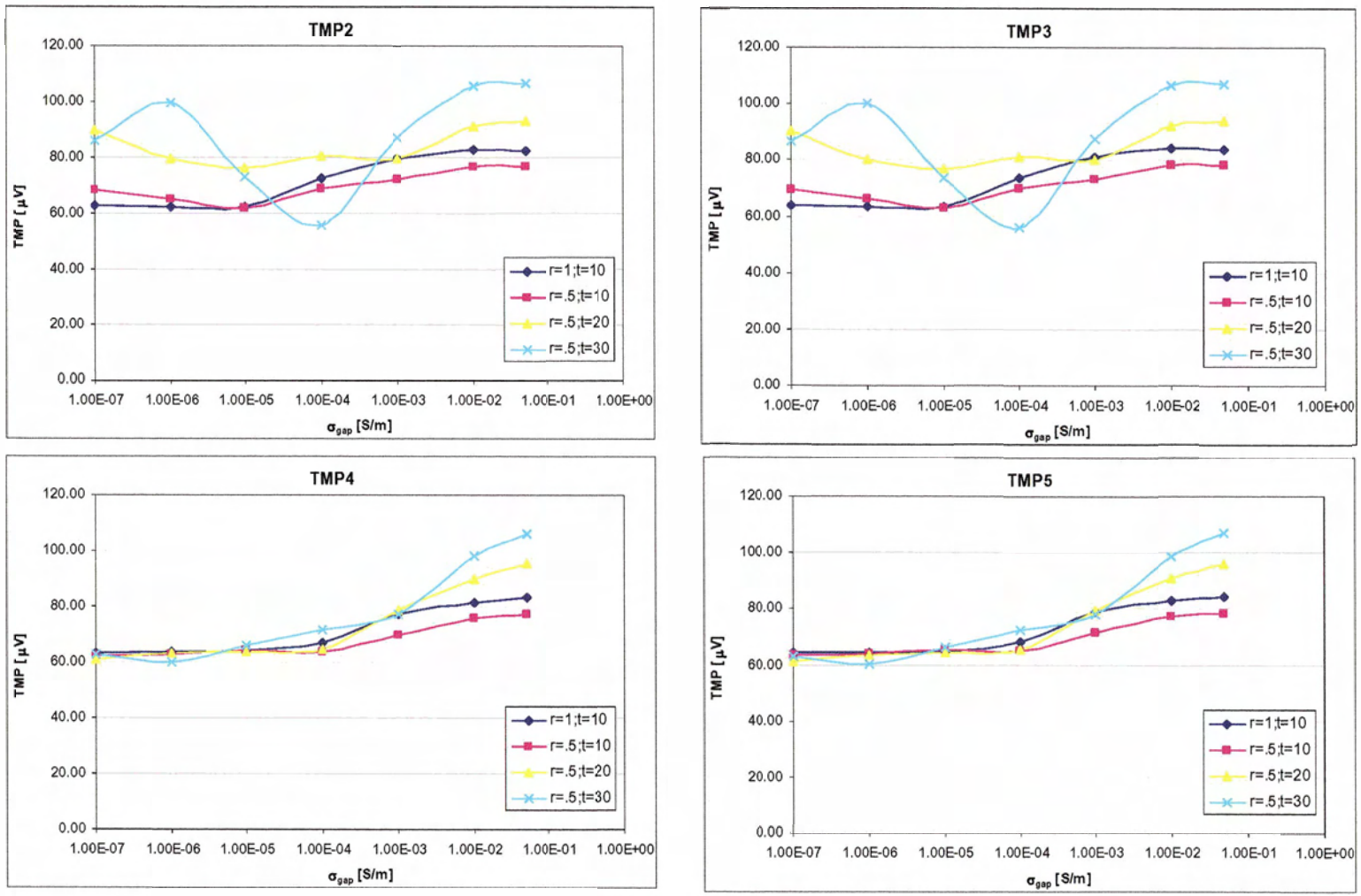

Figure B.1: Plots for TMP2, TMP3, TMP4 and TMP5 against σ_{gap}

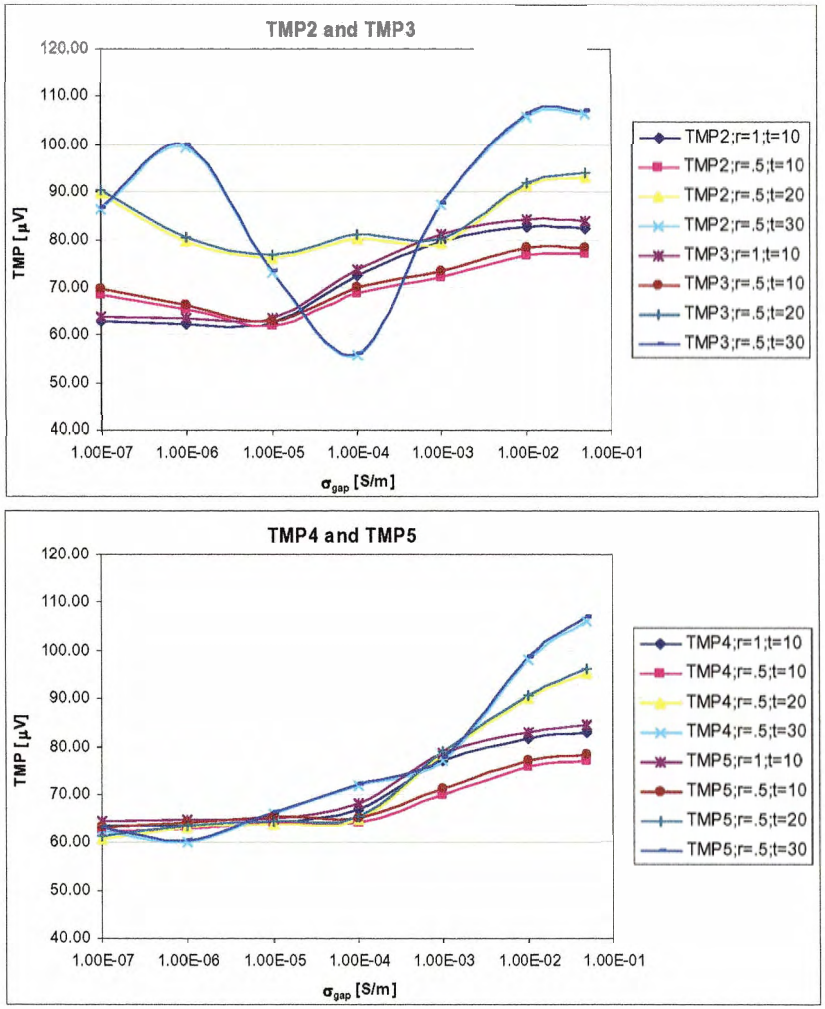

Figure B.2: Plots of (a) TMP2 and TMP3; (b) TMP4 and TMP5

TMP2 and TMP3 are both taken from the top plate while TMP4 and TMP5 are both from the bottom plate of the model. Although the values are fairly close, for all different trials TMP3 is slightly higher than TMP2; likewise, TMP5 is slighter greater than TMP4.

Referring to the stroma cell geometry, the cross-sections of the stroma cell parallel to the *xy*-plane are ellipses instead of circles. TMP2 and TMP4 are taken at the boundaries of the major axis, while TMP3 and TMP5 are taken at that of the minor axis.

This observation of larger TMP values, i.e., more rapid potential changes, with smaller stroma radii in the cross-section is consistent with the behavior observed with potential change along the *z*-axis as illustrated in Figure 4.28.

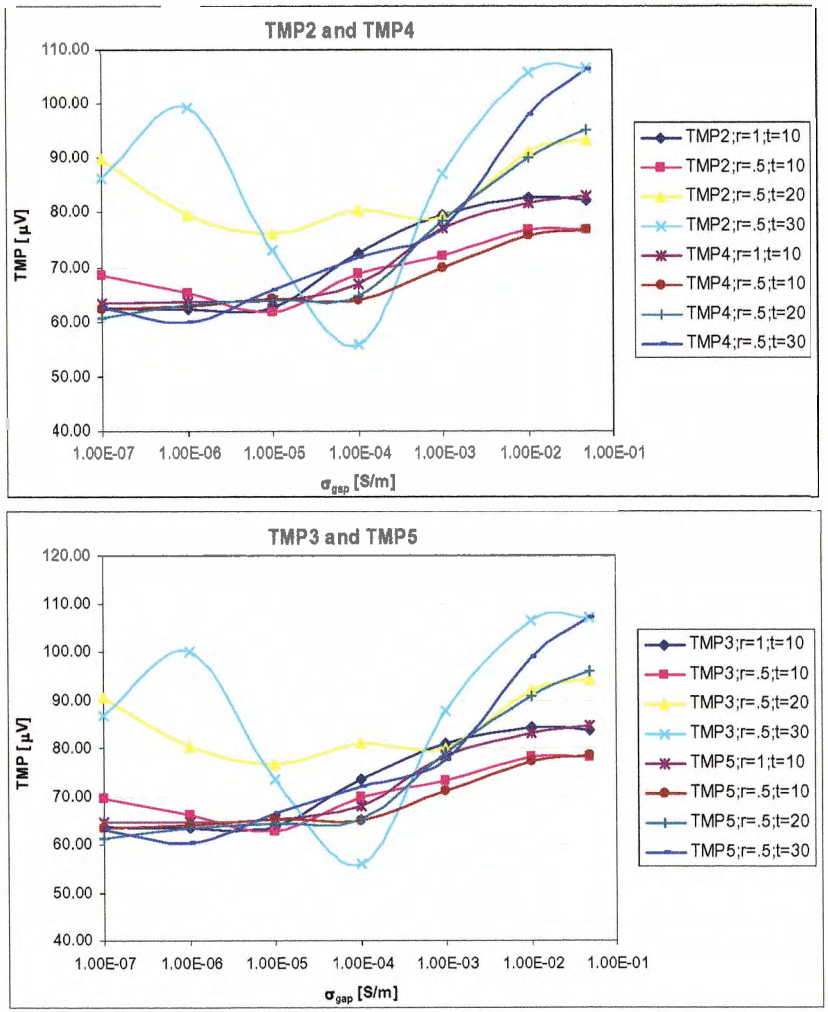

Figure B.3: Plots of (a) TMP2 and TMP4; (b) TMP3 and TMP5

The two partial cells in the model are identical; therefore, the entire model is symmetric across the *xy*-plane. However, instead of having comparable values, TMP2 and TMP4 do not show as good an agreement as TMP2 to TMP3, neither do TMP3 and TMP5.

Although both the top and bottom plates are assigned Dirichlet boundary conditions, the top plate is given a constant potential when the bottom plate is regarded as ground plate. As listed in Table 3.1, they are considered different boundary conditions probably with different implementation in FEMLAB, which may explain why one is more sensitive to increase in the membrane thickness.

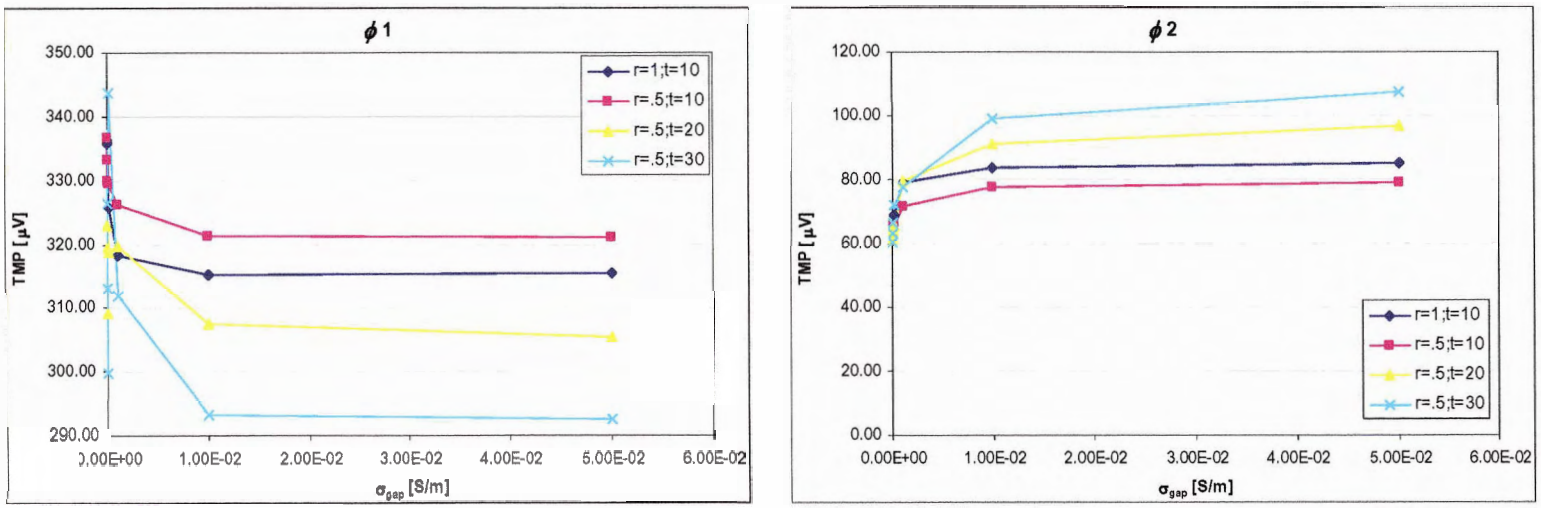

Figure B.4: Plots of $\phi 1$ and $\phi 2$

$\phi 1$ and $\phi 2$ are the electric potential taken at the top and bottom corner of the entire domain along the central axis of the stroma arms. Due to the insulating cell membrane separating the interior of the stroma cell from the outside medium, $\phi 1$ at the top plate should be smaller than the applied potential of 400 μV at the top plate *outside* of the cell; while $\phi 2$ would inevitably have slightly higher potential than the 0 μV outside the cell on the bottom plate. The sum of $\phi 1$ and $\phi 2$ is roughly 400 μV, therefore as σ_{gap} increases, $\phi 1$ decreases but $\phi 2$ increases.